Magnetic order at coherent oxide interfaces

Dissertation

zur Erlangung des

Doktorgrades der Naturwissenschaften (Dr. rer. nat.)

der Naturwissenschaftlichen Fakultät II

der Martin-Luther-Universität Halle-Wittenberg

vorgelegt

von **Herrn Sujit Das**

geb.am 09.01.1988 in Gangarampur, West Bengal, India

Gutachter

1. Prof. Dr. Kathrin Dörr
2. Dr. Karl-Michael Schindler
3. Prof. Dr. Vasily Moshnyaga
verteidigt am: 19.12.2016
Halle (Saale)

Dedicated to

my parents and late grandmother

Contents

List of Figures

List of Tables

List of Abbreviations

TMO   Transition metal oxide

PLD   Pulse Laser Deposition

RHEED   Reflection high-energy electron diffraction

XRD   X-ray diffraction

STEM   Scanning transmission electron microscopy

HAADF   High-angle annular dark-field

SL   Superlattice

BL   Bilayer

SQUID   Superconducting quantum interfering device

FC   Field cooled

u.c.   Unit cell

STO $SrTiO_3$

LAO $LaAlO_3$

PMN-PT $0.72PbMg_{1/3}Nb_{2/3}O_3$-$0.28PbTiO_3$

LAMO $La_{0.7}A_{0.3}MnO_3$ (A=Ca, Sr)

LSMO $La_{0.7}Sr_{0.3}MnO_3$

LCMO $La_{0.7}Ca_{0.3}MnO_3$

SRO $SrRuO_3$

XAS   X-ray absorption spectroscopy

XMCD   X-ray magnetic circular dichroism

Chapter 1

Introduction

Transition metal oxides (TMO) are well known for their complex magnetic and electrical properties. Interfaces between perovskite oxides have garnered enormous interest in the last decade by featuring several novel aspects such as interfacial coupling, different magnetic order and so on. One of the most notable properties is to support a conducting electron gas at the interface between two insulators $LaAlO_3$ and $SrTiO_3$ [1, 2]. Also it is reported that at low temperatures the $LaAlO_3/SrTiO_3$ interface showed superconducting behavior [3, 4]. The interfaces composed of two non-magnetic layers (e.g., interface between antiferromagnet $LaCrO_3$ and $LaFeO_3$, between antiferromagnet $LaMnO_3$ and paramagnet $LaNiO_3$) on the (111) perovskite substrate show a ferromagnetic behavior [5, 6]. Microscopic origin of these phenomena are dependent on the modification of the interfaces, so called reconstruction of the interfaces of these materials such as lattice reconstruction, electronic reconstruction, orbital reconstruction, complex interplay among charge, and spin associated with the d electrons of these materials [1, 7]. Perovskite manganites and their heterostructures are well studied and their behavior can be tuned by varying the composition, temperature, pressure and strain [8, 9, 10]. Magnetic interfaces, provide an excellent illustration of the richness of the interfacial phenomena which is highly relevant for technological applications such as magnetic field sensors and memories or read heads [11, 12]. Several studies have focused on the microscopic coupling mechanism at the interfaces in order to tune them more favorably for industrial applications. The interfacial exchange coupling between layers governs the overall properties of the heterostructure. For instance, ferromagnetic/antiferromagnetic alignments of magnetic moments are usually attributed to superexchange interactions across the interface [13].

The objective of this thesis is to study and explain the magnetic order at the interfaces in coherent magnetic perovskite oxide heterostructures like manganites with $SrRuO_3$ and $SrTiO_3$. The structure of the interface and the epitaxial strain are identified as the fundamental tools for controlled manipulation of the physical properties of these heterostructures. A brief overview on the materials which are used for the preparation of the heterostructures is presented in **chapter** 2. The structural aspects and magnetic properties of doped rare earth manganites ($La_{1-x}A_xMnO_3$; A=Sr, Ca), $SrRuO_3$ and $SrTiO_3$ are

discussed. Recent studies and advancements on thin films of these manganites, $SrRuO_3$ and $SrTiO_3$ and their heterostructures are also highlighted.

Experimental techniques and tools used to characterize the films are summarized in **chapter** 3. The growth technique, various methods for structural studies like reflection high energy electron diffraction, X-ray diffraction, atomic force microscopy, transmission electron microscopy are described in this context. Furthermore, techniques used for the magnetic investigation of thin films and reversible strain dependent magnetic characterization are described in this chapter.

Chapter 4 reports the investigation of the magnetic order of $La_{0.7}Sr_{0.3}MnO_3$(LSMO)/ $SrRuO_3$(SRO) coherent superlattices (SLs). The discussion involves fabrication of the LSMO/SRO SLs on (001)- oriented $SrTiO_3$ (STO) and piezoelectric $0.72PbMg_{1/3}Nb_{2/3}O_3$-$0.28PbTiO_3$ (PMN-PT) substrates. The coherent growth and the interface roughness of the SLs are investigated by structural analysis of the SLs. The reversible substrate strain has notable effects on the interfacial magnetic coupling at the LSMO/SRO interfaces as well as the overall magnetization of the SLs.

The magnetic order and the interfacial magnetic coupling at the interfaces in $La_{0.7}Ca_{0.3}$ MnO_3 (LCMO)/ $SrRuO_3$ (SRO) SLs under different elastic strain are discussed in **chapter** 5. In order to obtain different elastic strain, the SLs are synthesized on (001)-oriented $LaAlO_3$ (LAO), STO and PMN-PT substrates. The strain value and the interfacial roughness of the SLs are determined through structural characterization. The existence of an enhanced interfacial magnetic coupling and magnetization is observed under compressive strain. The former can be attributed to the phenomenon of exchange bias at the interface.

In **chapter** 6, a model interface between two ferromagnetic perovskite oxides $La_{0.7}Sr_{0.3}$ MnO_3 and $SrRuO_3$- is examined, in which, a desirable control of interface termination is facilitated on an atomic scale. For this, two different interfaces for SRO/LSMO and LSMO/SRO bilayers (BLs) are fabricated on TiO_2 terminated STO substrate. The scanning transmission electron microscopy (STEM) analysis reveals atomically sharp MnO_2-SrO termination at the interface of SRO/LSMO BL in which LSMO and, subsequently SRO are grown on the STO substrate. The reversed layer sequence (LSMO/SRO/STO(001)) in the BL nominally leads to the RuO_2-(La,Sr)O termination at the interface. Depending on the microscopic details, these different terminations have strong impact on the resulting magnetic properties of the BLs. The interfacial antiferromagnetic coupling, lattice symmetry of SRO and the switching behavior of Mn and Ru are quite different in these two cases

Chapter 7 deals with fabrication, structural and magnetic studies of $La_{0.7}Ca_{0.3}MnO_3$ / $SrTiO_3$ SLs on LAO, STO and PMN-PT substrates. The substrate strain has strong impact on the magnetization and transition temperature for the SLs, which equally applies to the case of reversible strain induced by the external electric field. It is especially noted that such epitaxial strain from the substrates plays a vital role in manipulating the orbital occupancy.

Finally in **chapter** 8, all the results are summarized with possible outlooks of magnetic heterostructures.

Bibliography

[1] M. Salluzzo , S. Gariglio , X. Torrelles , Z. Ristic , R. Di Capua , J. Drnec , M. Moretti Sala , G. Ghiringhelli , R. Felici , and N. B. Brookes, " Structural and Electronic Reconstructions at the LaAlO$_3$ /SrTiO$_3$ Interface,'' Adv. Mater. **25**, 2333 (2013).

[2] A. Ohtomo and H. Y. Hwang, "A high-mobility electron gas at the LaAlO$_3$/SrTiO$_3$ heterointerface," Nature **427**, 423 (2004).

[3] S Gariglio, N Reyren, A D Caviglia and J-M Triscone, Superconductivity at the LaAlO$_3$ /SrTiO$_3$ interface, J. Phys.: Condens. Matter **21**, 164213 (2009).

[4] Richter, H. Boschker, W. Dietsche, E. Fillis-Tsirakis, R. Jany, F. Loder, L. F. Kourk-outis, D. A. Muller, J. R. Kirtley, C. W. Schneider and J. Mannhart, Interface superconductor with gap behaviour like a high-temperature superconductor, Nature **502**, 508 (2013).

[5] K. Ueda, H. Tabata, and T. Kawai, Ferromagnetism in LaFeO$_3$-LaCrO$_3$ superlattices, Science **280**, 1064 (1998).

[6] Marta Gibert, Pavlo Zubko, Raoul Scherwitzl, Jorge *Íñ*iguez & Jean-Marc Triscone, "Exchange bias in LaNiO$_3$–LaMnO$_3$ superlattices," Nature Materials **11**, 195 (2012).

[7] J. Mannhart and D.G. Schlom, "Oxide Interfaces—An Opportunity for Electronics,'' Science **327**, 1607 (2010).

[8] J. H. Song, T. Susaki, and H. Y. Hwang, "Enhanced Thermodynamic Stability of Epitaxial Oxide Thin Films,'' Adv. Mater. **20**, 2528 (2008).

[9] Y. Tokura, "Colossal Magnetoresistive Oxides Advances in Condensed Matter Science'' Gordon and Breach Science Publishers, Amsterdam, Vol. 2 (2000).

[10] C. Thiele, K. Dörr, O.Bilani, J.Rödel, and L. Schultz, "Influence of strain on the magnetization and magnetoelectric effect in La$_{0.7}$A$_{0.3}$MnO$_3$ /PMN-PT (001) (A=Sr,Ca),'' Phys. Rev. B **75**, 054408 (2007).

[11] M. Bibes, J.E. Villegas and A. Barthelemy, ''Ultrathin oxide films and interfaces for electronics and spintronics,'' Adv. Phys. **60**, 5 (2011).

[12] B. Dieny, V. S. Speriosu, S. S. P. Parkin, B. A. Gurney, D. R. Wilhoit, and D. Mauri, "Giant magnetoresistive in soft ferromagnetic multilayers,'' Phys. Rev. B **43**, 1297 (1991).

[13] J. Nogués, D. Lederman, T. J. Moran, and I. K. Schuller, "Positive Exchange Bias in FeF_2-Fe Bilayers'' Phys. Rev. Lett.**76**, 4624 (1996).

Chapter 2

Materials and their heterostructures

A brief description of various fundamental bulk properties of doped manganite $La_{0.7}A_{0.3}$ MnO_3 ($A=Sr$, Ca), $SrRuO_3$ and $SrTiO_3$ is presented in this chapter. The pre-existing studies which reveal some of the important aspects of magnetic behaviors and other physical properties of thin films of these materials and their heterostructures are also highlighted.

2.1 $\mathbf{La_{0.7}A_{0.3}MnO_3}$ ($A=Sr$, Ca)

Doped perovskite manganites exhibit a variety of unique magnetic, electronic and transport behaviors such as colossal magnetoresistance (CMR), spin/charge/orbital ordering, high degree of spin polarization etc [1, 2, 3]. The phenomena such as giant magnetoresistance (GMR), colossal magnetoresistance (CMR), spin-tunneling in junctions (STJ) have attracted significant attention in perovskite mixed valence manganites $La_{1-x}A_x$ MnO_3 ($A=$ Sr, Ca). They are considered a model system for the study of interplay of spin/charge/orbital degree of freedoms in correlated oxide systems [1, 2, 4, 5]. The different electronic correlations emerge in the system as a function of x that give rise to a rich and interesting phase diagram of the doped manganite ($La_{1-x}Sr_xMnO_3$ and $La_{1-x}Ca_xMnO_3$) [Fig.2.1 (a) and (b)]. The notable features include the existence of an antiferromagnetic insulator at certain high and low doping concentrations (x) and a ferromagnetic metal with high Curie temperature ($T_C = 370K$ for $La_{1-x}Sr_xMnO_3$, T_C=260K for $La_{1-x}Ca_xMnO_3$) that peaks around $x \approx 0.33$ [1, 3]. Since the density of states at the Fermi level (E_F) are occupied mostly by the majority-spin electrons [6, 7] in some manganites like $La_{0.7}Sr_{0.3}MnO_3$ (LSMO) may have applicability in the device physics [8, 3].

The physics of the ferromagnetism in the metallic state of these compounds is explained by double exchange (DE) mechanism proposed by Zener [9]. The DE process involves two simultaneous motions of electrons - hopping from Mn^{3+} ion to the oxygen and oxygen to the Mn^{4+} ion as shown by arrows in Fig.2.2. For illustration, let us consider the following orbital picture in $La_{0.7}A_{0.3}MnO_3$. Because of the 180 degree orientation of the Mn^{3+} - O -
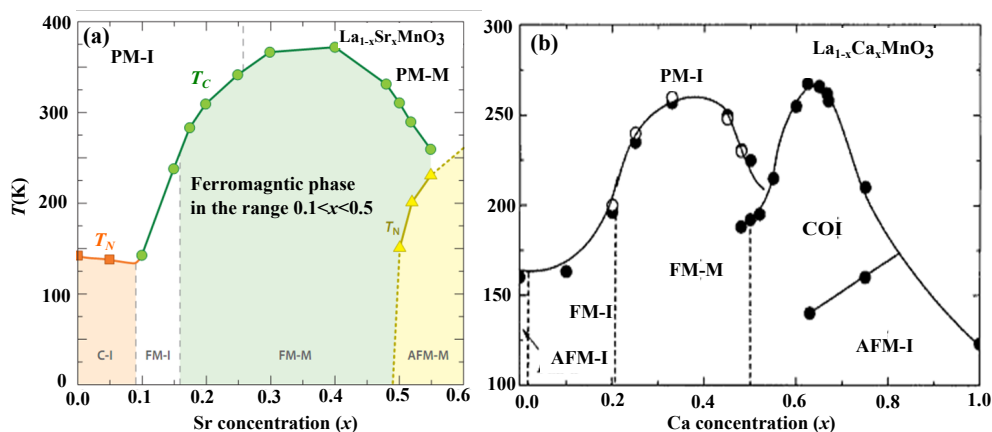
Figure 2.1:   Magnetic and electronic phase diagrams of (a) $La_{1-x}Sr_xMnO_3$ and (b) $La_{1-x}Ca_xMnO_3$. The ingredients include a paramagnetic insulator (PM-I), paramagnetic metal (PM-M), canted insulator (CI), ferromagnetic insulator (FM-I), ferromagnetic metal (FM-M), antiferromagnetic insulator (AFM-I), and charge-ordered insulator (COI). T_C and T_N, are Curie and Néel temperatures, respectively (taken from [3] and [1]).
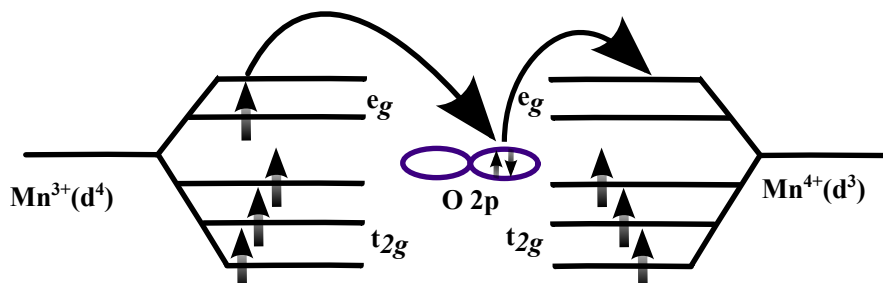
Figure 2.2:   Sketch of the double exchange mechanism which involves two Mn ions and one O ion. The mobility of e_g electrons improves if the localized spins are parallel.

Mn^{4+} bond, the e_g orbitals in Mn^{3+} are directly interacting with the O 2p orbitals. As a result of strong on-site Hund's coupling, the itinerant e_g electron in Mn^{3+} is aligned with the local core spins ($S{=}3/2$, t^3_{2g}) ferromagnetically. Consequently, this electron can hop from Mn^{3+} to Mn^{4+} to minimize its kinetic energy enforcing all spins to be aligned giving rise to ferromagnetism and metallicity in the material [2].

The physical properties of the perovskite lattice ABO_3 strongly depends on doping elements and their doping level (x). The traditional way to characterize the perovskite crystal structure is to look at the tolerance factor t which is a measure of the difference in ionic radii of various crystal compounds [10]. It quantifies the lattice matching between the AO and BO_2 planes: $t = (r_A{+}r_O)/\sqrt{2}(r_B{+}r_O)$, where $r_{A,B,O}$ is the mean ionic radius of the respective elements. For the cubic structure $t{=}1$. For $0.96{<}t{<}1$, the lattice structure is rhombohedral while orthorhombic for $t{<}0.96$. In common manganites, the tolerance factor t varies from 0.94 to 1 . The reduction of ionic size of A ions from this optimum value leads to an increase in rotation of MnO_6 octahedra which weakens the double exchange [11].

The magnetic properties of manganite thin films are very sensitive to the lattice strain induced by lattice mismatch between the film and the underlying substrate. When man-
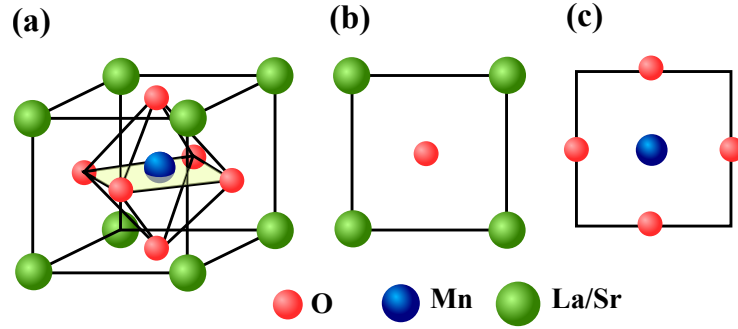
Figure 2.3: (c) Schematic diagram of unit cell of LSMO with the two possible termination layers shown in (b) La(Sr)O and (c) MnO_2.

ganite films are grown on different substrates like LAO, STO and PMN-PT, the induced epitaxial strain between the films and substrates can change the magnetic anisotropy [12, 13, 14, 15], thus, having drastic effects on the magnetic properties of the films. However, the thin films are grown epitaxially with (001) orientation on (001) oriented substrates because of the cubic symmetry of the substrates [16] which induces a pseudocubic unit cell of $La_{0.7}A_{0.3}MnO_3$ [see Fig.2.3 (a)]. The unit cell angle α and the lattice parameter of $La_{0.7}Sr_{0.3}MnO_3$ ($La_{0.7}Ca_{0.3}MnO_3$) are 90.26^o (90.26^o) and $3.87Å$ ($3.84Å$) respectively. When $La_{0.7}A_{0.3}MnO_3$ is grown "cube on cube" on a (001)-oriented substrate, there can be two atomic terminations either La(A)O plane or MnO_2 plane as shown in Fig.2.3 (b) and (c), respectively [17].

$La_{0.7}Sr_{0.3}MnO_3$(LSMO) films on various substrates, such as LAO(001), STO(001) and PMN-PT (001) are highly strained [12, 18]. The films grow in a layer-by-layer mode (Frank-Van der Merwe), viz., atoms attach preferentially to the surface sites resulting in atomically smooth layers. The process of a single layer formation starts with 2D islands which complete that layer first prior to growth of subsequent layers [Fig.2.4 (a)] [19]. The in-plane pseodocubic lattice parameters of LSMO, LAO, STO, and PMN-PT are $3.87Å$, $3.79Å$, $3.905Å$ and $4.02Å$, respectively. The LSMO lattice experiences a large biaxial tensile strain because of $+3.7\%$ lattice mismatch on PMN-PT [lattice mismatch, $\delta = (a_{substrate} - a_{LSMO})/a_{substrate}$], $+0.89\%$ on STO and biaxial compressive strain on LAO due to -2.1% lattice mismatch [12, 18].

The easy axis of magnetization depends on the substrate strain. For tensile films deposited on the STO substrate, the unit cell is elongated along the film's plane ($a_{in-plane}=$ $3.905Å$) with a reduced out-of-plane parameter ($c_{out-of-plane}=3.85Å$) and an easy axis of magnetization M in the film plane is observed. For compressive strained films deposited on LAO substrate, the situation is reversed with a unit cell elongated along the growth direction ($c_{out-of-plane}=4.00Å$ and $a_{in-plane}=3.79Å$) and an easy direction for magnetization M along this out-of-plane direction [20].
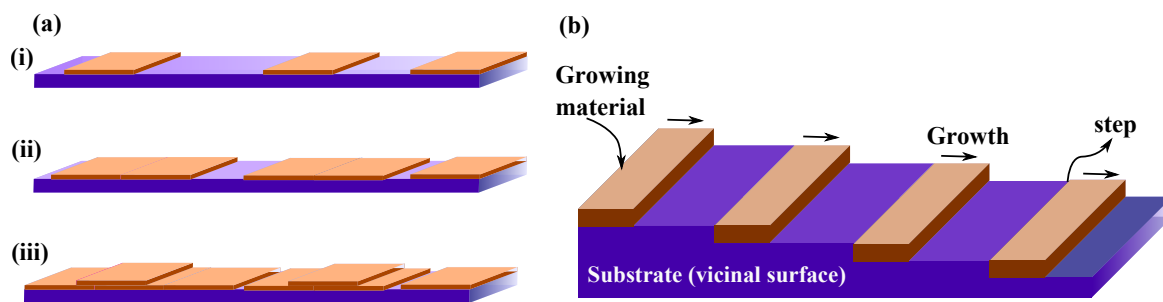
Figure 2.4: (a) Different stages of layer-by-layer growth by nucleation of 2D islands. (b) Film nucleation on the substrate in the case of step flow.

2.2 SrRuO$_3$

SrRuO$_3$ (SRO) is the interesting and infinite-layer (n=∞) material in the ruthenates Sr$_{n+1}$Ru$_n$O$_{3n+1}$. At room temperature it exhibits orthorhombic symmetry with lattice parameters a=5.567Å, b=5.5304Å, and c=7.8446Å (space group *Pbmn*) [Fig.2.5 (a)] [21]. The structure of SRO changes to higher symmetry perovskite structures with temperature. Around 550°C, the orthorhombic structure transforms into a tetragonal one with space group *I4/mcm* [22] and around 680 °C, this tetragonal SRO further transforms into a cubic structure with the standard perovskite space group *Pm3m* [22]. SRO is known to be a unique among the $4d$ transition metal oxides, showing an itinerant ferromagnet. The Curie temperature (T_C) is of ~160K in single crystal form [23], and is reduced typically to ~150K [24] by strain in thin films. The electronic configuration of Ru atoms in SRO being Ru$^{4+}t_{2g}$ ($4d^4$), the conduction electrons are free to move within the material. The ferromagnetism which arises from the parallel alignment of magnetic moments of Ru$^{4+}t_{2g}$ electrons is, thus, called "itinerant". The moment of SRO is expected to be $2\mu_B$ due to low-spin state of the four ruthenium electrons. But the measured magnetic moment in bulk (film) is 1.6 μ_B (1.4 μ_B) which is consistent with recent band calculations that indicate a strong Ru t_{2g}-O $2p$ hybridization [25, 26].

SRO is usually grown on vicinal substrates in a step flow growth mode. There can be two terminations either SrO termination or RuO$_2$ termination [21]. In the step flow mode, steps of the substrate are usually of monolayer height. During the growth on the terrace (vicinal) surface of the substrate, the attachment of the freshly deposited atoms (adatoms) takes place on the pre-existing steps of the terraces. The surface, thus, maintains its vicinal (terrace) shape as the growth occurs through step propagation [Fig.2.4 (b)].

In SRO thin film the RuO$_6$ octahedra rotation produces a distorted, pseudocubic perovskite structure [the inner cube in Fig.2.5 (a)] with lattice constant a= 3.93 Å. When SRO grows coherently on a single crystal substrate, lattice mismatch between them introduces strain that can affect the structural, magnetic and transport properties of the SRO layer. A schematic depiction of heteroepitaxial growth of orthorhombic SRO layer on STO (001) substrate is demonstrated in Fig.2.5 (b). As can be seen from the figure the orientation is: $<110>_L||<001>_S$, $<-110>_L||<100>_S$ and $<001>_L||<010>_S$ (The subscript
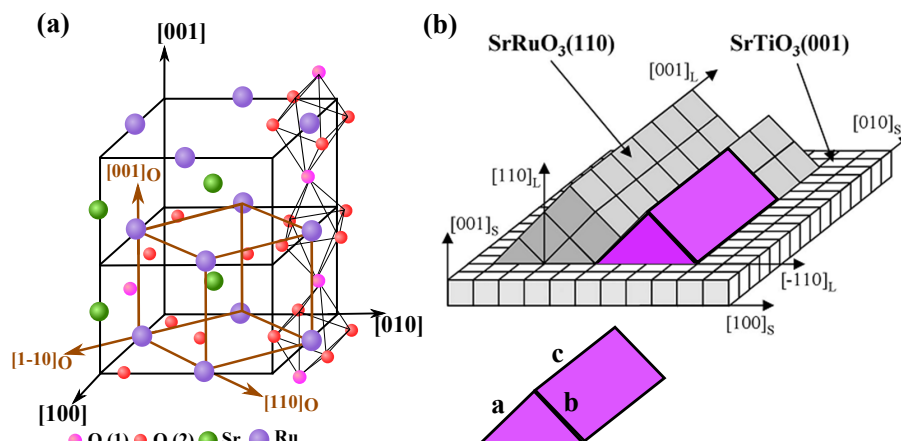
Figure 2.5: (a) Schematic view of the orthorhombic unit cell of SRO (taken from [21]) (b) Schematic representation of the heteroepitaxial growth of SRO (110) thin film on cubic (001)-STO substrate (taken from [24]).

'L' denotes the SRO layer and 'S' denotes the substrate) [27]. SRO thin films are usually grown coherently on STO, $DyScO_3$, $GdScO_3$, and $NdGaO_3$ because of close match in the lattice parameters and serve as a technologically important bottom layer with atomically smooth surfaces and interfaces [28]. The symmetry of SRO is highly affected by lattice strain, e.g., the orthorhombic symmetry of SRO (under compressive strain) changes to tetragonal symmetry under tensile strain [29]. The easy axis rotates from tilted out-of-plane orientation in case of compressive strain to in-plane orientation for tensile strain and stays along the pseudocubic $<100>_L$ and $<010>_L$ directions [30].

2.3 SrTiO$_3$

$SrTiO_3$ (STO) is a nonmagnetic wide-bandgap insulator and considered among today's most important oxide materials for substrates. At room temperature, both the bulk and thin film of STO crystallize in cubic perovskite structure (space group $Pm3m$) with a lattice parameter of 3.905Å. However, the lattice symmetries change with temperature. Below 105K it has tetragonal phase (space group $I4/mcm$) while orthorhombic below 55K [31]. This transition can be described in terms of TiO_6 octahedra tilts. In the cubic phase, STO has no tilting of the oxygen octahedra. The transformation into the tetragonal crystal structure is due to a coupled tilting of the oxygen octahedra along the c axis while that in the orthorhombic phase owes to opposite rotation of neighbouring oxygen octahedra.

STO is an excellent substrate for epitaxial growth of high-temperature superconductors and many oxide-based thin films. It is particularly well known as a substrate for the growth of $LaAlO_3$-$SrTiO_3$ interfaces [32]. Its bulk lattice parameter of 3.905Å makes it suitable as the substrate for the growth of many other oxides, including the rare-earth manganites, titanates, lanthanum aluminate ($LaAlO_3$), strontium ruthenate ($SrRuO_3$) and their heterostructures. The (100) STO surface exhibits two different types of atomic

alternating termination. One is formed by a TiO_2 termination and the other by an SrO termination [33, 34]. STO has also been known to exhibit quantum paraelectric behavior and a large field-induced piezoelectric effect at low temperatures [35, 36]. Oxygen vacancies are fairly common in STO crystals and thin films. These defects make the material more conducting and simultaneously opaque by introducing additional free electrons to the conduction band. The vacancies are primarily caused by exposure to reducing conditions, such as high vacuum at elevated temperatures.

2.4 Heterostructures of $La_{0.7}A_{0.3}MnO_3$ (A = Sr, Ca), $SrRuO_3$, and $SrTiO_3$

The oxide heterostructures exhibit plenty of exotic phenomena like interfacial conduction between two insulator oxides, magnetism, superconductivity and many others. The most exciting and prominent example is the conducting nature of the interface between the insulators $LaAlO_3$ and $SrTiO_3$. In the same avenue, heterostructures with manganites also have exotic properties and novel functionalities which are quite different from those of the respective bulk materials. The reason for this is the vastly unexplored electronic and lattice structures of the interfaces and the elastic strain that is induced by lattice mismatch between the heterostructure components and the substrate. They influence the structural, magnetic and electric transport properties of the overall compounds. For example, an exchange bias effect (shift of the magnetic hysteresis loop from centre) is often observed at the interfaces between ferromagnetic and antiferromagnetic films [37], conducting as well as superconducting interface between two insulator $LaAlO_3$ and $SrTiO_3$ [32, 38], magnetism between two non-magnetic interface $LaCoO_3$ and $LaFeO_3$ [39] which are heavily depended on the interfacial electronic structure in particular spin, orbital reconstruction, roughness, etc.[37, 32, 38, 39]. Magnetic interfaces are widely studied for phenomena of magnetic interfacial coupling and spin-polarized electrical transport. The control over local magnetization of the films is important from the perspectives of technological application like magnetoresistive devices as well as fundamental physics [40, 41]. For example, electromechanical coupling via a piezoelectric material can be used to control the orientation and strength of the magnetization. In that case, by tuning the lattice parameters of the heterostructure through an applied electric field [42].

Some of the promising properties of manganites [$La_{0.7}Sr_{0.3}Mn\,O_3$(LSMO), $La_{0.7}Ca_{0.3}Mn\,O_3$ (LCMO)] include a nearly half-metallic and ferromagnetic behavior with an extremely high degree of spin polarization [43]. This is strongly suggestive for making magnetic tunnel junctions out of these materials. Magnetic tunnel junctions, consisting of two half-metallic ferromagnets (LSMO, LCMO) separated by an insulating thin layer $SrTiO_3$(STO) [LSMO/STO/LSMO] are extensively studied by many researchers in order to realize its applicability in preparing the magnetoresistive devices, such as magnetic sensors. Such a junction shows very large tunnel magnetoresistance (TMR) of 1800% at 4K in corre-

spondence to a tunnel spin polarization of 95% [6]. However, TMR is rapidly suppressed with increasing temperature and typically disappears at room temperature [43] which is attributed to the formation of nonconducting layer, so called the dead layers near the LSMO/STO interface. The dead layer provides disordered spins in the tunnel barrier which contribute to the spin depolarization, in which the ferromagnetism of LSMO is locally deteriorated [42, 44].

The magnetotransport properties of metallic ferromagnetic oxides such as $La_{0.7}A_{0.3}Mn$ O_3 (A=Sr, Ca) and $SrRuO_3$ have been the subject of a large-scale research effort [45, 46, 47]. In recent years, the transition metal oxide heterostructures (such as LSMO-SRO, LCMO-SRO) are also in the focus of interest, because interfaces of these oxide heterostructures show strong antiferromagnetic (AFM) coupling whereas the parent compounds are ferromagnetic [48, 49, 50]. The antiferromagnetic exchange coupling at the interface leads to antiparallel orientation of the magnetizations between SRO and LSMO layers which can be sustained in a several tesla of magnetic field [48, 49, 50]. An exchange-bias phenomenon has been observed in such ferromagnetic oxide heterostructures [51] and the cooling history of the sample is shown to be very important to decide the magnetic order at low temperatures [52]. At low temperatures, the magnetic anisotropy of SRO is so large that full alignment of Ru spins is hard to achieve in applied magnetic fields of a few teslas. Hence, the arrangement of Ru spins during cooling is partially "frozen in". The frozen-in-structure of SRO at low temperatures and the in-plane Ru moments at the interface changes to out-of-plane deep inside the SRO layers in such heterostructures or superlattices as detected by combining polarized neutron reflectometry (PNR) and bulk magnetization measurements [53, 54]. The LSMO-SRO heterostructures have demonstrated many other novel physical properties induced by interface effects, such as the strong inverse magnetocaloric effect which might open an constructive approach for magnetic refrigeration applications [55, 56], 2D hole gas [57], and inverse photostrictive effect [58].

The symmetry of the layers may be different in the heterostructures. The structural change of SRO layers from orthorhombic to tetragonal has been shown in $[Pr_{0.7}Ca_{0.3}MnO_3$ (PCMO)/SRO]n/ STO (001) superlattices [61]. The single layer of LSMO structure on the STO (001) substrate is expected to be tetragonal with octrahedra rotation $a^0a^0a^0$ near the interface of the STO substrate, where single layer of SRO is expected to be orthorhombic (monoclinic distortion) structure with $a^-b^+c^-$ octrahedra rotation [59, 60].

Particular atomic arrangements at the interfaces (such as manganite-SRO heterostructure, manganite –STO heterostructure) are often endowed with intense coupling between the magnetic ions. Lattice strain is a vital parameter for manipulating the electronic states of complex oxide heterostructures. In this spirit, *in-situ* biaxial strain can provide a desired handle for the tunability of structural and magnetic coupling at the interfaces of the heterostructures. It has been shown to strongly affect and even reverse the sign of Mn-O-Ru interface coupling in ultrathin $SrRuO_3/AMnO_3/SrRuO_3$ (A=Ca or Pr) tri-

layers as observed by x-ray magnetic circular dichroism [62]. That experiment revealed the impact of strain on the magnetic coupling by comparing trilayers grown coherently on $SrTiO_3(001)$ and $LaAlO_3(001)$ substrates. Also different interface terminations are crucial which can dramatically alter the coupling between the layers and the physical properties of the heterostructures [32]. The interface between two (001)-oriented perovskites ABO_3 and $A'B'O_3$ can have two different interface terminations on an atomic scale (AO-BO_2-$A'O$-$B'O_2$ or BO_2 -AO-$B'O_2$-$A'O$). They could have significantly different nominal charge at the interfaces. A well known example is conducting behavior of the $LaAlO_3/SrTiO_3$ interface when the interface termination is LaO-TiO_2 and when the interface termination is AlO_2-SrO then it shows insulating behavior [32]. Also $BiFeO_3/La_{0.7}Sr_{0.3}MnO_3$ interface shows different ferroelectric polarization at the $La_{0.7}Sr_{0.3}O$-MnO_2-BiO-FeO_2 and MnO_2-$La_{0.7}Sr_{0.3}O$-FeO_2-BiO terminations, respectively [63]. Thus, epitaxial strain as well as different layer termination of the interface can offer additional ways to manipulate the interfacial magnetic state in the heterostructures. The focus of this thesis is to study these effects, more specifically, influence of *in-situ* biaxial strain and different layer termination of the interface on magnetic order and interfacial coupling strength in manganite/SRO and manganite/STO heterostructures.

Bibliography

[1] A. P. Ramirez, "Colossal magnetoresistance," Journal of Physics: Condensed Matter **9**, 8171 (1997).

[2] E. Dagotto, T. Hotta and A. Moreo, "Colossal magnetoresistance materials: the key role of phase separation," Physics Reports **344**, 1 (2001).

[3] Pavlo Zubko, Stefano Gariglio, Marc Gabay, Philippe Ghosez, and Jean-Marc Triscone, "Interface Physics in Complex Oxide Heterostructures," Annu. Rev. Condens. Matter Phys. **2**, 141 (2011).

[4] Y. Ishii, H. Yamada, H. Sato, H. Akoh, Y. Ogawa, M. Kawasaki and Y. Tokura, "Improved tunneling magnetoresistance in interface engineered $(La,Sr)MnO_3$ junctions", Appl. Phys. Lett., **89**, 042509 (2006).

[5] E. Gommert, H. Cerva, A. Rucki, R. v. Helmolt, J. Wecker, C. Kuhrt and K. Samwer, "Structure and magnetoresistive properties in La-manganite thin films," J. Appl. Phys. **81**, 5496 (1997).

[6] L. Samet, D. Imhoff, J.-L. Maurice, J.-P. Contour, A. Gloter, T. Manoubi, A. Fert and and C. Colliex, "EELS study of interfaces in magnetoresistive LSMO/STO/LSMO tunnel junctions," The Euro. Phys. J. B **34**, 179 (2003).

[7] H. Yamada, Y. Ogawa, Y. Ishii, H. Sato, M. Kawasaki, H. Akoh and and Y. Tokura, "Engineered Interface of Magnetic Oxides," Science **305**, 646 (2004).

[8] L. Balcells, E. Calvo and and J. Fontcuberta, "Room-temperature anisotropic magnetoresistive sensor based on manganese perovskite thick films", Journal of Magnetism and Magnetic Materials, **242**, 1166 (2002).

[9] C. Zener, "Interaction between the d-Shells in the Transition Metals. II. Ferromagnetic Compounds of Manganese with Perovskite Structure," Phys. Rev. **82**, 403 (1951).

[10] G.H. Jonker, J.H. Van Santen, "Ferromagnetic compounds of manganese with perovskite structure," Physica **16**, 337 (1950).

[11] H. Y. Hwang, S. W. Cheong, P. G. Radaelli, M. Marezio and B. Batlogg, "Lattice Effects on the Magnetoresistance in Doped LaMnO$_3$". Phys. Rev. Lett. **75**, 914 (1995).

[12] C. Thiele, K. Dörr, O.Bilani, J.Rödel, and L. Schultz, "Influence of strain on the magnetization and magnetoelectric effect in La$_{0.7}$A$_{0.3}$MnO$_3$ /PMN-PT (001) (A=Sr,Ca)," Phys. Rev. B **75**, 054408 (2007).

[13] C. Kwon, M.C. Robson, K.-C. Kim, J.Y. Gu, S.E. Lofland, S.M. Bhagat, Z. Trajanovic, M. Rajeswari, T. Venkatesan, A.R. Kratz, R.D. Gomez, and R. Ramesh, "Stress-induced effects in epitaxial La$_{0.7}$Sr$_{0.3}$MnO$_3$ films," J. Mag. and Mag. Mat. **172**, 229 (1997).

[14] R. Desfeux, S. Bailleul, A. Da Costa, W. Prellier and A. M. Haghiri-Gosnet, "Substrate effect on the magnetic microstructure of La$_{0.7}$Sr$_{0.3}$MnO$_3$ thin films studied by magnetic force microscopy," Appl. Phys. Lett. **78**, 3681 (2001).

[15] Y. Suzuki, H. Y. Hwang, S. W. Cheong and R. B. van Dover, "The role of strain in magnetic anisotropy of manganite thin films," Appl. Phys. Lett. **71**, 140 (1997).

[16] J.Z. Sun, D.W. Abraham, R.A. Rao and C.B. Eom, "Thickness-dependent magnetotransport in ultrathin manganite films," Appl. Phys. Lett. **74**, 3017 (1999).

[17] A-M Haghiri-Gosnet and J-P Renard, "CMR manganites: physics, thin films and devices," J. Phys. D: Appl. Phys. **36**, R127 (2003).

[18] D. Joonghoe, Y. N. Kim, Y. S. Hwang, J. C. Kim and N. H. Hur, "Strain-induced magnetic stripe domains in La$_{0.7}$Sr$_{0.3}$MnO$_3$ thin films," Appl. Phys. Lett. **82**,1434 (2003).

[19] Pimpinelli, Alberto; Jacques Villain (1998). Physics of Crystal Growth. Cambridge: Cambridge University Press. ISBN $0-521-55198-6$.

[20] A. M. Haghiri-Gosnet, J. Wolfman, B. Mercey, Ch. Simon, P. Lecoeur, M. Korzenski, M. Hervieu, R. Desfeux, and G. Baldinozzi, "Microstructure and magnetic properties of strained La $_{0.7}$Sr$_{0.3}$MnO$_3$ thin films", J. Appl. Phys. **88**, 4257 (2000).

[21] Gertjan Koster, Lior Klein, Wolter Siemons, Guus Rijnders, J. Steven Dodge, Chang-Beom Eom, Dave H. A. Blank, and Malcolm R. Beasley, "Structure, physical properties, and applications of SrRuO$_3$ thin films," Rev. Mod. Phys. **84**, 253 (2012).

[22] B.J Kennedy and B.A. Hunter, "High-temperature phases of SrRuO$_3$," Phys. Rev. B **58**, 653 (1998).

[23] J.M. Longo, P.M. Raccah, and J.B. Goodenough, "Magnetic properties of SrRuO$_3$ and CaRuO$_3$," J. Appl. Phys. **39**, 2963 (1968).

[24] Q. Gan, R.A. Rao, C.B. Eom, J.L. Garrett, and M. Lee, "Direct measurement of strain effects on magnetic and electrical properties of epitaxial $SrRuO_3$ thin films," Appl. Phys. Lett. **72**, 978 (1997).

[25] P. B. Allen, H. Berger, O. Chauvet, L. Forro, T. Jarlborg, A. Junod, B. Revaz, and G. Santi, "Transport properties, thermodynamic properties, and electronic structure of $SrRuO_3$" Phys. Rev. B **53**, 4393 (1996).

[26] D.J Singh "Electronic and magnetic properties of the 4d itinerant ferromagnet $SrRuO_3$," J. Appl. Phys. **79**, 4818 (1996).

[27] A. Vailionis, W. Siemons, and G, Koster, "Room temperature epitaxial stabilization of a tetragonal phase in $ARuO_3$ (A= Ca and Sr) thin films," Appl. Phys. Lett. **93**, 051909 (2008).

[28] N. Sai, A. M. Kolpak, and A. M. Rappe, "Ferroelectricity in ultrathin perovskite films," Phys. Rev. B **72**, 020101(R) (2005).

[29] A. Herklotz, M. Kataja, K. Nenkov, M. D. Biegalski, H.-M. Christen, C. Deneke, L. Schultz, and K. Dörr, "Magnetism of the tensile-strain-induced tetragonal state of $SrRuO_3$ films," Phys. Rev. B **88**, 144412 (2013).

[30] M. Ziese, I. Vrejoiu and D. Hesse, "Structural symmetry and magnetocrystalline anisotropy of $SrRuO_3$ films on $SrTiO_3$," Phys. Rev. B **81**, 184418 (2010).

[31] G. A. Samara, "The relaxational properties of compositionally disordered ABO_3 Perovskites," J. Phys.: Condens. Matter **15**, R367 (2003).

[32] A. Ohtomo and H. Y. Hwang, "A high-mobility electron gas at the $LaAlO_3/SrTiO_3$ heterointerface," Nature **427**, 423 (2004).

[33] F.M.F. De Groot, M. Grioni, J .C. Fuggle, J. Ghijsen, G.A. Sawatzky and H.Petersen, "Oxygen $1s$ x-ray-absorption edges of transition-metal oxides," Phys. Rev. B **40**, 5715 (1989).

[34] M Kawasaki, K Takahashi, T Maeda, R Tsuchiya, "Atomic control of the $SrTiO_3$ crystal surface," Science **266**, 1540 (1994).

[35] K. A. Müller and R. Burkard, "$SrTiO_3$- An intrinsic quantum paraelectric below 4 K," Phys Rev. B **19**, 3593 (1979).

[36] D. E. Grupp and A. M. Goldman, "Giant Piezoelectric Effect in Strontium Titanate at Cryogenic Temperatures," Science, **276**, 392 (1997).

[37] J. Nogués and I.K. Schuller, "Exchange bias," J.Magn. Magn. Mater. **192**, 203 (1999).

[38] S Gariglio, N Reyren, A D Caviglia and J-M Triscone, Superconductivity at the LaAlO$_3$ /SrTiO$_3$ interface, J. Phys.: Condens. Matter **21**, 164213 (2009).

[39] K. Ueda, H. Tabata, and T. Kawai, Ferromagnetism in LaFeO$_3$-LaCrO$_3$ superlattices, Science **280**, 1064 (1998).

[40] M. Bibes, J.E. Villegas and A. Barthelemy, ''Ultrathin oxide films and interfaces for electronics and spintronics,'' Adv. Phys. **60**, 5 (2011).

[41] B. Dieny, V. S. Speriosu, S. S. P. Parkin, B. A. Gurney, D. R. Wilhoit, and D. Mauri, "Giant magnetoresistive in soft ferromagnetic multilayers,'' Phys. Rev. B **43**, 1297 (1991).

[42] M.C. Dekker, A. Herklotz, L. Schultz, M. Reibold, K. Vogel, M.D. Biegalski, H.M. Christen, and K. Dörr, "Magnetoelastic response of La$_{0.7}$Sr$_{0.3}$MnO$_3$/SrTiO$_3$ super-lattices to reversible strain," Phys. Rev. B **84**, 054463 (2011).

[43] G. Banacha, R. Tyera, W.M. Temmerman, "Study of half-metallicity in LSMO," J.Magn. Magn. Mater. **272**, 1963 (2004).

[44] R. P. Borges, W. Guichard, J. G. Lunney, J. M. D. Coey, and F. Ott, "Magnetic and electric "dead" layers in (La$_{0.7}$Sr$_{0.3}$)MnO$_3$ thin films ," J. Appl. Phys. **89**, 3868 (2001).

[45] Y. Tokura and N. Nagaosa, "Orbital Physics in Transition-Metal Oxides," Science **288**, 462 (2000).

[46] J. S. Dodge, C. P. Weber, J. Corson, J. Orenstein, Z. Schlesinger, J. W. Reiner, and M. R. Beasley, Low-Frequency Crossover of the Fractional Power-Law Conductivity in SrRuO$_3$, Phys. Rev. Lett. **85**, 4932 (2000).

[47] Y. Kats, I. Genish, L. Klein, J.W. Reiner, and M. R. Beasley, Testing the Berry phase model for extraordinary Hall effect in SrRuO$_3$, Phys. Rev. B **70**, 180407(R) (2004).

[48] M. Ziese, I. Vrejoiu, E. Pippel, P. Esquinazi, D. Hesse, C. Etz, J. Henk, A. Ernst, I.V. Maznichenko, W. Hergert, and I. Mertig, "Tailoring Magnetic Interlayer Coupling in La$_{0.7}$Sr$_{0.3}$MnO$_3$/SrRuO$_3$ Superlattices," Phys. Rev. Lett. **104**, 167203 (2010).

[49] M. Ziese, I. Vrejoiu, and D. Hesse, "Inverted hysteresis and giant exchange bias in La$_{0.7}$Sr$_{0.3}$MnO$_3$/SrRuO$_3$ superlattices," Appl. Phys. Lett.**97**, 052504 (2010).

[50] M. Ziese , E. Pippel , E. Nikulina , M. Arredondo and I. Vrejoiu, "Exchange coupling and exchange bias in La$_{0.7}$Sr$_{0.3}$MnO$_3$-SrRuO$_3$ superlattices," Nanotechnology **22**, 254025 (2011).

[51] X. Ke, M. S. Rzchowski, L. J. Belenky, and C. B. Eom, "Positive exchange bias in ferromagnetic $La_{0.67}Sr_{0.33}MnO_3/SrRuO_3$ bilayers," Appl. Phys. Lett. **84**, 5458 (2004).

[52] X. Ke, L.J. Belenky, C.B. Eom, and M.S. Rzchowski, "Antiferromagnetic exchange-bias in epitaxial ferromagnetic $La_{0.7}Sr_{0.3}MnO_3/SrRuO_3$ bilayers," J. Appl. Phys. **97**, $10K115$ (2005).

[53] X. Ke, L. J. Belenky, V. Lauter, H. Ambaye, C. W. Bark, C. B. Eom and M. S. Rzchowski, "Spin Structure in an Interfacially Coupled Epitaxial Ferromagnetic Oxide Heterostructure," Phys. Rev. Lett. **110**, 237201 (2013).

[54] J.-H. Kim, I. Vrejoiu, Y. Khaydukov, T. Keller, J. Stahn, A. Ruhm, D. K. Satapathy, V. Hinkov and B. Keimer, "Competing interactions at the interface between ferromagnetic oxides revealed by spin-polarized neutron reflectometry," Phys. Rev. B **86**, 180402(R) (2012).

[55] S. Thota, Q. Zhang, F. Guillou, U. Lüders, N. Barrier, W. Prellier, A. Wahl, and P. Padhan, "Anisotropic magnetocaloric effect in all-ferromagnetic $La_{0.7}Sr_{0.3}MnO_3/SrRuO_3$ superlattices," Appl. Phys. Lett. **97**, 112506 (2010).

[56] M. Ziese, "A spin-calorics device based on $La_{0.7}Sr_{0.3}MnO_3/SrRuO_3$ superlattices," Phys. Status Solidi RRL **5**, No. 12, 444 (2011).

[57] M. Ziese, F. Bern, A. Setzer, E. Pippel, D. Hesse, and I. Vrejoiu, "Existence of a magnetically ordered hole gas at the $La_{0.7}Sr_{0.3}MnO_3/SrRuO_3$ interface," Eur. Phys. J. B **86**, 42 (2013).

[58] Heng-Jui Liu , Tzu-Chiao Wei , Yuan-Min Zhu , Rui-Rui Liu , Wen-Yen Tzeng , Chih-Ya Tsai , Qian Zhan , Chih-Wei Luo , Pu Yu , Jr-Hau He , Ying-Hao Chu , and Qing He, "Strain-Mediated Inverse Photoresistivity in $SrRuO_3/La_{0.7}Sr_{0.3}MnO_3$ Superlattices ", Adv. Funct. Mater., 26, 729 (2016).

[59] A. Vailionis, H. Boschker, Z. Liao, J. R. A. Smit, G. Rijnders, M. Huijben, and G. Koster, "Symmetry and lattice mismatch induced strain accommodation near and away from correlated perovskite interfaces," Appl. Phys. Lett. **105**, 131906 (2014).

[60] Wenlai Lu, Ping Yang, Wen Dong Song, Gan Moog Chow, and Jing Sheng Chen, "Control of oxygen octahedral rotations and physical properties in $SrRuO_3$ films," Phys. Rev. B **88**, 214115 (2013).

[61] M. Ziese, I. Vrejoiu, E. Pippel, E. Nikulina, and D. Hesse, "Magnetic properties of $Pr_{0.7}Ca_{0.3}MnO_3/SrRuO_3$ superlattices," Appl. Phys. Lett. **98**, 132504 (2011).

[62] J.W. Seo, W. Prellier, P. Padhan, P. Boullay, J.-Y. Kim, Hangil Lee, C.D. Batista, I. Martin, Elbert E.M. Chia, T. Wu, B.-G. Cho, and C. Panagopoulos, "Tunable

Magnetic Interaction at the Atomic Scale in Oxide Heterostructures," Phys. Rev. Lett. **105**,167206 (2010).

[63] P. Yua, W.Luo, D.Yi, J. X. Zhanga, M. D. Rossell, C.-H. Yan, L.You, G. Singh-Bhalla, S. Y. Yanga, Q.He, Q. M. Ramasse, R. Erni, L. W. Martin, Y.H.Chu, S. T. Pantelides, S. J. Pennycook, and R. Ramesh, "Interface control of bulk ferroelectric polarization," PNAS **109**, 9710 (2012).

Chapter 3

Experimental methods

3.1 Introduction

This chapter focuses on the different experimental techniques used for the growth and characterization of the epitaxial complex oxide films and their heterostructures as mentioned in this thesis. It starts with a brief description of the $SrTiO_3$ substrates treatment prior to the deposition of the heterostructures on them. The epitaxial thin film growth of oxide materials which are described in this thesis is done by Pulse Laser Deposition (PLD) technique. PLD is regarded as one of the most simple growth tools, both conceptually as well as experimentally, for single layer films as well as multi components oxide heterostructures due to stochiometic transfer of the materials from the target to substrate. In this method high power laser beam ablates the material from the target to grow the thin films. The growth of the monolayers can be followed by in-situ Reflection high-energy electron diffraction (RHEED), which provides information about the surface morphology of layers. Characterization of the thin films after fabrication is done by various techniques that include analysis of the crystal structure by X-ray diffraction (XRD) and the magnetic properties by superconducting quantum interference device (SQUID) magnetometer and X-ray circular magnetic dichroism (XMCD). To control the reversibly epitaxial strain, piezoelectric substrates are used.

3.2 $SrTiO_3$ substrate surface treatments

The perovskite $SrTiO_3$ (STO) is formed by two possible atomic termination planes, SrO and TiO_2 stacking along (001)-direction. Commercially available substrates show about 5% SrO termination and 95% TiO_2 termination [1]. For STO, non-acidic deionized (DI)-water treatment and thermal annealing have been used to prepare atomically flat and singly terminated surfaces . In this method, one of the surface oxides SrO is water-soluble [2]. By combining two thermal annealing steps after DI-water treatment, the process removes SrO terminated layers resulting in TiO_2 termination at the surface [3]. We took commercially available STO (001) single crystalline substrates (Crystec GmbH).
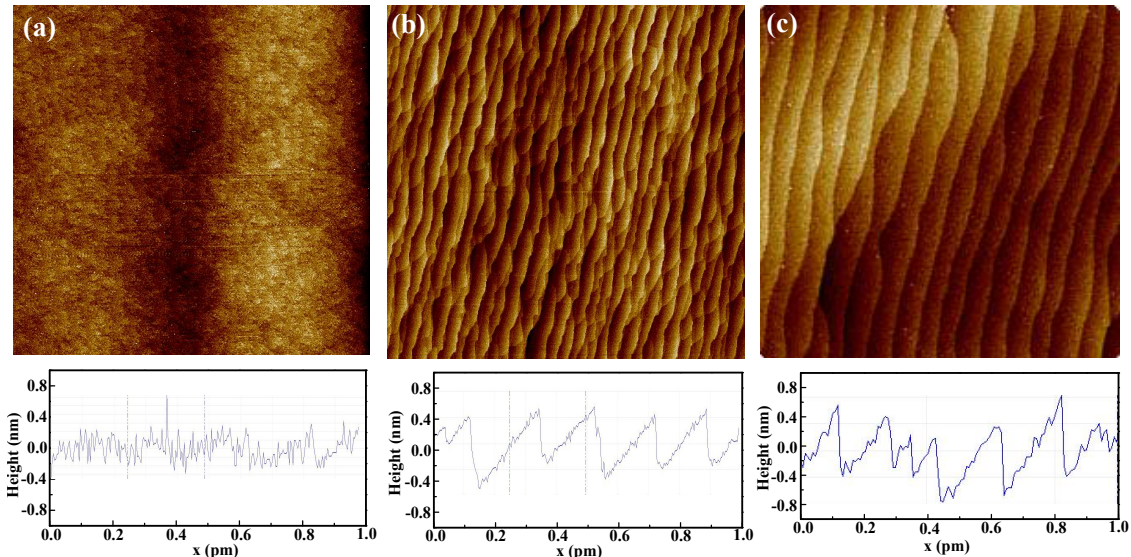
Figure 3.1: AFM topograpic image with their line profile (a) commercial STO (001) substrate, (b) after 1st annealing step, (c) after 2nd annealing step. Scan area is 5 x 5 μm^2.

Substrates are rinsed in DI water (resistivity >15 M Ωcm, pH =7.0 $\pm$ 0.2) by stirring for about 5 min at room temperature. Then substrates are annealed at 1200 $^{\circ}$ C (1st thermal annealing) for 8 h in air. The substrates are then again rinsed in DI water for 5 min and annealed again at 1200 $^{\circ}$ C (2nd thermal annealing) for 8 h in air. The surfaces of the substrates were characterized after annealing process using Bruker Multimode 8 atomic force microscopy (AFM). Fig.3.1 illustrates the surface of the commercial STO (001) substrate before and after annealing. Fig.3.1 (a), (b) and (c) shows AFM image of commercial STO (001) substrate, after 1st annealing and 2nd annealing of the substrate, respectively. Fig.3.1 (b) and (c) supports the hypothesis as the water soluble SrO have been removed by DI-water treatment and thermal annealing technique since single steps are observed in AFM. After 2nd annealing, an atomically flat surface has been produced by the process with a step height of $\sim$4 Å and roughness of approximately 0.2 Å. The step height tells that the substrate is single termination TiO$_2$ which was confirmed by coaxial impact-collision ion scattering spectroscopy (CAICISS) measurements reported in ref. [1].

3.3 Pulsed Laser Deposition (PLD)

In PLD, the process of laser ablation is aided by the photons hitting the target to melt, evaporate and ionize the material from the surface of a target. As a result, a highly luminous dense vapor beam, called the plasma plume, is formed that expands rapidly away from the target surface towards the substrate [4, 5, 6]. The targets are rotated in the focal plane of the laser beam and the target carousel moves with translational motion to achieve a stationary ablation rate. The substrate itself is held stationary or is rotated for homogeneous deposition rate. The kinetic energy of the particles arriving
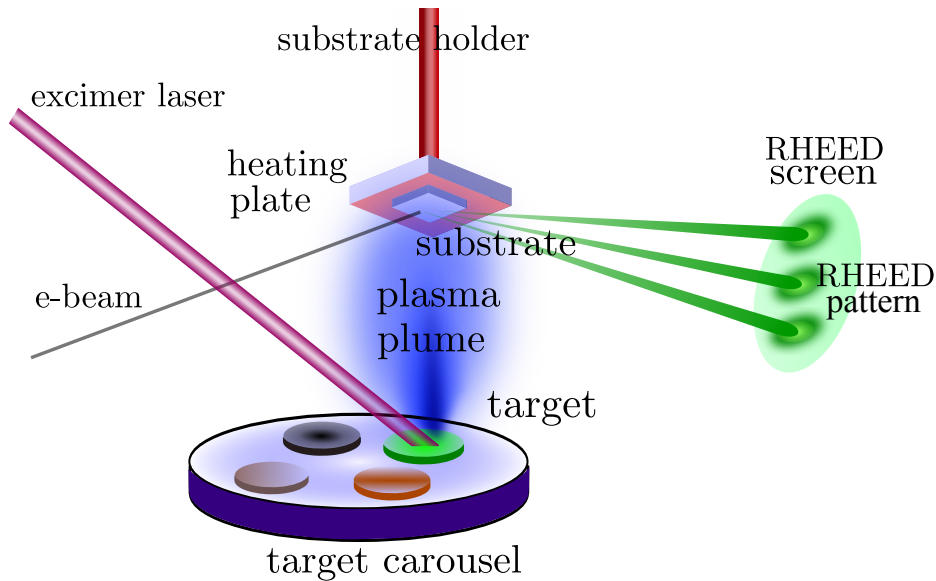
Figure 3.2: Schematic diagram of PLD setup of chamber II.

at the substrate can be controlled by background pressure. If a background gas such as argon or oxygen is used, the ablated particles interact with the gas before hitting the substrate which ensures the particles in the plasma plume to be nealy thermalised at the time they reach the substrate. Once the ablated material is collected on an appropriately placed substrate surface, the surface diffusion and desorption probabilities of the particles are controlled by substrate temperature. Then it condenses and the thin film grows.

The main advantages of PLD are: i) stochiometric transfer of most target materials onto the substrate, ii) highly controllable deposition rate by tuning the deposition parameters such as target to substrate distance, substrate temperature, gas pressure, laser energy etc., iii) as the laser source is outside the deposition chamber, it introduces minimal contamination to the grown film. The source of oxygen is used for proper control of oxygen content during growth of oxide materials.

The sequential ablation of material from multiple targets is used to form the heterostructures or superlattices where one layer is deposited before switching to the layer of the next material. In case of heterostructures or superlattices, the roughness of the each interface must be significantly smaller than the thickness of individual layers. Prior to starting the growth of multiple layers, it is crucial to calibrate the growth rate of each material or track the number of layers by RHEED.

3.3.1 PLD chamber set-up

A schematic picture of the deposition chamber II is shown in Fig.3.2. All films are deposited by using the KrF excimer laser with wavelength 248 nm, which operates at repetition frequencies of 1-10 Hz and pulse duration of about 20-50 ns. The maximum pulse energy is 700 mJ. A homogenous part of the laser beam is selected by using an aperture, which is projected onto the target by focusing lens. By varying both, the laser

Table 3.1: Deposition conditions of the various sample types in the off-axis chamber I and RHEED chamber (chamber II). T denotes the substrate temperature, P_{O2} is backgound oxygen pressure, f is the laser pulse frequency and E is the laser energy density.

Chamber I

Sample	Substrate	T (°C)	P_{O2} (mbar)	f (Hz)	E (J/cm^2)
[LSMO/SRO]$_{15}$ SL	STO	650	0.1	3	2.5
	PMN-PT	650	0.1	3	2.5
	STO	700	0.1	3	2.5
	PMN-PT	700	0.1	3	2.5
[LCMO/SRO]$_{15}$ SL	STO	650	0.1	3	2.5
	LAO	650	0.1	3	2.5
	PMN-PT	650	0.1	3	2.5
[LCMO/STO]$_{15}$ SL	STO	650	0.1	3	2.5
	LAO	650	0.1	3	2.5
	PMN-PT	650	0.1	3	2.5

Chamber II

Sample	Substrate	T (°C)	P_{O2} (mbar)	f (Hz)	E (J/cm^2)
SRO/LSMO Bilayer	STO	700	0.2	3	0.3
LSMO/SRO Bilayer	STO	700	0.2	3	0.3

energy and the spot size on the target, the energy density at the target can be adjusted. The pressure in the vacuum system during deposition is controlled by the rotary pump and turbomolecular pump. For the background gas, O_2 is used. The chamber contains a target carousel, on which up to 4 targets can be mounted.

The investigated films in this work have been grown in two different PLD chambers. In chamber I, the films are grown by off-axis geometry [7]. The substrate holder is held 90 degree angle to the target surface. A cylindrical oven is used to heat the substrate and the substrate holder is rotated during the deposition in order to assure a homogeneous distribution of materials on the substrate surface. A rotary pump and turbo pump are used to evacuate the chamber lowering the base pressure down to $P_b = 10^{-4}$-10^{-5} mbar. The deposited materials and their exact deposition conditions are summarized in Table 3.1.

In chamber II, the films are deposited by the standard on-axis geometry. In-situ RHEED is used during the deposition to analyze the surface morphology of the films and track the number of deposited layers. The substrates are glued by silver paste onto the heater plate which can heat up to 900 °C. A turbo pump evacuates the chamber to the base pressure of $P_b = 10^{-6}$-10^{-7} mbar. The deposited materials and their exact deposition conditions are summarized in Table 3.1 chamber II.

3.4 Structural characterization

The morphology of the surface and the lattice structure of the film can be monitored during and after the growth of the film by using the RHEED. After growth, the crystalline structure of the film is characterized by $ex-situ$ x-ray diffraction (XRD).

3.4.1 *In-situ* reflection high-energy electron diffraction

Reflection high-energy electron diffraction (RHEED) is a powerful technique for studying the growth dynamics and surface morphology of complex oxides. RHEED is sensitive to surface roughness, interface properties and phase stability [8, 9, 10]. $In-situ$ RHEED can be done along with pulsed laser deposition (PLD), where an accelerated electron beam of 30 keV is incident on the surface with a glancing angle < 3 degee and is reflected. A schematic of the RHEED setup is shown in Fig.3.2. During the deposition, the electron beam is focused onto the surface under a grazing angle and a phosphor screen combined with a CCD camera was used to measure the intensity of reflected electrons.

The electrons are diffracted from sample surface. The crystal structure of a surface layer of the film gives rise to a diffraction pattern (intersection of the reciprocal lattice rods with the Ewald sphere) on the RHEED screen. The electrons interact with the topmost atomic layers (1-2 nm) only, therefore RHEED is a surface sensitive technique. The diffraction patterns provide essential information about the crystal structure and the morphology of the film surface [11, 12].

During the deposition of thin film on a substrate one can follow the time variation of the intensity of the specular spot. The intensity oscillations are observed during the layer-by-layer growth mode where period of the oscillations corresponds to one atomic layer of the material. If a surface is atomically flat, then sharp RHEED patterns are seen. If the surface is rough, the RHEED pattern is more diffuse.

3.4.2 X-ray Diffraction (XRD)

X-ray diffractometer is a sophisticated tool to get information regarding the crystalline structure of thin film, powder or bulk form of the materials. The XRD results reported in this thesis have been obtained on the Phillips X'pert MRD diffractometer with Cu $K\alpha$ radiation (λ=1.54Å) and Bruker D8 Discover diffractometer with Cu $K\alpha$ radiation (λ=1.54Å). To know the crystalline structure, XRD can be performed in several different scans such as low angle 2θ-ω scan to determine the thickness, roughness of the sample, high angle 2θ-ω scan which gives the out-of-plane lattice parater of the sample and strain state of the materials as captured in the reciprocal space map (RSM). For simple configuration of XRD, the x-ray source is fixed while the sample holder and the detector can be rotated with an angle ω and 2θ, respectively. Also independent rotation of the sample are possible by changing the angles ω, ψ and ϕ (Fig.3.3). The following different types of XRD measurements have been applied.

3.4.2.1   X-ray reflectivity

Low-angle measurement called X-ray reflectivity (XRR) is used to determine the thickness of the thin films. In XRR measurement, the diffractometer is used in the 2θ-ω configuration at low angles of 2θ, typically from $0°$ to $5°$. In the obtained diffraction pattern, we can see regular intensity oscillations called Kiessig oscillations or Kiessig fringes which are equidistant from each other. These oscillations are due to the interference between the reflected ray from the film surface and that from the interface between the film and the substrate. Therefore, the distance between the oscillations reveals information about the thickness of the sample. The total thickness of the sample is estimated by the following equation,

$$d = \lambda/(2\triangle\theta) \tag{3.1}$$

Where λ is the x-ray wavelength and $\triangle\theta = \theta_i - \theta_{i-1}$ with θ_i being the angle of the ith order fringe. It is difficult to measure thickness above 70 nm by using Cu $K\alpha$ radiation due to small angular resolution.

In low angle XRD measurements of a periodic structure like superlattices, two types of fringes are observed, one is associated with the superlattice period, Λ (i.e. large interference maxima called superlattice peak) and other with the total thickness of the periodic film stack, d. Ideally, if the superlattice consists of N double layers there are $N-2$ small fringes between two adjacent large superlattice peaks. The reflectivity spectrum exhibits the superlattice peaks which are coming from the chemical modulation of the sample with additional Kiessig fringes related to the total thickness of the sample [13]. The superlattice period, Λ (double layer thickness) can be determined using the equation 3.2. One can use the reflectivity simulation to calculate the individual layer thickness and roughness.

3.4.2.2 2θ-ω scan

The 2θ-ω scan is used to determine the orientation of the film with respect to the substrate, the structure and phase of the films, and the out-of-plane lattice parameter of the films. In 2θ-ω scan, the diffractometer is performed at high angles of 2θ, typically about $20°$ to $120°$, depending on the sample and the aim of the measurement. The x-ray beam is incident at an angle ω with respect to the surface plane [Fig.3.3 (a)]. The intensity of the reflected beam is measured at an angle 2θ with respect to the incident beam.

During the measurement, a peak is observed at a certain angle 2θ when the Bragg condition is satisfied:

$$2\mathrm{d}_{hkl}\sin\theta = n\lambda \tag{3.2}$$
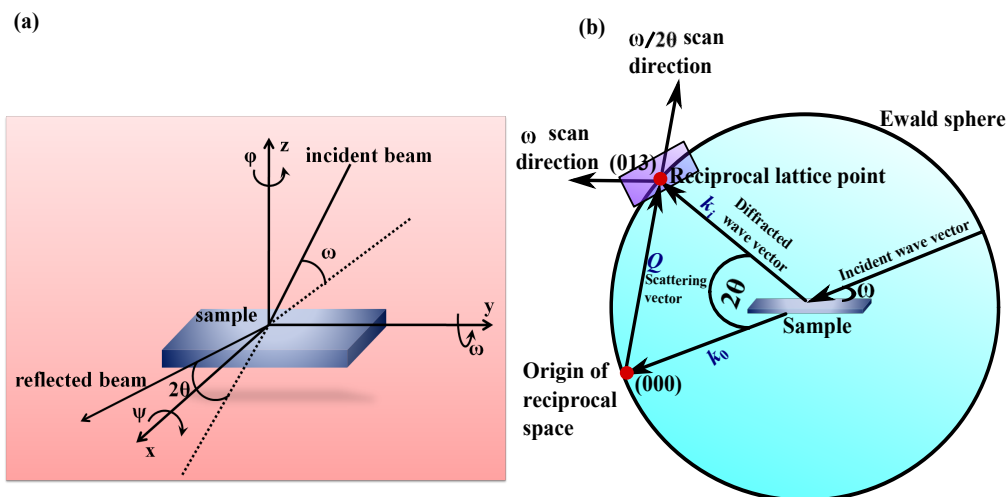
Figure 3.3: (a) Geometry of XRD measurements, (b) Schematic representation of RSM.

Where n is any integer number, λ is the wavelength (1.5406 Å), d_{hkl} is the lattice spacing of a set of crystallographic planes parallel to the film plane (hkl are the Miller indices). One can calculate the out-of-plane lattice parameter (c) in Cubic lattice by d_{hkl} $=c/\sqrt{(h^2+k^2+l^2)}$.

The 2θ-ω diffraction pattern for superlattice show several satellite peaks around main peak which indicates that the superlattice are periodic structure having sharp interfaces, albeit qualitatively. One can calculate the modulation period of the superlattice from the Laue diffraction using

$$\Lambda = (n_i - n_{i-1})\lambda/[2(\sin\theta_i - \sin\theta_{i-1})] \tag{3.3}$$

where n_i as the number corresponding to i^{th} order oscillation of the fringe, θ_i is the angle of that particular i^{th} order fringe.

3.4.2.3 Reciprocal space maps

Reciprocal space map (RSM) is used to study and determine the structural properties such as lattice parameters, strain relaxation and structural quality of epitaxial thin films. The RSM is a contour mapping of the XRD signal peak intensity. It records the intensity distribution in the vicinity of the Bragg peak. RSM is realized as a series of ω-2θ scans taken at different offsets around a Bragg reflection. As a result, the two dimensional intensity map, so called reciprocal space map is obtained. Fig.3.3 (b) schematically represents the execution of such a map. The scattering vector should coincide with a surface normal to a scattering crystal plane, which corresponds to reciprocal lattice point. k_0 is stationary under all circumstances while sample and detector must be rotated (ω-2θ scans) to change the orientation of the scattering vector Q. However, ω scans change the direction of the scattering wave vector but keeps the magnitude of Q constant. Angle

dependent intensities are collected in real space and transformed into reciprocal space and one gets the RSM of the particular Bragg reflection and its vicinity.

One can calculate the reciprocal lattice vector components from the coordinate position (q_x, q_y) of any (hkl) reciprocal lattice point, [14]:

$q_x = 2/\lambda \sin\theta \sin(\theta - \omega)$, $q_y = 2/\lambda \sin\theta \cos(\theta - \omega)$;

Where λ is the X-ray wavelength, ω is the angle between primary X-ray beam and the sample surface, and 2θ is the angle between incident and diffracted X-ray beams. For example, one can calculate the a and c lattice parameters by, $a = 1/q_x$; $c = 3/q_y$ in the (103) point. For a cubic film, if $c/a > 1$, the film shows compressive strain state; $c/a < 1$, the film is under tensile strain and when $c/a = 1$, the film is relaxed. In case of multilayers the difference in a and c parameters between the superlattice and the substrate represents as a peaks separation ("average" peak of superlattice and the substrate peak) along the q_x and q_y axes in RSM.

3.4.3   Atomic Force Microscopy

To characterize the surface morphology of the substrates and films, Bruker Multimode 8 atomic force microscopy (AFM) has been used. A typical AFM setup is shown in Fig.3.4 (a). It has been operated at room temperature in atmospheric pressure in Peak Force (PF) tapping mode with Scan Asyst Air tip (tip radius $\simeq$ 2 nm and 0.2-0.8 N/m force constant). In PF mode, the tip is scanned over the area of interest on the specimen while force distance curves of the cantilever are measured with 2 kHz frequency with very low contact forces $\simeq$ 1 nN on the surface. Due to attractive and repulsive forces between cantilever and tip the cantilever therefore becomes deformed perpendicular to the surface. By detecting and analyzing this deformation with an optical laser beam on the cantilever the tip surface distance can be adjusted by the Feedback control system to maintain a constant maximum force and the height profile of surface can be measured with atomic resolution.

3.4.4   Transmission Electron Microscopy

Transmission electron microscopy (TEM) is used primarily for structural and chemical characterization of the specimen. In this thesis, we use the TITAN 80-300 (FEI) Scanning Transmission electron microscopy for imaging which is done in collaboration with Prof. Dr. Eckhard Pippel, MPI Microstructure Physics, Halle, Germany. TEM is a microscopy technique in which a beam of electrons is transmitted through an ultra-thin specimen which interacts with the specimen as it passes through. An image is formed from the interaction of the electrons transmitted through the specimen. The image is magnified and focused onto an imaging device, such as a fluorescent screen or to be detected by a sensor such as a CCD camera. TEMs are capable of imaging at a significantly higher resolution than light microscopes, owing to the small de Broglie wavelength of electrons.
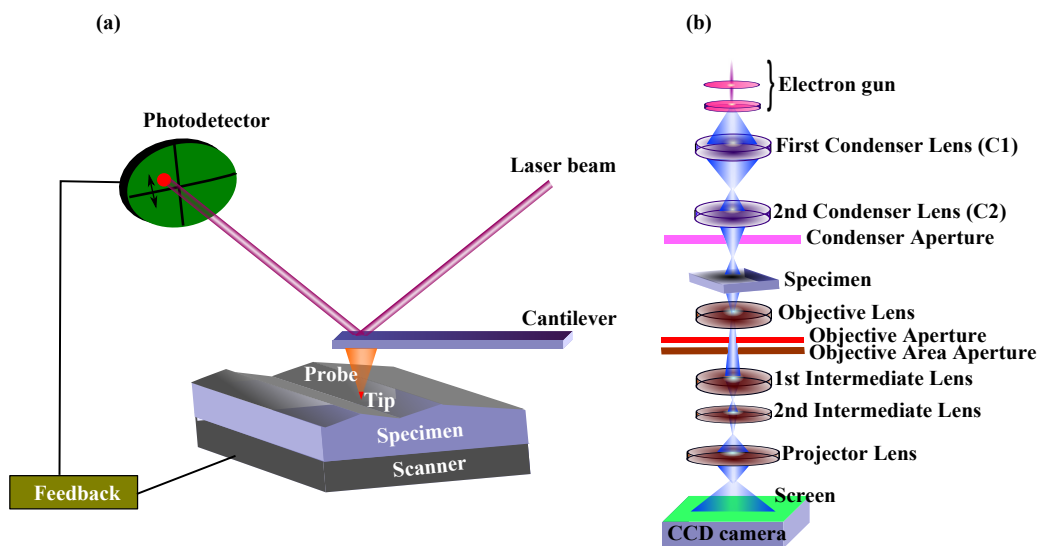
Figure 3.4: (a) A schematic view of an Atomic Force Microscope. A feedback system keeps a tip in contact with the sample, (b) Illustration of the TEM lens system [15]

According to the Rayleigh criterion, the smallest resolvable distance for a visible light microscope is given by, $\delta = 0.61\lambda/\mu\sin\beta$, where δ is the resolvable distance, λ is the wave length of light, μ is the refractive index of viewing medium and β is the semi-angle of the magnifying lens [15]. The resolvable distance for visible light is in range 200 -400 nm which is much larger than the most nanostructures.

To resolve the smaller feature size, one would need to shorten the wave length of incident radiation which is possible by using the electron instead of light. One can estimate this according to de-Broglie, $\lambda = 1.22/\sqrt{E}$, where E is the energy of electron in eV [15]. For a 100 keV electron this yields a theoretical wavelength of 0.004 nm, which is smaller than an atom. Such energies are routinely attainable in a modern electron microscope shown in Fig.3.4 (b). The main parts of the microscope are the electron gun, focusing optics, specimen, and collection optics [15]. The high spatial resolution of the probe makes TEM a highly effective means to probe local atomic-scale structure and chemistry.

3.4.4.1 Scanning Transmission Electron Microscopy

Scanning Transmission Electron Microscopy (STEM) is a variant of traditional TEM in which the incident optics are arranged in such a way as to converge the beam at the sample position. In particular, the second condenser lens (C2) is turned off and a third condenser (C3) is used to focus and converge the beam to a small spot on the sample which is scanned over the sample in a raster [15].

There are many benefits of using a STEM imaging mode. STEM allows the user to get the highest possible spatial resolution of any real-space imaging mode, as well as simultaneous measurement of local chemistry, bonding, and valence [16]. In addition, the use of a high-angle annular dark field (HAADF) detector allows the user to isolate electrons scattered to high angles. It is found that the probability of such scattering is proportional to the atomic number (Z) of the scattering atoms and is termed "*Z*-contrast"
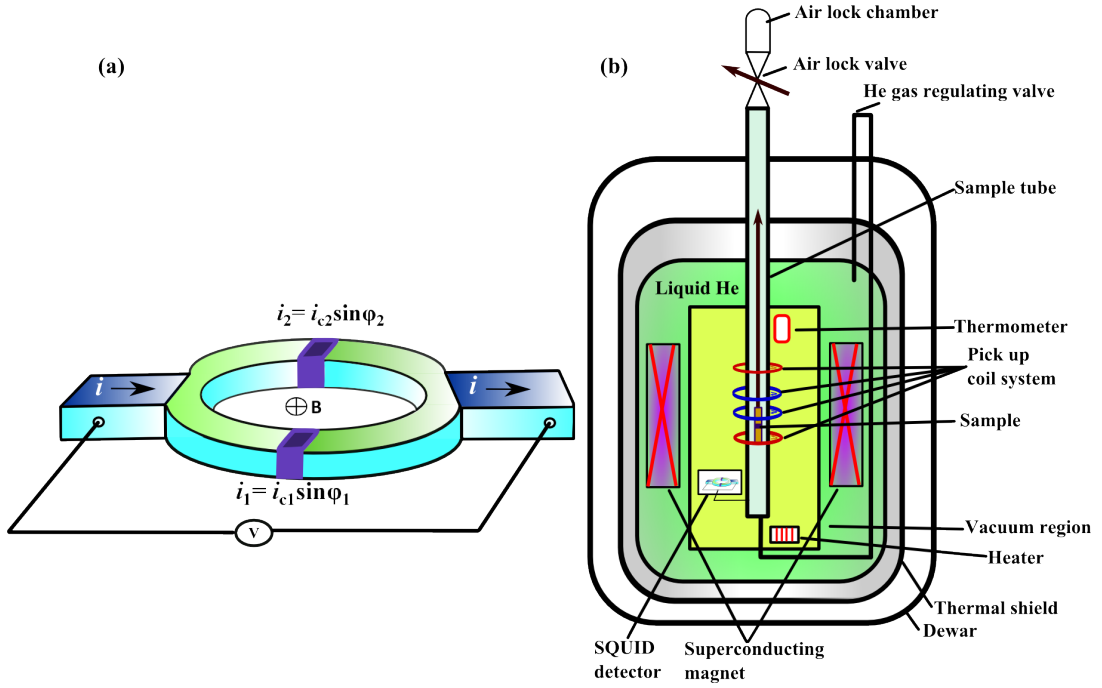
Figure 3.5: Schematic diagram of (a) Josephson junction, (b) SQUID Magnetometer.

imaging. This contrast mechanism allows the user to easily distinguish regions of high and low atomic number.

3.5 Magnetic characterization

3.5.1 Superconducting Quantum Interference Device

We use the superconducting quantum interference device (SQUID, Quantum design, 5 T) to measure the magnetization (M) of the films. SQUID magnetometer is consisting of several superconducting (SC) components such as: SC magnet generating high magnetic fields, SC pick-up coils placed at the center of the SC magnet and the SQUID detector [Fig.3.5]. The working principle of SQUID is based on the magnetic flux quantization in the SC ring and on Josephson junction [17].

The SQUID detector is performed as a superconducting ring with two parallel Josephson junctions (JCs) [Fig.3.5]. When the sample is moved through the SC detection coils the magnetic dipole moment of the sample induces an electric current and a phase difference in the electron-pair wave appears across the junctions. The phase difference of the electron-pairs wave functions over JCs with the magnetic flux penetrating the SC ring is connected by the below expression,

$$i = 2i_c \mid \cos \pi \phi / \phi_0 \mid \qquad (3.4)$$

Where i is induced current, i_c is a critical current over the JC, ϕ is the flux produced
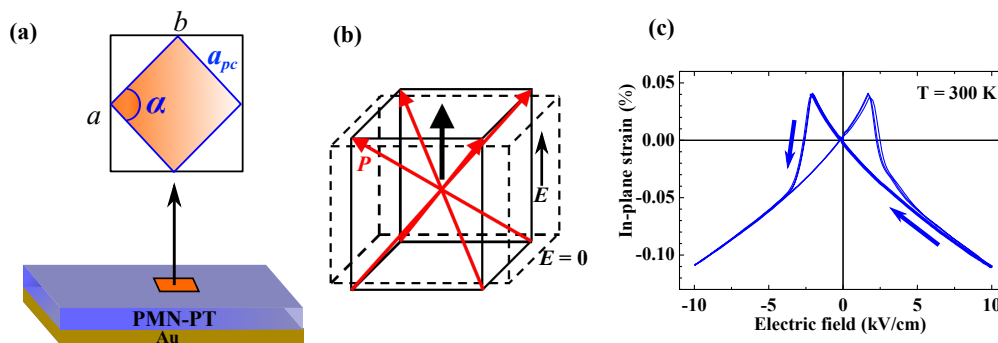
Figure 3.6: (a) Schematics of pseudocubic surface lattice of PMN-PT in the poled state, (b) Schematic diagram of domain configuration in (001)-oriented rhombohedral PMN-PT crystal under electric field E. (c) In-plane piezoelectric strain vs applied electric field E ||(001) hysteresis of a PMN-PT (001) substrate at room temperature (taken from ref.[21]).

in the ring by the applied magnetic field and $\phi_0 = h/2e = 2.07 \times 10^{-15}$ [Wb] is flux quantum. This flux signal from the SQUID is detected in terms of voltage while the sample is scanned trough the detection coils which is further amplified and processed to magnetic moments in units of emu. Moments as low as 10^{-7} emu can be measured in our Quantum Design SQUID. The SQUID is used to measure the temperature, magnetic field and reversible strain dependence of magnetic moment of the sample. We can vary the measurement temperature from 10 K to 350 K, and the applied magnetic field can be swept from +5 T to −5 T. The Curie temperature has been estimated by extrapolating the linear part of M^2 vs T curve to M=0.

3.5.2 Strain-dependent magnetization

To measure the direct strain dependence of magnetization, we use the films grown on piezoelectric PMN-PT substrate. Poled PMN-PT $(001)_{pc}$ crystals have a monoclinic M_A structure, with the ferroelectric polarization P near a body diagonal to the pseudocubic cell [Fig.3.6 (a)]. Thus, crystals poled along $(001)_{pc}$ contain four different domain variants with a stable domain configuration under E ||$(001)_{pc}$ [Fig.3.6 (b)] [18].

The in-plane angle between the $[100]_{pc}$ and $[010]_{pc}$ planes is estimated as $\alpha = 89.92°\pm 0.03°$ for $E \leq 13.3$ kV/cm, revealing a tiny deviation from a quadratic surface lattice, similar to that of LAO (001) substrates [Fig.3.6 (a)]. Thus, the domain pattern on the surface of the substrate produces only a small distortion that can be neglected for most of the studies. Fig.3.6 (b) schematically presents the ferroelectric domains and their piezo-electric response under bias (electric field) for rhombohedral crystals poled along <001>. When actuation is induced by an E field along <001>, the polar direction is expected to incline to the E-field direction in each domain. PMN-PT is nearly cubic (pseudocubic) in the unpoled state, and the large multi-domain crystals show low-hysteresis strains [Fig.3.6 (c)]. In order to avoid the hysteresis, most experiments are carried out at $E_{max}> E> 0$ after applying E_{max} to the crystal.

For providing electrically controllable reversible biaxial strain, a silver paint contact

(a)

(b)
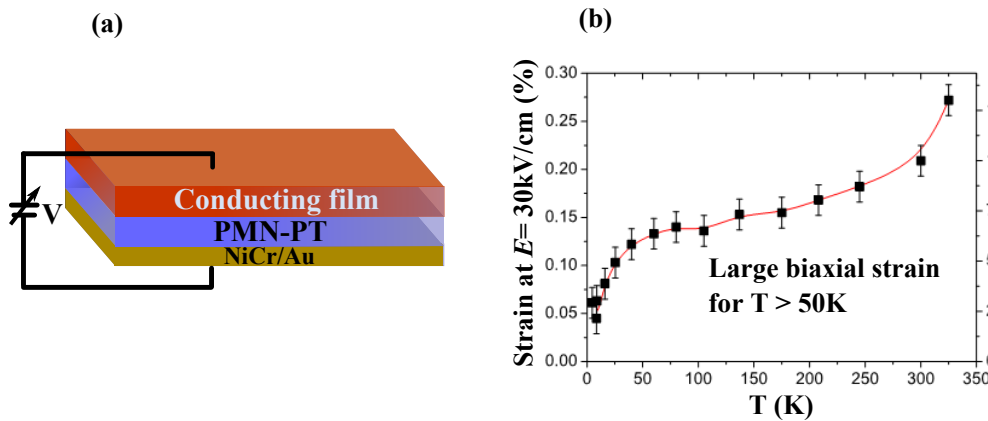
Figure 3.7: (a) Schematic diagram of reversible strain application. (b) Temperature dependence of the piezoelectric in plane-strain of PMN-PT substrate (taken from ref.[22]).

on top of the sample and a NiCr/Au electrode on the bottom face of the 0.3 mm thick PMN-PT crystal are used. These facilitate applying an electric field of $E \leq 10$ kV/cm normal to the substrate [Fig.3.7 (a)]. After properly poling the crystal at 10 kV/cm, the resulting current through the piezo-crystal is < 1 µA. The PMN-PT substrate shrinks approximately linearly with increasing substrate voltage along both [100] and [010] in-plane directions, undergoing a compression of about 0.1% in an electric field of E=10 kV/cm [19, 20]. For reversible strain dependent measurement we use a modified sample holder for the SQUID magnetometer. Such sample holder has additional voltage contacts at the sample position where the wires are connected to the sample. During the measurement, the magnetization of the NiCr/Au electrode of the PMN-PT can be neglected compared to the signal from manganite films and their heterostructures.

Fig.3.7 (b) shows the temperature dependence of the substrate strain at E=30 kV/cm. The piezoelectric effect is commonly decreasing with decreasing temperature for lead based ferroelectrics. Below 50 K the strain drops distinctly to about 25% of the room temperature value. At $T > 50$K, there is large biaxial strain. That is why in most of our strain dependent measurement we restrict to $T> 50$K [22]. It should be noted that the low temperature decrease in the piezoelectric strain is subject to some degree of variation, most likely due to minor scattering of compositions between the crystals [22].

3.6   X-ray absorption spectroscopy

X-ray absorption spectroscopy (XAS) is an extremely powerful and element sensitive technique which provides the information for determining the local geometric and/or electronic structure of specific element of the material investigated. The experiment is usually performed at synchrotron radiation sources, which provide intense and tunable X-ray beams. XAS data are obtained by tuning the photon energy of the incident monochromatic radiation to a specific range where core electrons can be excited (0.1-100 keV photon energy). The absorption will have very strong peaks when the photon energy is exactly able to

excite certain energy level to the unoccupied states. This is called absorption edges. The "edge" depends upon the core electron which is excited: the principal quantum numbers $n = 1$, 2, and 3, correspond to the K-, L-, and M-edges, respectively. For instance, excitation of a $1s$ electron occurs at the K-edge, while excitation of a $2s$ or $2p$ electron occurs at an L-edge. An x-ray absorption spectrum (XAS) can be measured in two different detection modes: total electron yield (TEY) and total fluorescence yield (TFY) mode. In TEY mode, the total number of electrons (photoelectrons, Auger electrons, secondary electrons) emitted from the sample are counted. Since the mean free path of the electrons is very small the TEY mode is surface sensitive. In the TFY mode the number of emitted fluorescence photons (after the hole is filled by an electron from an outer shell) are counted at each energy level of the impinging photons. TFY mode provides bulk information of the materials.

3.6.1   X-ray magnetic circular dichroism

X-ray magnetic circular dichroism (XMCD) is a powerful element-selective magnetrometry technique [23]. XMCD is the difference of two XAS spectra taken in a magnetic field, one taken with left circularly polarized light, and the other with right circularly polarized light. In this thesis XMCD is used to extract the information regarding the magnetic properties of the specific atom investigated.

In this thesis, the XAS and XMCD experiments are performed in collaboration with Stefano Agrestini, Ziwei Hu (MPI CPfS, Dresden) at the BL29 BOREAS beamline at the ALBA synchrotron radiation facility in Barcelona with its high-field. The magnetic field up to 7 T can be applied during the measurements. It covers a photon energy ranging from 0.5 keV to 4 keV and thus enables us to measure both Ru- $L2,3$ edges and the Mn-$L2,3$ edges.

Bibliography

[1] M Kawasaki, K Takahashi, T Maeda, R Tsuchiya, "Atomic control of the SrTiO$_3$ crystal surface," Science **266**, 1540 (1994).

[2] J. H. Ngai, T. C. Schwendemann, A. E. Walker, Y. Segal, F. J. Walker, E. I. Altman, and C. H. Ahn, "Achieving A-Site Termination on La$_{0.18}$Sr$_{0.82}$Al$_{0.59}$Ta$_{0.41}$O$_3$ Substrates," Adv. Mater. **22**, 2945 (2010).

[3] J. G. Connell, B. J. Isaac, G. B. Ekanayake, D. R. Strachan, and S. S. A. Seo, "Preparation of atomically flat SrTiO$_3$ surfaces using a deionized-water leaching and thermal annealing procedure," Appl. Phys. Lett. **101**, 251607 (2012).

[4] P. R. Willmott and J. R. Huber, "Pulsed laser vaporization and deposition," Rev. Mod. Phys. **72** (1) (2000).

[5] R. K. Singh and J. Narayan, "Pulsed-laser evaporation technique for deposition of thin films: Physics and theoretical model," Phys.Rev.B, **41**(13) (1990).

[6] A. Miotello, R. Kelly, "Laser-induced phase explosion: new physical problems when a condensed phase approaches the thermodynamic critical", Appl.Phys.A **69**, S67 (1999).

[7] B. Holzapfel, B. Roas, L. Schultz, P. Bauer, G. Saemann-Ischenko, "Off axis laser deposition of YBa$_2$Cu$_2$O$_{7-\delta}$ thin films," Appl. Phys. Lett, **61**, 3178 (1992).

[8] K. Britze and G. M. Ehmsen, "High energy electron diffraction at Si(001) surfaces," Surface Science **77**, 131-142 (1978).

[9] M. Itoh, "Relation between surface reconstructions and RHEED intensity oscillations," Phys. Rev. B, **58**, 6716 (1998).

[10] Braun W, "Applied RHEED Reflection High-Energy Electron Diffraction During Crystal Growth," Springer-Verlag: Berlin (1999). pp. 14–17, 25, 75. ISBN $3-540-65199-3$.

[11] W. Unertl, editor. Physical Structure volume 1, Elsevier 1st editio edition (1996).

[12] G. Koster and G. Rijnders, "In situ characterization of thin film growth," Woodhead Publishing, Limited (2011), ISBN $978-0-85709-495-7$ (onlne).

[13] L.G. Parratt, "Surface studies of solids by total reflection of X-rays," Phys. Rev. **95**, 359 (1954).

[14] P. F. Fewster: X-ray scattering from semiconductors. Imperial College Press (2003)

[15] D.B.Williamsand C.B.Carter, "Transmission Electron Microscopy" Springer, 2009.

[16] R Egerton. Physical Principles of Electron Microscopy: An Introduction to TEM, SEM, and AEM. Springer, 2008.

[17] R. C. Jaklevic, J. Lambe, A. H. Silver, J.E. Mercereau, "Quantum interference effects in Josephson tunneling," Phys. Rev. Lett. **12**, 159 (1964).

[18] S.E.Park and T.R.Shrout, "Ultra high strain and piezoelectric behavior in relaxor based ferroelectric single crystals," J. Appl Phys **82**,1804 (1997).

[19] M.D. Biegalski, D.H. Kim, K.Dörr, H.M.Christen, "Applying uniform reversible strain to epitaxial oxide films," Appl. Phys. Lett. **96**,151905 (2010).

[20] K. Dörr , O. Bilani-Zeneli, A. Herklotz, A. D. Rata, K. Boldyreva, J.-W. Kim, M. C. Dekker, K. Nenkov, L. Schultz, M. Reibold, "A model system for strain effects: epitaxial magnetic films on a piezoelectric substrate," Eur.Phys.J.B **71**, 361 (2009).

[21] C. Thiele, K. Dörr, O.Bilani, J.Rödel, and L. Schultz, "Influence of strain on the magnetization and magnetoelectric effect in $La_{0.7}A_{0.3}MnO_3$ /PMN-PT (001) (A=Sr,Ca)," Phys. Rev. B **75**, 054408 (2007).

[22] A.Herklotz, J.D.Plumhof, A.Rastelli, O.G.Schmidt, L.Schultz, and K.Dörr, "Electrical characterization of PMN–28%PT (001) crystals used as thin-film substrates," J. Appl. Phys., **108**, 094101 (2010).

[23] J. Stohr, "Exploring the microscopic origin of magnetic anisotropies with X-ray magnetic circular dichroism (XMCD) spectroscopy," Journal of magnetism and magnetic materials, **200**, 470 (1999).

Chapter 4

Strain dependence of antiferromagnetic interface coupling in La$_{0.7}$Sr$_{0.3}$MnO$_3$/ SrRuO$_3$ superlattices

This Chapter presents details of the magnetic response of $La_{0.7}Sr_{0.3}MnO_3/SrRuO_3$ superlattices to biaxial in-plane strain applied $in-situ$ and reveals a signicant strain effect on interfacial coupling.

4.1 Introduction

Magnetic order and coupling at coherent interfaces between oxides of perovskite type have received increasing interest during the last decade. This also includes a renewed quest for phenomena that were discovered earlier in context of metal films such as exchange bias effect between a ferro- and an antiferromagnetic layer [1] and the interlayer coupling through non-magnetic spacer layers responsible for giant magnetoresistance in Co/Cu/Co and many others [2, 3]. The new phenomena have been discovered that are similar to realization of two-dimensional electronic states at semiconductor interfaces but add the surprising new interfacial magnetic degree of freedom [4]. The most prominent example is the observation of a conducting electron gas at the interface between the insulators LaAlO$_3$ and SrTiO$_3$ [5, 6]. Alongside the transport properties, magnetic behavior of an interface also can differ drastically from that of the individual components. The interface of ferromagnetic SrRuO$_3$ (SRO) with ferromagnetic manganites such as La$_{0.7}$Sr$_{0.3}$MnO$_3$ (LSMO), for example, is now a focus of interest because it shows a strong antiferromagnetic coupling which, so far is unparalleled in the family of oxides [7]. The antiferromagnetic exchange coupling at the interface leads to opposite orientation of the magnetizations of thin adjacent SRO and LSMO layers and can withstand a magnetic field up to several Tesla [7, 8, 9]. The strong reduction of magnetic order at LSMO surfaces or interfaces termed as "dead layer" in previous work[10] seems to be weak or absent at the LSMO/SRO interface as noted in Ref.[11]. Subsequent work showed the complexity

of magnetic order arising from combination of the antiferromagnetic interface coupling with magnetic anisotropies of the components which are perpendicular to the film plane and strong for SRO and in-plane and weak for LSMO on $SrTiO_3(001)$ substrates, respectively. An inhomogeneous magnetization depth profile with in-plane Ru spins near the interface and perpendicular Ru spins inside the SRO layer has been derived from neutron reflectivity measurements [12]. The magnetic order at low temperatures depends heavily on the cooling history of samples [13]. One reason for this is the alignment of Ru spins during cooling through $T_C^{SRO} \sim$150 K according to the more dominant energy of either (i) the exchange coupling to ordered Mn spins ($T_C^{LSMO} \geq$250 K) at the interface, or (ii) the magnetic anisotropy energy of SRO, or (iii) the Zeeman energy in an applied magnetic field [13]. At low temperatures, the magnetic anisotropy of SRO is so large that full alignment of Ru spins is hard to achieve in applied magnetic fields of a few Tesla. Hence, the arrangement of Ru spins during cooling is (partially) "frozen in".

Meaningful investigation of magnetic coupling at oxide interfaces has been enabled by the advance of experimental tools such as RHEED-assisted layer-wise growth under high oxygen pressure [14] and scanning transmission electron microscopy (STEM). The latter allows for semi-quantitative evaluation of chemical intermixing at interfaces by applying the high angle annular dark field technique (HAADF) [15, 16]. Thermal diffuse electron scattering at high angles (>70 mrad) is recorded with the intensity of the localized, incoherent scattering processes proportional to Z^2 (Z denotes the atomic number). Thus the position of atom columns is imaged with a brightness related to their atomic number, usually referred as Z-contrast. This technique has been employed to characterize LSMO/SRO interfaces [15, 16].

Biaxial epitaxial strain is crucial for magnetic exchange interactions because it systematically alters bond angles and lengths [17]. An example is the comprehensive study by *Seo et al.* [18], which examined three-layer $SrRuO_3$/manganite/$SrRuO_3$ heterostructures. They observed strong compressive strain causes relative ferromagnetic (FM) alignment of magnetization in the heterostructure layers, while tensile or weak compressive strain favors antiferromagnetic (AFM) alignment of neighboring layers. Strain has been shown to reverse the sign of Mn-O-Ru interface coupling in ultrathin $SrRuO_3$/$AMnO_3$/$SrRuO_3$ (A = Ca or Pr) trilayers as observed by X-ray magnetic circular dichroism [18]. That experiment revealed the impact of strain on the magnetic coupling by comparing trilayers grown coherently on $SrTiO_3(001)$ and $LaAlO_3(001)$ substrates. SLs of LSMO/SRO have, so far, not been grown coherently on different substrates and previous work concentrates on SLs grown on TiO_2-terminated $SrTiO_3(001)$. From this point of view, it seems motivating to attempt a new *in-situ* strain control on such SLs using piezoelectric $0.72PbMg_{1/3}Nb_{2/3}O_3$ -$0.28PbTiO_3(001)$ (PMN-PT) substrates [19, 20]. The strain dependence of magnetic order in SRO and LSMO single films has been investigated earlier using *in-situ* strain [21, 22]. Those results for bulk-like films with thicknesses beyond 50 unit cells (20 nm) can help to understand the properties of ultrathin layers in SLs, but must
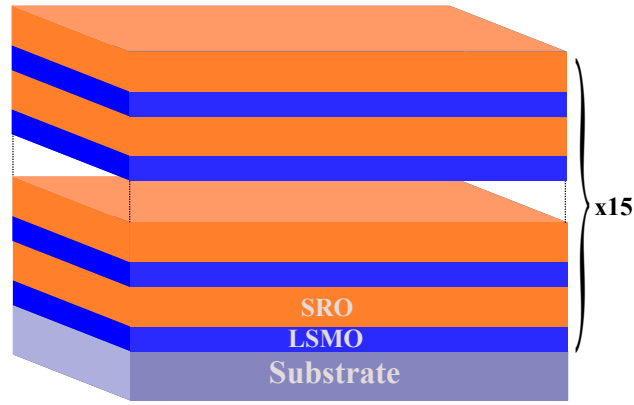
Figure 4.1: Schematic diagram of [LSMO/ SRO]$_{15}$ superlattice samples

be considered with care because interfaces don't matter for the magnetization of bulk-like films. Here the strain dependence of the antiferromagnetic coupling in LSMO/SRO superlattices grown on piezoelectric PMN-PT substrates and a large response to reversible biaxial strain has been investigated. The coupling field strongly increases upon reversible in-plane compression which releases some of the tensile strain in the manganite layers. The observed strain-dependent order of Mn spins at the interface is suggested to contribute to the strain-induced change of the apparent antiferromagnetic coupling.

4.2   Sample preparation

[2.2nm La$_{0.7}$Sr$_{0.3}$MnO$_3$(LSMO)/ 5.5nm SrRuO$_3$(SRO)]$_{15}$ SLs have been grown by Pulsed Laser Deposition (PLD) with a KrF laser (wavelength 248 nm) on (001)-oriented SrTiO$_3$ (STO) and 0.72PbMg$_{1/3}$Nb$_{2/3}$O$_3$-0.28PbTiO$_3$(PMN-PT) substrates using stoichiometric targets of LSMO and SRO. The laser energy density during deposition was 2.5 J/cm^2 at the frequency of 3 Hz. The SLs are grown in 0.1 mbar of pure oxygen at 700 °C substrate temperature. After deposition, *in-situ* annealing is done at 600 mbar O$_2$ at 700 °C for 45 mins. The deposition started with a LSMO layer and ended with a SRO layer. In total, 15 double layers of LSMO and SRO have been deposited [Fig.4.1].

In order to compare the properties many samples have been deposited at different growth parameters and different SRO thickness which shows weaker or even non-existing interfacial coupling. For example, [2.2nm LSMO/4.0nm SRO]$_{15}$ SL is grown by PLD on (001)-oriented PMN-PT substrate in 0.1 mbar of pure oxygen at 650 °C substrate temperature. After deposition, *in-situ* annealing is done at 600 mbar O$_2$ at 650 °C for 45 mins.

4.3   Structural characterization

The SLs have been structurally characterized by X-ray diffraction in a Bruker D8 Discover diffractometer. The microstructure of the SLs has been investigated by high-angle annular
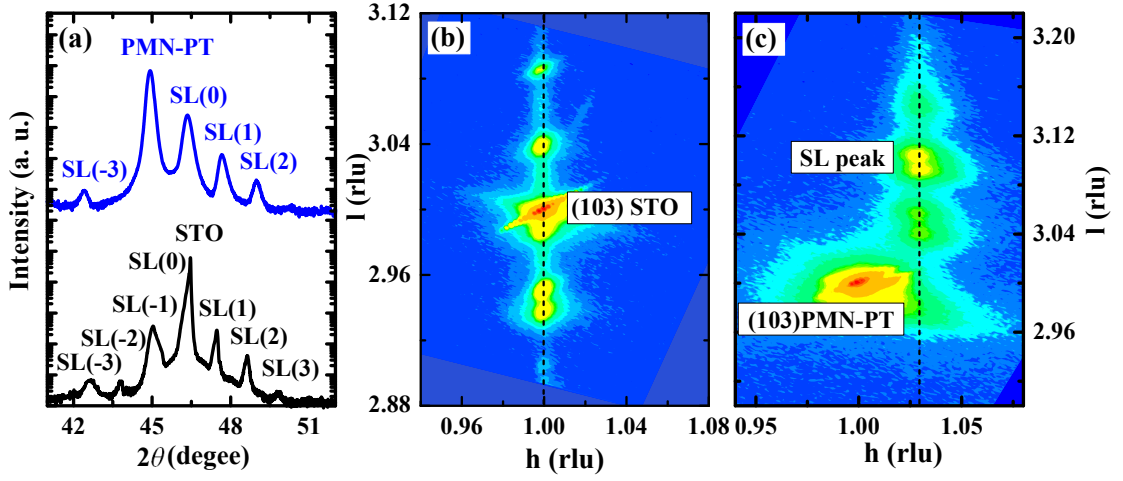
Figure 4.2: (a) $\theta - 2\theta$ X-ray diffraction scans around the (002) reflection of the super-lattices on STO and PMN-PT substrates, respectively. Reciprocal space map around the (103) reflection on (b) STO and (c) PMN-PT.

dark field (HAADF) imaging in a TITAN 80-300 (FEI) scanning transmission electron microscope (STEM). The chemical interdiffusion or intermixing at interfaces was probed by an energy dispersive X-ray spectrometer (EDX) attached to the TITAN and operating in the STEM mode. STEM has been done by Dr. E. Pippel at Max Planck Institute of Microstructure Physics in Halle.

4.3.1 X-ray diffraction

Fig.4.2 (a) shows the $\theta - 2\theta$ XRD scans around the (002) reflection of the [2.2nm LSMO/ 5.5nm SRO]$_{15}$ SL on PMN-PT and STO, respectively. A strong main peak and sharp satellite peaks of the SLs are observed, indicating good structural quality with sharp interfaces. The differences in peak positions are related to the slightly different in-plane strain of SLs on STO and PMN-PT, respectively. In order to determine the average in-plane (a) and the out-of-plane (c) lattice parameters of the superlattices, reciprocal space maps around the pseudocubic (103) reflections were recorded. The derived values of the c lattice parameter of the SL are weighted averages over the components. The estimated c values of SL on STO and PMN-PT are c_{STO}= 3.92 Å and c_{PMN-PT}= 3.90 Å, respectively. According to XRD measurements, SLs grown on STO are strained coherently to the substrate lattice with an in-plane parameter a_{STO} = 3.905 Å. Thus, the LSMO layers in the coherently grown SL are under tensile strain, while the SRO layers experience compressive strain, referring to the bulk lattice parameters of 3.87 Å and 3.93 Å for LSMO and SRO, respectively.

An XRD reciprocal space map of the SL on STO and PMN-PT are shown in Fig.4.2 (b) and (c), respectively. The SL is coherently strained to the STO substrate, but the SL is not coherently strained to the PMN-PT substrate because of the larger in-plane parameter of $a_{PMN-PT} \approx 4.02$ Å (which depends on ferroelectric poling). Strain relaxation occurred immediately at the substrate-SL interface where the first LSMO layer forms
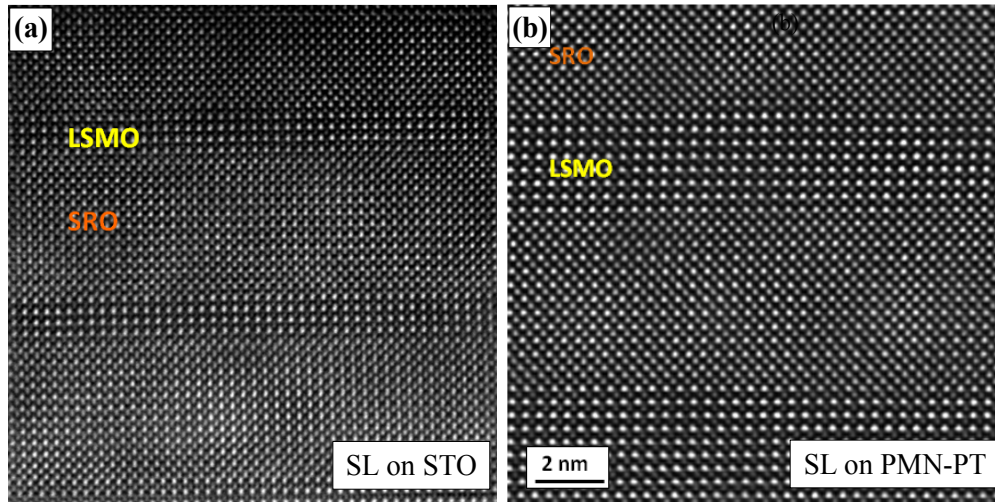
Figure 4.3: HAADF-STEM images of the investigated SL on (a) STO, (b) PMN-PT

misfit dislocations. Nevertheless, the SL itself grew coherently with a lattice parameter of $a = 3.92$ Å. This has been checked by high-resolution STEM (see below). Additionally, *in-situ* recording of the in-plane parameter by tracking the distance of RHEED diffraction streaks during growth has been used to check for strain relaxation during growth. No strain relaxation has been found, confirming to a coherent growth of the SL. To characterize the strain state of the components, we use the in-plane lattice parameter and its deviation from the pseudocubic bulk value. SL grown on PMN-PT, LSMO layers are under slightly stronger tensile strain than in the SL grown on STO, while the SRO layers are under very weak compressive strain. In single layers of LSMO or SRO on STO(001) substrates the film structure is expected to be tetragonal (LSMO) or orthorhombic with small monoclinic distortion (SRO), respectively, but the symmetry of the layers in the SL might be different. For example, it has been shown that ultrathin SRO layers in SLs with PCMO layers are tetragonal [23].

4.3.2   Scanning Transmission Electron Microscopy (STEM)

Several High-resolution STEM images of the SL on STO and PMN-PT confirmed the absence of dislocations and other crystal defects breaking the coherence of the lattice inside the SL [Fig.4.3(a) and (b)]. Probably due to the less well-defined surface of the PMN-PT substrate (and the lattice mismatch of the components), the SRO layers do not grow in fully flat way, but show thickness fluctuations of 2-3 unit cells [Fig.4.3 (b)]. The intermixing at the interfaces of the SL on PMN-PT has been probed by tracking the EDX signal along lines across the interfaces using the Ru-Kα and the Mn-Kα X-ray intensities [Fig.4.4]. From this figure, intermixing of the elements Ru and Mn can be deduced to range over a distance of about 1 unit cell for both interfaces LSMO/SRO and SRO/LSMO. Interestingly, intermixing is very small at the interfaces in spite of the non-ideal flatness of the layers. This indicates the absence of a chemical driving force for intermixing under
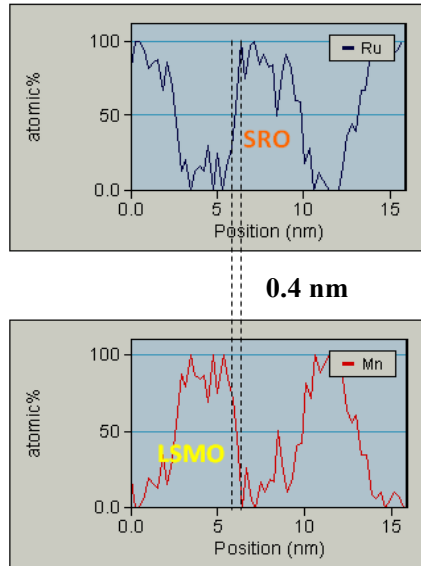
Figure 4.4: EDX line scans of Ru and Mn, crossing LSMO/SRO layers for SL on PMN-PT. The dashed lines indicate an intermixing depth of about 4 Å.

the applied growth conditions. No clear difference between the interfaces of LSMO/SRO and SRO/LSMO (in the sequence of growth) has been found, contrary to the expectation for a well-defined termination of sharp interfaces between layers of complete perovskite unit cells. An inspection by STEM of a SL on $SrTiO_3$ substrate revealed fully coherent growth of flat layers comparable to earlier published work by Ziese *et* al.[7]. A similar magnitude of intermixing at the interfaces has been found for the SL on PMN-PT.

4.4 Magnetization

The magnetization of the SLs has been measured in a SQUID (Superconducting Quantum Interference Device) magnetometer. The magnetizaion is expressed in Bohr magnetons per pseudocubic unit cell.

4.4.1 Temperature and field dependence of magnetization

We first discuss magnetization measurements of a representative [2.2nm LSMO/ 5.5nm SRO]$_{15}$ SL on PMN-PT. Temperature-dependent in-plane (parallel to an [100] direction) magnetization curves recorded during warming in a moderate magnetic field of $\mu_0 H = 0.1$ T, after field-cooling in 2 T, gives evidence for the antiferromagnetic coupling of SRO and LSMO layers. An example is shown in Fig.4.5 (a) where the total magnetization is the difference of the magnetizations of the components below the Curie temperature of SRO. Approaching from high temperatures, LSMO orders first at $T_C^{LSMO} = 263$ K. As temperature drops below $T_C^{SRO} \sim 156$ K, the magnetisation falls. This indicates that the SRO layer has ordered with magnetization opposite to that of the LSMO layer – signifying antiferromagnetic coupling between layers [insets in Fig.4.5 (a)]. The Curie temperature
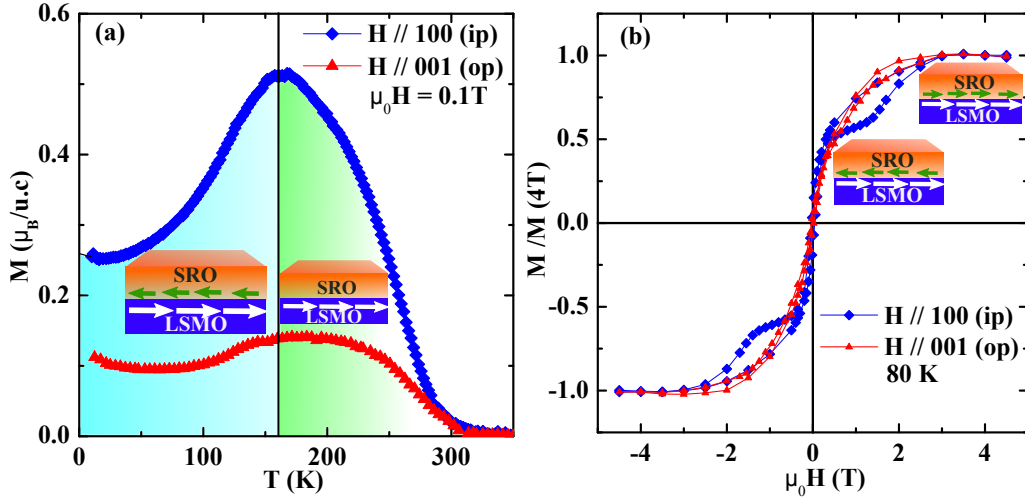
Figure 4.5: Magnetization of the SL on PMN-PT after field cooling (FC) at 2 T in-plane (ip) and out-of-plane (op). (a) Temperature dependence of magnetization at $\mu_0 H = 0.1$ T, (b) magnetization loops at 80K. Insets: schemes of magnetization orientation of LSMO and SRO.

of the components, $T_C{}^{SRO} = 156$ K and $T_C{}^{LSMO} = 263$ K, are close to the bulk value for SRO and strongly reduced (because of the tensile strain of $\sim 1.3\%$ [21] and the low layer thickness) for the LSMO layers. Magnetic hysteresis curves $M(H)$ have been measured at temperatures between 10 K and 100 K both, in the film plane along a pseudocubic [100] direction and along the film normal, the [001] direction. For $T = 80$ K (and in the range of $60 - 100$ K), $M(H)$ reveals hard-axis behavior and nearly reversible magnetization rotation for the normal direction [Fig.4.5 (b)]. This result indicates spontaneous in-plane magnetization for both layers. In-plane $M(H)$ loops measured along a [110] diagonal direction show smaller M(4 T) and smaller remanent magnetization, both indicating {100} easy axes. (In stating that, we assume biaxial in-plane symmetry not to be broken.)

In-plane $M(H)$ loops [Fig.4.5 (b)] show a two-step switching process in the field. Firstly, the LSMO layers align along the field, followed by the alignment of the SRO layers at 1.8 T. This switching sequence is not immediately obvious, because strong anti-ferromagnetic interlayer coupling may lead to different switching sequences depending on the magnetic moments of both layers [7]. Zeeman energy in the applied field, magnetic anisotropy energy of the respective layers and interface coupling govern the switching and may lead to different loop shapes / switching sequences [24]. Based on layer thicknesses and ideal magnetization values of 3.7 μ_B/Mn for LSMO and 1.1 μ_B/Ru, one expects the magnetic moment of LSMO layers to be larger than that of SRO layers. This would mean, based on magnetization values, that the first switching step is related to LSMO alignment [Fig.4.5 (b)], whereas the second is the SRO alignment with the applied field. But this argumentation is weakened by the fact that ultrathin strained LSMO layers are not fully ordered and one does not know their magnetization well enough. More confirmation for the switching sequence is found in the strain response as discussed below. We assign the midpoint of the SRO transition (defined as the point where 50% of the SRO magnetization
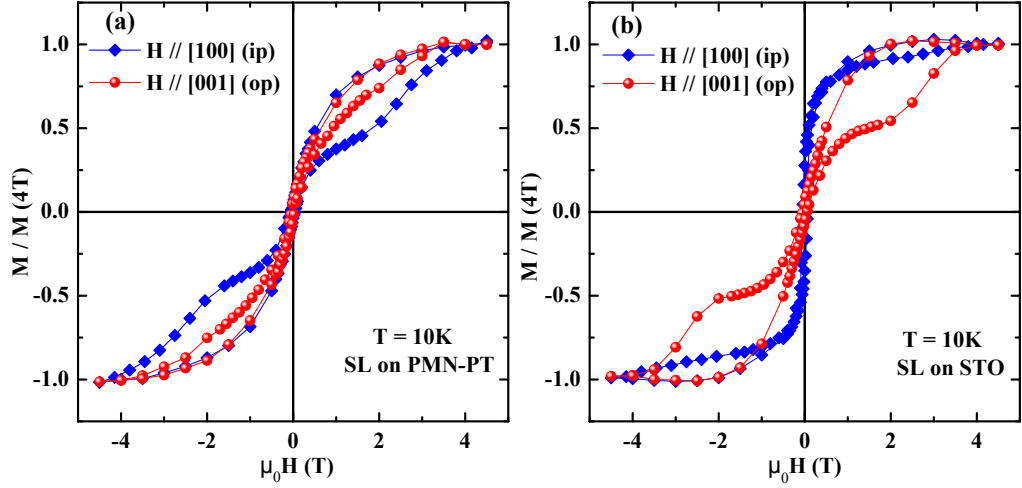
Figure 4.6: Field cooled (FC) at 2 T in-plane (ip) and out-of-plane (op) magnetization loops at $T = 10$K of the superlattices on (a) PMN-PT and (b) STO, respectively.

has been switched) as the coupling field H_{AF}. H_{AF} increases from 1.4 T to 2.8 T when the sample is cooled from 100 K to 10 K. The magnitude and temperature dependence of H_{AF} are qualitatively similar to earlier work on SLs on $SrTiO_3(001)$ substrates,[8, 9] but seem to be sensitive to the quality of the interfaces. H_{AF} is proportional to the inverse SRO thickness, [25] and decreases with increased level of interface roughness / interdiffusion. There is no information on the impact of biaxial in-plane strain on the coupling strength available thus far. The observed strong AFM coupling in the SL on PMN-PT indicates good structural interface quality in agreement with the chemically sharp interfaces found by STEM. The fluctuations in SRO layer thickness surely have the effect of broadening the switching transition.

At 10 K where the anisotropy of SRO is very large, the out-of-plane magnetization of the SL on PMN-PT is more hysteretic and reveals some remanent magnetization [Fig.4.6 (a)]. This indicates that some SRO spins are canted out-of-plane at 10 K. A canted or vertical easy axis may be present in an inner section of the SRO layers [12] at low temperatures. Therefore, strain-dependent measurements have been restricted to $T \geq 60$ K where M essentially lies in the film plane.

The magnetic behavior of the reference SL sample grown on STO substrate is useful to compare because of its smaller in-plane lattice parameter. The Curie temperatures of the components are $T_C^{SRO} = 143$ K and $T_C^{LSMO} = 305$ K. T_C^{SRO} is not so far from the SRO bulk value, but smaller than that of the SL on PMN-PT, in qualitative agreement with the increase of T_C^{SRO} between $a = 3.905$ Å and 3.92 Å [22]. T_C^{LSMO} is about 40 K higher on STO, an expectable shift for the 0.4% weaker tensile strain of the LSMO layers [21]. The magnetic anisotropy of the SLs is also quite different on STO and PMN-PT (Fig.4.6): the in-plane and out-of-plane $M(H)$ loops for both cases appear nearly like interchanged at 10 K. Weak hysteresis and rotation of magnetization in the field occurs for the in-plane $[100_{pc}]$ direction on STO, whereas the out-of-plane M shows a distinct transition at an antiferromagnetic coupling field of $\mu_0 H_{AF} = 2.8$ T. Hence, both layers of LSMO and SRO

in the SL on STO have a spontaneous perpendicular (or canted) magnetization which is antiferromagnetically coupled. This coupling is of similar strength like the in-plane coupling for the SL on PMN-PT. This change of the magnetic anisotropy is consistent with the known influence of epitaxial strain on the anisotropy in single SRO layers [22], whereas compressed films on STO (001) substrate show tilted perpendicular anisotropy [26].

4.4.2   Strain dependence of magnetization

For inspecting the effect of biaxial strain, the piezoelectric PMN-PT substrates are used [20, 21]. An electrical voltage is applied along the substrate normal between the top of the SL serving as top electrode and a NiCr/Au back electrode of the substrate [schematic diagram in Fig.4.7 (a)]. The piezoelectric strain of the substrate is transferred to the SL layers in spite of the large total thickness [10, 19]. The magnitude of the substrate strain has been measured using x-ray diffraction at room temperature [19], and the temperature dependence has been reported in Ref.20. The PMN-PT substrate shrinks approximately linearly with increasing substrate voltage along both [100] and [010] in-plane directions, undergoing a compression of about 0.07% in an electric field of E=10kV/cm at 80K [19, 20]. Fig.4.7 (b) gives a comparison of the $M(H, T = 80$ K$)$ loops in the as-grown and a biaxially compressed ($\triangle\varepsilon \sim$ -0.07%) state for [2.2nm LSMO/ 5.5nm SRO]$_{15}$ SL. The change between the two loops is reversibly controlled by the piezoelectric substrate strain. Similar loops have been measured between 60 K and 100 K. The immediately obvious impact of the compression is an enlargement of the saturated magnetization (at $\mu_0 H = 4$ T) which roughly agrees with the enlargement seen after the first switching step (at $\mu_0 H = 1$ T) [Fig.4.7 (b)]. Here we note that other samples prepared under less favourable growth conditions did not show strong (or even any) coupling. One example shown in Fig.4.7 (c), where the [2.2nm LSMO/4.0nm SRO]$_{15}$ SL is grown on (100)-oriented PMN-PT substrate in 0.1 mbar of pure oxygen at 650 °C substrate temperature shows weak AFM coupling at the interface. Also piezoelectric compression does not influence the AFM coupling of this SL. So, deposition parameters as well as SRO thickness are vital to obtain strongly coupled samples on PMN-PT.

We note that the strain-induced shift of the transition field is only visible in the expanded view in Fig.4.8 discussed later. Ferromagnetic order in LSMO is known to be very sensitive to tensile strain, reflected in strong strain-induced shifts of T_C for thicker LSMO films [21]. Ultrathin LSMO films like those in the present SL sample show some magnetic disorder at the interfaces which substantially reduces the LSMO magnetization. (An ordered moment of 2.6 μ_B/Mn is estimated below.) The latter fact makes the LSMO magnetization strain-dependent through the influence of strain on the ferromagnetic double exchange interaction. The applied reversible compression releases a small part of the as-grown tensile strain of $\sim$1.3% in the LSMO layers. This has a profound effect on LSMO magnetization at $T << T_C{}^{LSMO}$ which increases by 6.3% (at 60 K), 5.5% (80 K)
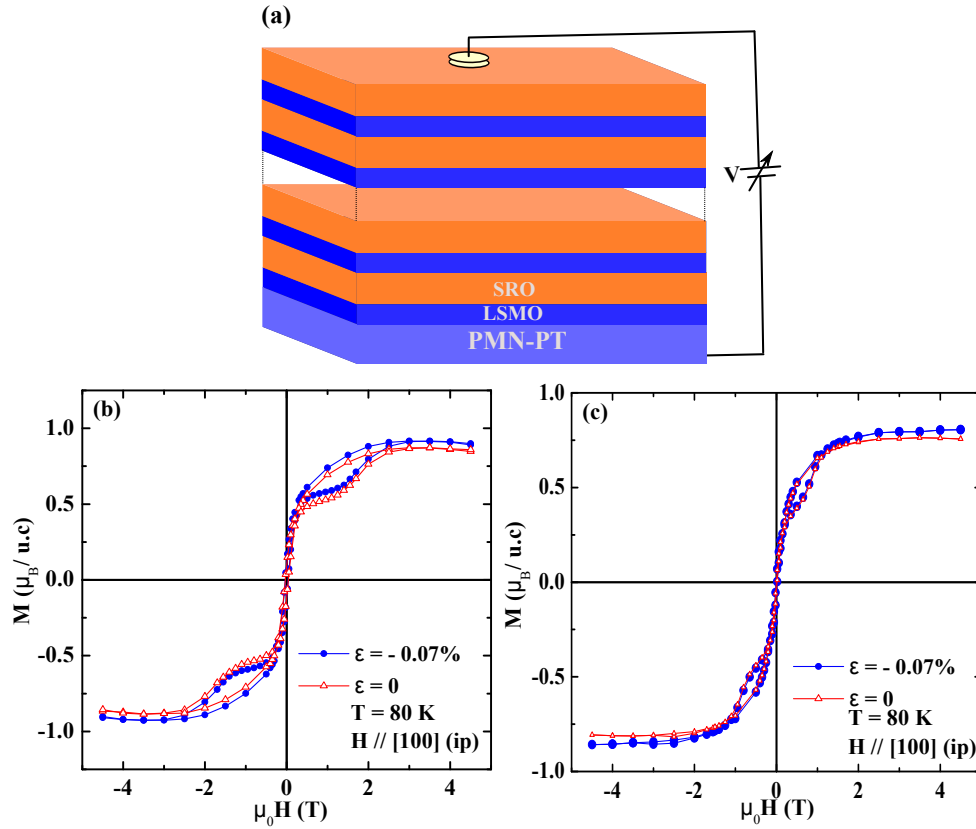
Figure 4.7: (a) Schematic diagram of biaxial strain application, (b) In-plane magnetization loops of the [2.2nm LSMO/ 5.5nm SRO]$_{15}$ SL on PMN-PT in as-grown state (ε = 0) and after piezocompression (ε= - 0.07%), (c) In-plane magnetization loops at T = 80K of the [2.2nm LSMO/4.0nm SRO]$_{15}$ SL deposited at 650 °C substrate temperature on PMN-PT in as-grown state (ε = 0) and after piezocompression (ε= - 0.07%).

or 4.4% (100 K), respectively. These values have been estimated from the strain-induced magnetization increase observed around 1 T [where SRO is anti-aligned to LSMO, see Fig.4.5 (b)] and 4 T (where SRO is aligned parallel to LSMO). As expected for a strain effect on LSMO only, the magnetization increase is the same in both cases. This reveals a general crucial point in assessing the *interlayer* exchange coupling as an independent parameter of interest because the *intralayer* magnetic order matters for the observable coupling strength. Stronger apparent AFM coupling of the SRO layer at the interface as detected by strain-dependent magnetization measurements may result from both, (i) stronger Mn-O-Ru exchange interaction and (ii) higher ordered Mn moment at the interface. (We note that the extreme case of randomly oriented Mn moments would offer no net coupling to ferromagnetically aligned Ru moments.) The issue is further discussed below.

Strain-induced changes of H_{AF} have been determined as the difference of H_{AF} values in two investigated strain states. Care has been taken to check the reversibility of the strain-induced change and the reproducibility of the values in several samples and at several temperatures. The two strain states have been measured in immediate sequence, and curves have not been smoothed. Fig.4.8 provides a direct view on the change of H_{AF}
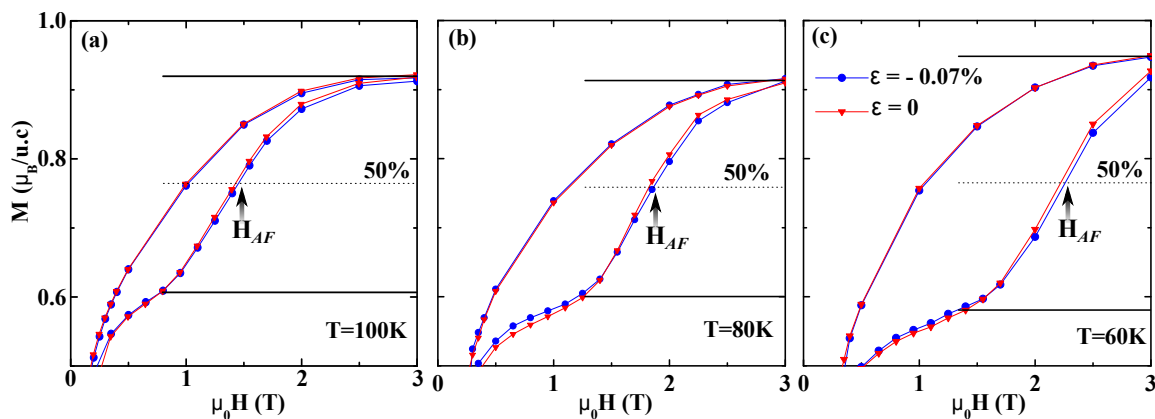
Figure 4.8: Change of the antiferromagnetic coupling field (H_{AF}) induced by the piezo-compression at (a) $T = 100K$, (b) $T = 80K$ and (c) $T = 60K$ of the [2.2nm LSMO/ 5.5nm SRO]$_{15}$ SL. We define H_{AF} as the field where 50% of the SRO magnetization has been switched.

induced by the piezo-compression in the following way: the $\varepsilon = 0$ (as-grown state) loop has been shifted vertically by a constant value to match the loop measured under strain at saturation (4 T). In this way, the strain-enhanced LSMO magnetization is compensated. One notes the shift of H_{AF} at the 50% level of the transition. The values are $\mu_0 \triangle H_{AF}/\triangle \varepsilon =$ -650 mT %$^{-1}$, -520 mT %$^{-1}$, and -410 mT %$^{-1}$ (with an error of $\sim$20%) at the temperatures of 60 K, 80 K, and 100 K. (Lower temperatures have not been investigated because the spontaneous magnetization shows some reorientation out of the film plane as discussed above.) Further, there is a lower slope dM/dH of LSMO around 1 T in the strained case. The latter results from better ferromagnetic order of the LSMO layers after partial release of tensile strain.

4.5   Discussion

Regarding the origin of strain-dependent antiferromagnetic coupling, we consider previously reported models. First principles calculations by Lee *et al.*[27] reveal the lowest total energy for the antiferromagnetic coupling of LSMO and SRO layers for an in-plane lattice parameter close to the one we get on PMN-PT substrates. Similarly, the antiferromagnetic state has been found in density functional theory calculations in Ref. [7]. The influence of in-plane strain has not been investigated yet in such calculations, to our knowledge. On the other hand, discussion on interface magnetic coupling in oxides has been based on orbital hybridization and strain-dependent orbital occupation in recent work [18, 28, 29]. For our lattice parameter of 3.92 Å (strong tensile strain of LSMO), Mn e_g orbital levels are split leading to strong in-plane x^2-y^2 orbital occupation in Mn^{3+} ions. This reduces coupling via the e_g orbitals. The piezo-compression releases a small part of tensile strain and enhances the probability of electrons to occupy out-of-plane orbitals (4d t_{2g} xz and yz minority orbitals for Ru, 3d e_g $3z^2$-r^2 for Mn). Hence, one would expect stronger hybridization and magnetic coupling under piezo-compression, in line with the

observed sign of the strain effect on antiferromagnetic coupling. The details in an orbital picture seem to be less clear if one uses previously suggested arguments. Seo *et al.*[18] have discussed a strain-dependent orbital occupation of Ru^{4+} ions at interfaces of SRO with various manganites, and found a stronger antiferromagnetic coupling for the larger in-plane parameter. This agrees with their experimental results (for different manganites than LSMO), but conflicts with our observation. In a step beyond the consideration in Ref. [18], the contributions of e_g orbitals have been considered. In $SrRuO_3$, the Ru^{4+} e_g orbitals are empty because of the large crystal field splitting. In Mn^{4+}, they are empty, whereas in Mn^{3+} there is one $e_g^{\uparrow}$ electron. Nominally, LSMO contains 30% of Mn^{4+} and 70% Mn^{3+} ions. Coupling via the e_g $3z^2$-r^2 orbitals of Mn and Ru would thus be antiferromagnetic for Mn^{4+} and ferromagnetic for Mn^{3+} at the interface according to the Goodenough-Kanamori rules. The e_g $3z^2$-r^2 orbital occupation of Mn^{3+} is expected to increase with in-plane compression, because the single e_g electron gets a higher probability to leave the tensile-strain-stabilized x^2-y^2 orbital. Again, this e_g-orbital-related mechanism reduces the total antiferromagnetic coupling upon in-plane compression and thus disagrees with our result. Possibly, these single-orbital considerations cannot describe the unusually strong antiferromagnetic coupling at the LSMO/SRO interface if it is based on itinerant electrons.

One other influence should be considered, that is a non-ideal interface structure. Interdiffusion of about one unit cell can strongly affect the experimentally observable coupling. Recently, it is shown that Mn ions of lower oxidation state can even reside on the A site of the ABO_3 perovskite lattice in case of a strong Mn excess [30]. If such a situation would occur at the LSMO/SRO interface, additional magnetic coupling pathways would be present. Such a mechanism for the non-ideal interfaces may also influence experimental results and calls for further improvement of knowledge on real interface structures.

One outcome of this work is finding that it is difficult to characterize the Mn-O-Ru interface coupling based on magnetization measurements if the Mn-O-Mn coupling at the interface is changing simultaneously. This is clearly true for our experiment, as is seen in the enhanced saturated magnetization of the LSMO layers upon piezo-compression. Investigating interface coupling through magnetization measurements means to take into account the intralayer magnetic order in both components as well as the exchange coupling at the interface. Manganite layers are known to show some degree of magnetic disorder at interfaces. In our experiment, this is evident from the lower saturated moment of LSMO as follows. For the as-grown state, the magnetic moment of $\sim$0.6 μ_B per unit cell of the superlattice at 1 T is assumed to represent LSMO layers aligned and SRO layers anti-aligned with the field (Fig.4.7). The reversal of SRO layers yields a change by $\sim$0.3 μ_B / u.c., leading to an estimated ordered moment of 2.6 μ_B / Mn, in contrast to 3.7 μ_B / Mn for fully ordered Mn spins. Release of tensile strain is known to enhance the ferromagnetic Mn-O-Mn double exchange interaction in LSMO, in line with the observed larger LSMO magnetization upon in-plane compression. Hence, we expect the increased

antiferromagnetic coupling of SRO layers to result partially from better ordered Mn spins at the interfaces.

4.6   Conclusion

Summarizing, coherent SLs of [2.2nm LSMO/5.5nm SRO]$_{15}$ on piezoelectric PMN-PT substrates show strong antiferromagnetic interface coupling between the two ferromagnetic components with a profound dependence on reversible strain. The coupling field of $\mu_0 H_{AF} = 2.8$ T is found to change by $\mu_0 \triangle H_{AF}/\triangle \varepsilon \sim$ -520 mT %$^{-1}$ under reversible biaxial strain ($\triangle \varepsilon$) at 80 K in a [2.2nm LSMO/5.5nm SRO]$_{15}$ SL. This reveals a significant strain effect on interfacial coupling. Simultaneously, the magnetic order of the LSMO layers is enhanced strongly under the reversible in-plane compression which releases a part of the as-grown tensile strain. We see the latter effect as an important second influence on H_{AF} besides the strength of the Mn-O-Ru exchange interaction.

Bibliography

[1] J. Nogués and I.K. Schuller, "Exchange bias," J.Magn. Magn. Mater. **192**, 203 (1999).

[2] Z.Q. Qiu, J. Pearson, and S.D. Bader, "Oscillatory interlayer magnetic coupling of wedged Co/Cu/Co sandwiches grown on Cu(100) by molecular beam epitataxy," Phys. Rev. B **46**, 8659 (1992).

[3] P. Bruno and C. Chappert, "Oscillatory coupling between ferromagnetic layers separated by a nonmagnetic metal spacer," Phys. Rev. Lett. **67**, 1602 (1991).

[4] H.L. Störmer, R. Dingle, A.C. Gossard, W. Wiegmann and M.D. Sturge, "Two-dimensional electron gas at a semiconductor-semiconductor interface," Solid State Comm. **29**, 705 (1979).

[5] A. Ohtomo and H. Y. Hwang, "A high-mobility electron gas at the $LaAlO_3/SrTiO_3$ heterointerface," Nature **427**, 423 (2004).

[6] A. Brinkman, M. Huijben, M. van Zalk, J. Huijben, U. Zeitler, J. C. Maan, W. G. van der Wiel, G. Rijnders, D. H. A. Blank & H. Hilgenkamp, "Magnetic effects at the interface between non-magnetic oxides," Nature Materials **6**, 493 (2007).

[7] M. Ziese, I. Vrejoiu, E. Pippel, P. Esquinazi, D. Hesse, C. Etz, J. Henk, A. Ernst, I.V. Maznichenko, W. Hergert, and I. Mertig, "Tailoring Magnetic Interlayer Coupling in $La_{0.7}Sr_{0.3}MnO_3/SrRuO_3$ Superlattices," Phys. Rev. Lett. **104**, 167203 (2010).

[8] M. Ziese, I. Vrejoiu, and D. Hesse, "Inverted hysteresis and giant exchange bias in $La_{0.7}Sr_{0.3}MnO_3/SrRuO_3$ superlattices," Appl. Phys. Lett.**97**, 052504 (2010).

[9] M. Ziese , E. Pippel , E. Nikulina , M. Arredondo and I. Vrejoiu, "Exchange coupling and exchange bias in $La_{0.7}Sr_{0.3}MnO_3$-$SrRuO_3$ superlattices," Nanotechnology **22**, 254025 (2011).

[10] M.C. Dekker, A. Herklotz, L. Schultz, M. Reibold, K. Vogel, M.D. Biegalski, H.M. Christen, and K. Dörr, "Magnetoelastic response of $La_{0.7}Sr_{0.3}MnO_3/SrTiO_3$ superlattices to reversible strain," Phys. Rev. B **84**, 054463 (2011).

[11] M. Ziese, F. Bern, E. Pippel, D. Hesse, and I. Vrejoiu, "Stabilization of Ferro-magnetic Order in $La_{0.7}Sr_{0.3}MnO_3$-$SrRuO_3$ Superlattices," Nano Letters **12**, 4276 (2012).

[12] J.-H. Kim, I. Vrejoiu, Y. Khaydukov, T. Keller, J. Stahn, A. Ruhm, D. K. Satap-athy, V. Hinkov and B. Keimer, "Competing interactions at the interface between ferromagnetic oxides revealed by spin-polarized neutron reflectometry," Phys. Rev. B **86**, 180402(R) (2012).

[13] X. Ke, L. J. Belenky, V. Lauter, H. Ambaye, C. W. Bark, C. B. Eom and M. S. Rzchowski, "Spin Structure in an Interfacially Coupled Epitaxial Ferromagnetic Oxide Heterostructure," Phys. Rev. Lett. **110**, 237201 (2013).

[14] G.J.H.M. Rijnders, G. Koster, D.H.A. Blank, and H. Rogalla, "*In situ* monitoring during pulsed laser deposition of complex oxides using reflection high energy electron diffraction under high oxygen pressure," Appl. Phys. Lett.**70**, 1888 (1997).

[15] R. Hillebrand, E. Pippel, D. Hesse, I. Vrejoiu, "A study of intermixing in perovskite superlattices by simulation-supported c_s-corrected HAADF-STEM," Phys. Stat. Sol. A **208**, No. 9, 2144 (2011).

[16] A.Y. Borisevich, A.R. Lupini, Jun He, E.A. Eliseev, A.N. Morozovska, G.S. Svech-nikov Pu Yu, Y.H. Chu, R. Ramesh, S.T. Pantelides, S.V. Kalinin, and S.J. Pen-nycook, "Interface dipole between two metallic oxides caused by localized oxygen vacancies," Phys. Rev. B **86**, 140102(R) (2012).

[17] S.J. May, J.-W. Kim, J.M. Rondinelli, E. Karapetrova, N.A. Spaldin, A. Bhat-tacharya, and P.J. Ryan, "Quantifying octahedral rotations in strained perovskite oxide films," Phys. Rev. B **82**, 014110 (2010).

[18] J.W. Seo, W. Prellier, P. Padhan, P. Boullay, J.-Y. Kim, Hangil Lee, C.D. Batista, I. Martin, Elbert E.M. Chia, T. Wu, B.-G. Cho, and C. Panagopoulos, "Tunable Magnetic Interaction at the Atomic Scale in Oxide Heterostructures," Phys. Rev. Lett. **105**,167206 (2010).

[19] M.D. Biegalski, D.H. Kim, K.Dörr, H.M.Christen, "Applying uniform reversible strain to epitaxial oxide films," Appl. Phys. Lett. **96**,151905 (2010).

[20] A.Herklotz, J.D.Plumhof, A.Rastelli, O.G.Schmidt, L.Schultz, and K.Dörr, "Elec-trical characterization of PMN–28%PT (001) crystals used as thin-film substrates," J. Appl. Phys., **108**, 094101 (2010).

[21] C. Thiele, K. Dörr, O.Bilani, J.Rödel, and L. Schultz, "Influence of strain on the magnetization and magnetoelectric effect in $La_{0.7}A_{0.3}MnO_3$ /PMN-PT (001) (A=Sr,Ca)," Phys. Rev. B **75**, 054408 (2007).

[22] A. Herklotz, M. Kataja, K. Nenkov, M. D. Biegalski, H.-M. Christen, C. Deneke, L. Schultz, and K. Dörr, "Magnetism of the tensile-strain-induced tetragonal state of $SrRuO_3$ films," Phys. Rev. B **88**, 144412 (2013).

[23] M. Ziese, I. Vrejoiu, E. Pippel, E. Nikulina, and D. Hesse, "Magnetic properties of $Pr_{0.7}Ca_{0.3}MnO_3/SrRuO_3$ superlattices," Appl. Phys. Lett. **98**, 132504 (2011).

[24] A. Solignac, R. Guerrero, P. Gogol, T. Maroutian, F. Ott, L. Largeau, Ph. Lecoeur, and M. Pannetier-Lecoeur, "Dual Antiferromagnetic Coupling at $La_{0.67}Sr_{0.33}MnO_3/SrRuO_3$ Interfaces," Phys. Rev. Lett. **109**, 027201 (2012).

[25] P. Padhan, W. Prellier, and R.C. Budhani, "Antiferromagnetic coupling and enhanced magnetization in all-ferromagnetic superlattices," Appl. Phys. Lett. **88**, 192509 (2006).

[26] M. Ziese, I. Vrejoiu and D. Hesse, "Structural symmetry and magnetocrystalline anisotropy of $SrRuO_3$ films on $SrTiO_3$," Phys. Rev. B **81**, 184418 (2010).

[27] Y. Lee, B. Caes and B.N. Harmon, "Role of Oxygen 2p states for anti-ferromagnetic interfacial coupling and positive exchange bias of ferromagnetic LSMO/SRO bilayers," Journal of Alloys and Compounds **450**,1 (2008).

[28] S. Okamoto, "Magnetic interaction at an interface between manganite and other transition metal oxides," Phys. Rev. B **82**, 024427 (2010).

[29] J. Garcia-Barriocanal, J.C. Cezar, F.Y. Bruno, P. Thakur, N.B. Brookes, C. utfeld, A. Rivera-Calzada, S.R. Giblin, J.W. Taylor, J.A. Duffy, S.B. Dugdale, T. Nakamura, K. Kodama, C. Leon, S. Okamoto and J. Santamaria, "Spin and orbital Ti magnetism at $LaMnO_3/SrTiO_3$ interfaces," Nat. Communs **1**, 82 (2010).

[30] C. Aruta, M. Minola, A. Galdi, R. Ciancio, A.Yu. Petrov, N.B. Brookes, G. Ghiringhelli, L. Maritato and P. Orgiani, "Off-stoichiometry effect on orbital order in A-site manganites probed by x-ray absorption spectroscopy," Phys. Rev. B **86**, 115132 (2012).

Chapter 5

Tuning of antiferromagnetic order at the ferromagnetic $La_{0.7}Ca_{0.3}MnO_3$/ $SrRuO_3$ interface

This chapter addresses the aspect of elastic strain effects on $[La_{0.7}Ca_{0.3}MnO_3/SrRuO_3]_{15}$ superlattices (SLs) which are grown simultaneously on (001)- oriented $SrTiO_3$ (STO), $LaAlO_3$ (LAO) and piezoelectric $0.72Pb(Mg_{1/3}Nb_{2/3})O_3$-$0.28PbTiO_3$(PMN-PT) substrates by pulsed laser deposition. On LAO, the SL assumes a compressive strain state, whereas on PMN-PT it is under tensile strain and on STO an intermediate strain state is achieved. A strong signature of antiferromagnetic (AFM) exchange coupling is observed in all SLs below the Curie temperature of $SrRuO_3$. It is observed that a reversible compression increases the AFM coupling and enhances the SL magnetization.

5.1   Introduction

Coherent interfaces between magnetic oxides such as $La_{0.7}A_{0.3}MnO_3$ (A=Sr,Ca) and $SrRuO_3$ (SRO) may induce an intense magnetic coupling [1, 2]. Recent work has indicated the impact of cooling history, size and elastic strain on the strength and even the sign of the coupling [3, 4, 5, 6, 8]. Lattice strain is also a vital parameter for tuning the electronic states of complex oxide SLs. Elastic strain may change the bond lengths and bond angles which alters the exchange interactions. In addition, the occupation probability of the d orbitals depends on strain [5, 7]. The strain state of the SL can be tuned by choice of substrate and interlayer materials [5, 9]. Influence of direct strain on structural, electronic, and optical properties of the materials can be probed by choosing the piezoelectric substrate of $0.72Pb (Mg_{1/3} Nb_{2/3})O_3$ -$0.28PbTiO_3$ (PMN-PT) [10, 11, 12, 13].

Interfaces are another important source of altered electronic states of complex oxide SLs. Magnetic, electronic and ferroelectric properties of the perovskite oxide superlattices (SL) can be tuned by interface effects such as interdiffusion, charge transfer, magnetic exchange coupling etc [12, 14, 15, 16]. Therefore, magnetic heterostructures and SLs have
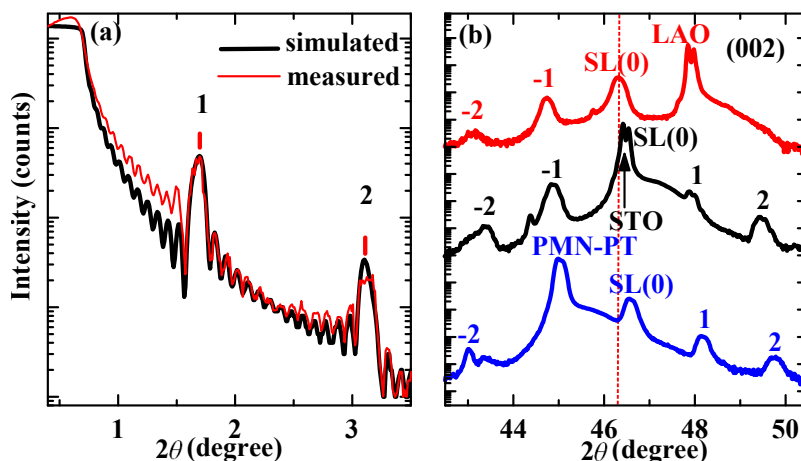
Figure 5.1: (a) X-ray reflectivity measurement of [LCMO/SRO]$_{15}$ SL grown on PMN-PT (thin line) and simulated fitting curve (thick line). (b) $\theta-2\theta$ XRD scans around the (002) reflection of SL grown on LAO (red curve), SL grown on STO (black curve) and SL on PMN-PT (blue curve). The curves are vertically shifted for clarity.

high potential for technological applications like magnetic tunnel junction [17], spin caloric device as well as for fundamental research [18, 19, 20, 21]. Complex oxide SLs bear more promising electronic properties and functionalities than the respective bulk materials. One of the interesting phenomena so called exchange bias effect (shift in the hysteresis loop parallel to the field axis), is most commonly observed at ferromagnet/antiferromagnet interfaces [22]. When the antiferromagnetic interaction between the spins at the interfaces dominates, it can shift the hysteresis loop.

5.2 Sample preparation

We have synthesized the [La$_{0.7}$Ca$_{0.3}$MnO$_3$ (LCMO)/SrRuO$_3$ (SRO)]$_{15}$ SLs composed from stoichiometric targets of La$_{0.7}$Ca$_{0.3}$MnO$_3$ and SrRuO$_3$ on (001)-oriented LaAlO$_3$(LAO) (lattice constant a_{LAO}=3.79 Å), SrTiO$_3$(STO) (a_{STO}=3.905 Å) and piezoelectric 0.72Pb (Mg$_{1/3}$ Nb$_{2/3}$)O$_3$ -0.28PbTiO$_3$(PMN-PT)(a_{PMN-PT}=4.02 Å) substrates simultaneously by off-axis pulsed laser deposition (KrF 248nm). During deposition, temperature is kept constant at 650 °C and the oxygen pressure is at 0.1 mbar. The laser energy density is approximately 2.5 J/cm^2 with repetition rate of 3 Hz. The SLs are annealed for 45 min under 700 mbar O$_2$ pressure after the deposition and then are furnace-cooled to room temperature in the same oxygen environment. The SLs contain 15 layers of LCMO and 15 layers of SRO, deposited alternatively starting with an LCMO layer.

5.3 X-ray diffraction (XRD)

Characterization of the structure and the epitaxial nature of these SLs has been carried out using a Bruker D8 Discover diffractometer with Cu $K\alpha$ radiation. The X-ray reflectivity data exhibits SL peaks (marked as 1, 2) in Fig.5.1 (a) with large number of Kiessig
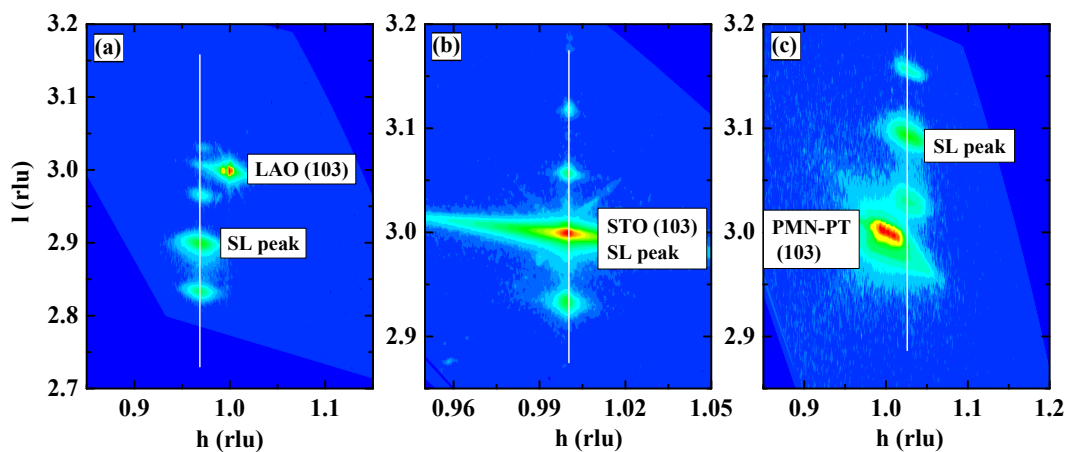
Figure 5.2: Reciprocal space map of LCMO/SRO SLs around the (103) reflection on (a) LAO (b) STO and (c) PMN-PT.

oscillations. These give evidence for smooth layers with well defined interfaces between LCMO and SRO. The value of total thickness (d) of the SLs and the individual thickness of LCMO and SRO layers calculated from X-ray reflectivity simulation [Fig.5.1 (a)] are shown in Table 5.1. In Fig.5.1 (b), all SLs show (002) reflections in the Bragg-Brentano θ-2θ x-ray scans. Besides the (002) peak from the substrate, the presence of a SL main peak [SL(0)] and satellite peaks (marked as 1, 2...−1, −2 etc.) reveal the periodic structure as well as sharp interfaces. One important feature of Fig.5.1 (b) is the shift of SL(0) peak position which is attributed to a change of the average out-of-plane lattice parameter, indicating different elastic strain of the SLs. The SL periods (Λ) calculated from the satellite peak positions are listed in Table 5.1 for different substrates (Λ agrees nearly with d_1+d_2 as expected). An evalution of in-plane (a) and out-of-plane (c) lattice parameter is obtained from XRD reciprocal space maps (RSM) around the (103) reflection (Fig.5.2). The SL is coherently strained to the STO substrate [Fig.5.2 (b)], but the SLs are not coherently strained to the LAO and PMN-PT substrate [Fig.5.2 (a) and (c)], respectively, because of the larger lattice mismatch. Nevertheless, all the SL grew coherently inside the SLs. Calculated lattice parameters are shown in Table 5.1. From these measurements, it is confirmed that on LAO, the SL assumes a compressive strain state, i.e. $c/a>1$, whereas on PMN-PT it shows a tensile strain state ($c/a<1$) and on STO it shows weakly compressive strain. The c lattice parameters calculated this way, are in good agreement with those derived from SL(0) peak position in Fig.5.1 (b). The in-plane lattice parameter of the SL/PMN-PT (3.91 Å) is slightly larger than that of the SL/LAO (3.90 Å) and SL/STO (3.905 Å). Hence, with respect to the bulk in-plane lattice parameter (3.84 Å), LCMO layers are under slightly stronger tensile strain in the SL/PMN-PT than in the SL/LAO and SL/STO. SRO (a_{SRO} = 3.93 Å) layers are under weak compressive strain in all SLs. The lattice structure of a single layer LCMO film is expected to be orthorhombic under tensile strain [23], and that of SRO is expected to be orthorhombic (with small monoclinic distortion) under compressive strain [24, 25]. However, it is difficult to make any such conclusion on the lattice symmetry of the SL

68

Table 5.1: Structural properties of the superlattice samples grown on LAO, STO and PMN-PT substrates: film thicknesses of LCMO (d_1) and SRO (d_2), SL period (Λ), average out-of-plane (c), in-plane (a) lattice parameter and magnetic transition T_C of LCMO and SRO.

Substrate	$[d_1/d_2]_{15}$ (nm)	Period (Λ)	a (Å)	c (Å)	c/a	T_C (LCMO) (K)	T_C (SRO) (K)
LAO	$[2.2/3.81]_{15}$	6.0	3.90	3.92	1.005	234	140
STO	$[2.2/3.82]_{15}$	6.0	3.905	3.91	1.001	229	142
PMN-PT	$[2.2/3.80]_{15}$	5.9	3.91	3.89	0.994	187 (193 for ε=0.1%)	150

components from the XRD measurements. For example, it has been shown that thicker SRO films in LSMO/SRO bilayers are orthorhombic [26] but ultrathin SRO layers in $Pr_{0.7}Ca_{0.3}MnO_3$/SRO SL are tetragonal [27].

5.4 Magnetization

The magnetization measurements have been done by using a SQUID (superconducting quantum interference device) magnetometer. The magnetization is expressed in Bohr magnetons per number of pseudocubic unit cells.

5.4.1 Temperature and field dependence of magnetization

Fig.5.3 (a)-(c) show the temperature-dependent magnetic moments in-plane and out-of-plane of SLs on LAO, STO and PMN-PT, respectively. The measurements are done at 0.01 T magnetic field applied parallel and perpendicular to the surface of SLs, after field cooling (FC) at 2 T. We observe [Fig.5.3 (a)-(c)] two clear magnetic transitions at the Curie temperatures of the components. The ferromagnetic (FM) to paramagnetic (PM) transition temperature (T_C of LCMO) of the SLs are shown in Table 5.1. The T_C is reduced compared to the bulk value of LCMO (250 K) due to strain and the finite size effect [28]. The magnetization monotonically increases with decreasing temperature down to the Curie temperature of SRO. T_C values of SRO are shown in Table 5.1. The magnetic moment decreases sharply below the Curie temperature of SRO for all in-plane and out-of-plane magnetization curves of the SLs. This indicates the appearance of antiferromagnetic (AFM) coupling at the adjacent LCMO and SRO layers, i.e. magnetic moments of SRO layers anti-align to the LCMO moments and the applied field. A small moment of out-of-plane direction proves that the magnetic hard axis lies along SL normal.
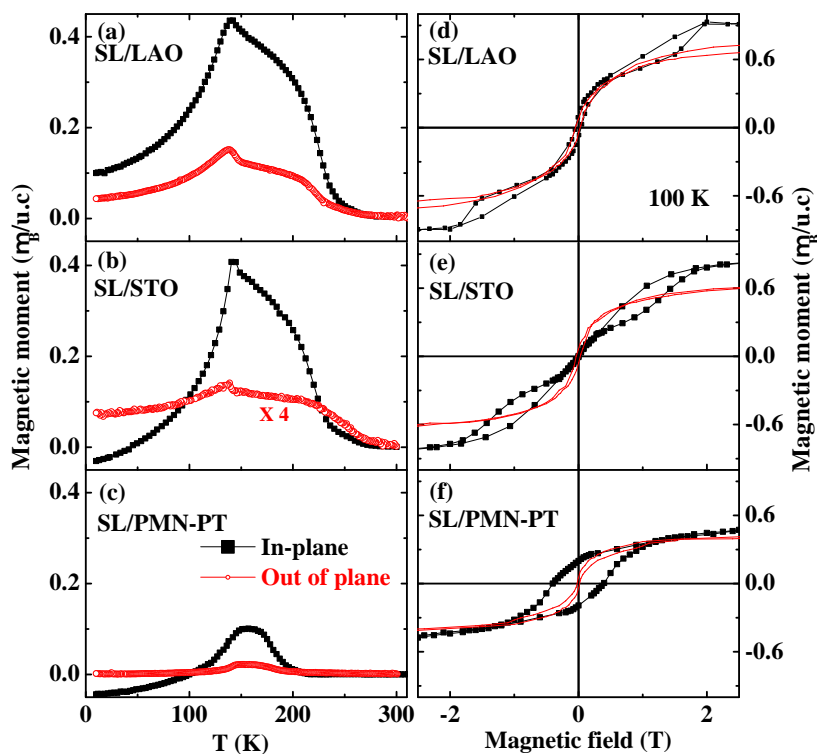
Figure 5.3: Field cooled (FC) in-plane (H // 100) (solid square) and out-of-plane (open circle) magnetic moment as a function of temperature of (a) SL on LAO, (b) SL on STO, and (c) SL on PMN-PT measured in magnetic field of 0.01 T. In-plane (solid square) and out-of-plane (red line) magnetic moment as a function of magnetic field of the SLs (d) on LAO, (e) on STO, and (f) on PMN-PT measured at 100 K.

It is reported that biaxial strain reduces the T_C of manganite layers which depends on the in-plane strain quadratically [2, 10, 29]. Taking the bulk pseudocubic lattice parameter of LCMO (3.84 Å) and SRO (3.93 Å) into account, it is inferred that the LCMO layer is under in-plane tensile strain (ε) of 1.5%, 1.7% and 1.8% for SL on LAO, STO and PMN-PT, respectively, as reflected in the reduced T_C (LCMO). One can stress that, the change of T_C (LCMO) between the SL on STO and PMN-PT is 42 K under the 0.1% strain change (ε_{PMN-PT} -ε_{STO}). But the difference in T_C (LCMO) between LAO and STO samples is very small (5 K) and cannot be explained by 0.1% strain difference (Table 5.1). This is opposite for the T_C (SRO) which are always under compressive strain (-0.8%, -0.6% and -0.5% on LAO, STO and PMN-PT, respectively) (Table 5.1). In this case, change in T_C (SRO) is 1K under -0.1% strain change [2 K under -0.2% strain change (Table 5.1)] between the SL on LAO and STO. While between STO and PMN-PT, the difference is very large 8 K which again cannot be explained by -0.1% strain change and it is contrary to the behavior of T_C (SRO) under strain. Also it is reported that the change in T_C (SRO) under strain is much small [25]. This suggests that the interfaces themselves are playing an important role on different substrates. This motivates to probe the intrinsic interface structure independently of the strain effects. On top of it, strain provides us an easy handle to control the magnetic properties present in our system under observation.
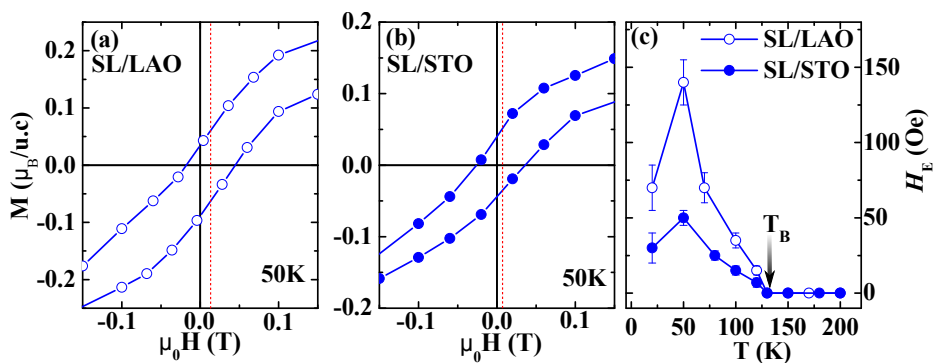
Figure 5.4: Field cooled (FC) curves at 50 K are shown for the SL (a) on LAO and (b) on STO. The horizontal shift is clearly visible and the new centre of gravity of the loop is shown by dotted line. (c) Exchange bias field (H_E) of the SL on LAO (open circle) and the SL on STO (solid circle) as a function of temperature. H_E decreases with increasing temperature and gradually disappears around the blocking temperature $T_B \sim 120$ K

The in-plane and out-of-plane magnetic hysteresis loops recorded at 100 K after field cooling in magnetic field 2 T on LAO, STO and PMN-PT are shown in Fig.5.3 (d), (e) and (f), respectively. The curves are showing astonishing behavior on different substrates. The SL on LAO shows in-plane unconventional double like hysteresis loop while its central part looks like conventional hysteresis. In contrast, the SL on STO the central part of the hysteresis loop is almost absent, i.e. moments of LCMO and SRO nearly compensate. Apart from this unusual behavior, conventional hysteresis loops are observed in the out-of-plane measurements for the SL on LAO and STO. In case of SL on PMN-PT, conventional hysteresis loops are generated while applying magnetic field along out-of-plane and in-plane directions.

The in-plane loop shape can be explained as follows: LCMO layers are comprised of soft spins (more susceptible to magnetic field) while SRO layers are comparatively harder. For the SLs on LAO and STO, at the maximum applied field both magnetizations (LCMO as well as SRO) are aligning along the field direction. At positive low field for SL on LAO, the dominant moments of LCMO still align with the field while SRO moments reverse due to AFM interface coupling (switching field at about ± 0.52 T) to form a ferrimagnetic alignment. For SL on STO, LCMO and SRO moments are compensated between $\sim \pm 0.45$ T and form a ferrimagnetic alignment. The formation of this ferrimagnetic alignment particularly emphasizes a possible strong AFM coupling between LCMO and SRO layers. This ferrimagnetic moments then "follow the field" until a very high magnetic field value where the coupling breaks down and all the moments align along it.

The remnant magnetization along surface normal (out-of-plane) is roughly 8-10% of the saturated moment calculated from the in-plane measurements for all SLs. This points to the fact that Ru and Mn moments are aligned in a canted fashion along a direction slightly tilted from the in-plane field direction. This conclusion is supported by the out-of-plane M-T measurements shown in Fig.5.3.

Zoomed in, central part of the hysteresis loop shows a visible shift towards the positive

field direction after cooling the samples in 2 T. This corresponds to LCMO layer under positive exchange bias [30, 31, 32]. The exchange bias field is defined by the horizontal shift of the centre of the loop. The exchange bias field (H_E) is derived from loops measured at temperatures 20 K, 50 K, 70 K, 80 K, 100 K, 120 K, 130 K and 150 K (Fig.5.4.). If H_{C1} and H_{C2} are the values of positive and negative coercive field, then $H_E = (H_{C1}+H_{C2})/2$.

Fig.5.4 (c) shows the temperature dependence of the exchange bias field H_E of the SL on LAO (open circles) and on STO (solid circles). The H_E for both the SLs, decreases with increasing temperature and goes to zero at the temperature so called blocking temperature around $T_B \sim 120$ K, which is closed to T_C (SRO) [21]. Exchange bias phenomena are quite common at the interfaces of ferromagnetic/antiferromagnetic materials [22]. We observe this phenomenon also at the interfaces of two ferromagnetic layers (LCMO/SRO). The possible explanation of this is: at high positive field, the magnetization of both layers aligns along the field direction. When the field decreases, for the SLs on LAO and STO, below 100 K due to strong magnetic anisotropy, SRO magnetization remains fixed and LCMO magnetization reverses. At temperature above 100 K LCMO moments remain fixed at low field while SRO moments flip i.e. SRO layers pins magnetically soft layers, LCMO. The detailed switching of Mn and Ru moments are further checked by XMCD measurements (details in *Chapter* 6). Both types of SLs here show similar behavior of the exchange field with temperature. The only clear differences are H_E of the SL on LAO is higher than H_E of the SL on STO. It has been shown that the interfacial AFM coupling is responsible for positive exhange bias [22]. Here this is attributed at the interfaces to the larger AFM interfacial exchange interaction in case of SL on LAO than on STO. Moreover, the AFM coupling strength can also be varied by strain while its effects on the behavior of H_E is observed as shown in Fig.5.4 (c). For the SL on PMN-PT, the AFM coupling is very weak at the interfaces which lack any detectable H_E.

5.4.2 Reversible strain-dependent magnetization

In order to study the SL properties under reversible strain, we used the SL on PMN-PT substrate. The magnetic response of the SL is controlled by the in-plane compressive strain from inverse piezoelectric effect of the PMN-PT substrate [11, 13, 10]. The applied electric field across the 0.3 mm thick substrate is slowly ramped up to E=10 kV/cm (schematic diagram of measuring set-up shown in Fig.5.5 (a) inset) which creates a compressive strain ∼0.1% [33]. Upon application of E the magnetization ΔM/M(0) = [M(E) –M(0)] /M(0) [M(E) and M(0) are the magnetization under finite E and zero E, respectively] is ∼11% at an applied electric field 10 kV/cm as shown in Fig.5.5 (a). It is observed that the magnetization grows approximately linear with electric field E in the in-plane direction [H//100] following the compression of the PMN-PT crystal. This proves that the strain can be transferred into the SL, [11] and it modulates the magnetization of the SL. We measure in-plane magnetic hysteresis loops under E=10 kV/cm and E=0 after field cooling at 2 T and 100 K as shown in the Fig.5.5 (b). It is seen that M is enhanced
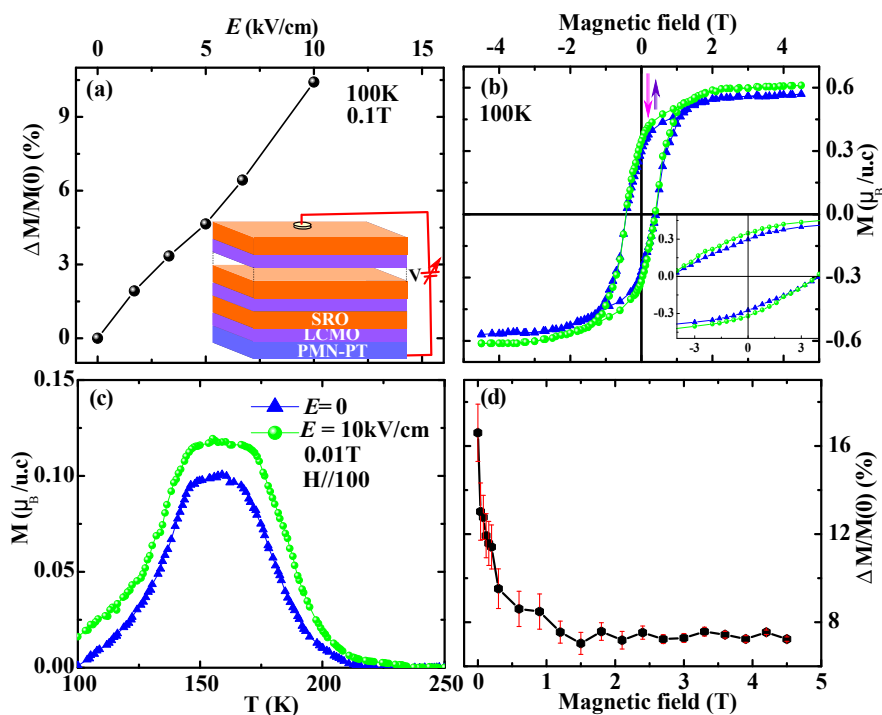
Figure 5.5: (a) The magnetization △M/M(0) of the SL plotted as a function of the *E*-field strength. Inset: Schematic picture of reversible strain application. (b) M-H loops under two strain states at *E*=10 kV/cm and *E*=0, Inset: Zoomed at the central part. (c) Temperature dependence magnetization of the SL on PMN-PT in two strain states; (d) Relative change of the magnetization between the two strain states as defined in the text with magnetic field.

up to 4.5 T after applying the 0.1% piezocompression. The strain also increases the remnant magnetization (M_R), but no detectable change in the H_C is found, indicating that the magneto-crystalline anisotropy does not change due to small in-plane compression. To infer the modulation of AFM coupling and the spin ordered structure between the LCMO and SRO layers at the interfaces under the reversible strain we have shown the M-T at different values of E [Fig.5.5 (c)]. This supports the enhancement of magnetic order under application of 0.1% compressive strain. To explore the correlation between the change of magnetization and electric field directly we turn our attention to the magnetization △M/M(0) between two strain states as a function of magnetic field [Fig.5.5 (d)]. △M/M(0) decreases almost exponentially with magnetic field up to ∼1.8 T. At high magnetic field, μ_0H >1.8 T, △M/M(0) saturates to a value of about 7% which reveals that the influence of strain on magnetic ordering is still present at high field where most of Mn and Ru spins align along the magnetic field. This indicates that magnetic order, probably of the Mn spins is not complete (see *Chapter* 4).

5.5   Conclusion

In summary, we report the evidence of interfacial AFM coupling in LCMO/SRO SLs. SLs in different static strain states have been obtained on three types of oxide substrates. The

ordered magnetic moment and the Curie temperature of LCMO and SRO are signicantly different among the samples. The effect of the elastic strain has been separately evaluated by the approach of reversible strain application using a piezoelectric PMN-PT substrate. The influence of strain is found to be strong, but it cannot alone account for the change of T_C and the ordered magnetic moment in comparion to the SL/LAO, SL/STO and SL/PMN-PT, suggesting that the interfacial roughness and structural dislocations playing a role at the interfaces.

Bibliography

[1] M. Ziese, I. Vrejoiu, E. Pippel, P. Esquinazi, D. Hesse, C. Etz, J. Henk, A. Ernst, I.V. Maznichenko, W. Hergert, and I. Mertig, "Tailoring Magnetic Interlayer Coupling in $La_{0.7}Sr_{0.3}MnO_3$/$SrRuO_3$ Superlattices," Phys. Rev. Lett. **104**, 167203 (2010).

[2] G. Q. Gong, A. Gupta, Gang Xiao, P. Lecoeur, and T. R. McGuire, "Perovskite oxide superlattices: Magnetotransport and magnetic properties," Phys. Rev. B **54**, R3742 (1996).

[3] X. Ke, L. J. Belenky, V. Lauter, H. Ambaye, C. W. Bark, C. B. Eom and M. S. Rzchowski, "Spin Structure in an Interfacially Coupled Epitaxial Ferromagnetic Oxide Heterostructure," Phys. Rev. Lett. **110**, 237201 (2013).

[4] X. Ke, L. J. Belenky, C. B. Eom, and M. S. Rzchowski, "Antiferromagnetic exchange-bias in epitaxial ferromagnetic $La_{0.67}Sr_{0.33}MnO_3$/$SrRuO_3$ bilayers," J. Appl. Phys. **97**, 10K115 (2005).

[5] J.W. Seo, W. Prellier, P. Padhan, P. Boullay, J.-Y. Kim, Hangil Lee, C.D. Batista, I. Martin, Elbert E.M. Chia, T. Wu, B.-G. Cho, and C. Panagopoulos, "Tunable Magnetic Interaction at the Atomic Scale in Oxide Heterostructures," Phys. Rev. Lett. **105**,167206 (2010).

[6] P. Padhan and W. Prellier, "Size effect on magnetic coupling in all-ferromagnetic superlattices," Appl. Phys. Lett. 99, 263108 (2011).

[7] Y. Tokura and N. Nagaosa, "Orbital Physics in Transition-Metal Oxides," Science **288**, 462 (2000).

[8] S. Rao Singamaneni, W. Fan, J. T. Prater, and J. Narayan, "Complete vertical M-H loop shift in $La_{0.7}Sr_{0.3}MnO_3$/$SrRuO_3$ thin film heterostructures," J. Appl. Phys. **117**, 17B711 (2015).

[9] B.C. Behera, P. Padhan , W. Prellier, "Infl uence of substrate in all-ferromagnetic superlattices," J.Magn. Magn. Mater. **388**, 22 (2015).

[10] C. Thiele, K. Dörr, O.Bilani, J.Rödel, and L. Schultz, "Influence of strain on the magnetization and magnetoelectric effect in $La_{0.7}A_{0.3}MnO_3$ /PMN-PT (001) (A=Sr,Ca)," Phys. Rev. B **75**, 054408 (2007).

[11] M.D. Biegalski, D.H. Kim, K.Dörr, H.M.Christen, "Applying uniform reversible strain to epitaxial oxide films," Appl. Phys. Lett. **96**,151905 (2010).

[12] Hajo J. A. Molegraaf, Jason Hoffman, Carlos A. F. Vaz, Stefano Gariglio, Dirk van der Marel, Charles H. Ahn, and Jean-Marc Triscone, "Magnetoelectric Effects in Complex Oxides with Competing Ground States," Adv. Mat.**21**, 3470 (2009).

[13] M.C. Dekker, A. Herklotz, L. Schultz, M. Reibold, K. Vogel, M.D. Biegalski, H.M. Christen, and K. Dörr, "Magnetoelastic response of $La_{0.7}Sr_{0.3}MnO_3/SrTiO_3$ super-lattices to reversible strain," Phys. Rev. B **84**, 054463 (2011).

[14] J.-H. Kim, I. Vrejoiu, Y. Khaydukov, T. Keller, J. Stahn, A. Ruhm, D. K. Satapathy, V. Hinkov and B. Keimer, "Competing interactions at the interface between ferromagnetic oxides revealed by spin-polarized neutron reflectometry," Phys. Rev. B **86**, 180402(R) (2012).

[15] A.Y. Borisevich, A.R. Lupini, Jun He, E.A. Eliseev, A.N. Morozovska, G.S. Svechnikov Pu Yu, Y.H. Chu, R. Ramesh, S.T. Pantelides, S.V. Kalinin, and S.J. Pennycook, "Interface dipole between two metallic oxides caused by localized oxygen vacancies," Phys. Rev. B **86**, 140102(R) (2012).

[16] K. Lv, H. P. Zhu, W. Q. Zou, F. M. Zhang, and X. S. Wu, "Charge transfer and orbital reconstruction in the $(La_{2/3}Sr_{1/3}MnO_3)_m/(SrRuO_3)_n$ superlattices," J. Appl. Phys. **117**, 185305 (2015).

[17] K. S. Takahashi, A. Sawa, Y. Ishii, H. Akoh, M. Kawasaki, and Y. Tokura, "Inverse tunnel magnetoresistance in all-perovskite junctions of $La_{0.7}Sr_{0.3}MnO_3/SrTiO_3/SrRuO_3$," Phys. Rev. B **67**, 094413 (2003).

[18] S. Thota, Q. Zhang, F. Guillou, U. Lüders, N. Barrier, W. Prellier, A. Wahl, and P. Padhan, "Anisotropic magnetocaloric effect in all-ferromagnetic $La_{0.7}Sr_{0.3}MnO_3/SrRuO_3$ superlattices," Appl. Phys. Lett. **97**, 112506 (2010).

[19] M. Ziese, "A spin-calorics device based on $La_{0.7}Sr_{0.3}MnO_3/SrRuO_3$ superlattices," Phys. Status Solidi RRL **5**, No. 12, 444 (2011).

[20] Q Zhang, S Thota, F Guillou, P Padhan, V Hardy, A Wahl and W Prellier, "Magnetocaloric effect and improved relative cooling power in $La_{0.7}Sr_{0.3}MnO_3/SrRuO_3$ superlattices," J. Phys.: Condens. Matter **23**, 052201 (2011).

[21] S. N. Jammalamadaka, J. Vanacken, and V. V. Moshchalkov, "Resistive switching in ultra-thin $La_{0.7}Sr_{0.3}MnO_3/SrRuO_3$ superlattices," Appl. Phys. Lett. **105**, 033505 (2014).

[22] J. Nogués and I.K. Schuller, "Exchange bias," J.Magn. Magn. Mater. **192**, 203 (1999).

[23] C. J. Lu, Z. L. Wang, C. Kwon, and Q. X. Jia, "Structural and magnetic properties of ultrathin epitaxial $La_{0.7}Ca_{0.3}MnO_3$ manganite films: Strain versus finite size effects," Appl. Phys. Lett., 83, 4 (2003).

[24] Gertjan Koster, Lior Klein, Wolter Siemons, Guus Rijnders, J. Steven Dodge, Chang-Beom Eom, Dave H. A. Blank, and Malcolm R. Beasley, "Structure, physical properties, and applications of $SrRuO_3$ thin films," Rev. Mod. Phys. **84**, 253 (2012).

[25] A. Herklotz, M. Kataja, K. Nenkov, M. D. Biegalski, H.-M. Christen, C. Deneke, L. Schultz, and K. Dörr, "Magnetism of the tensile-strain-induced tetragonal state of $SrRuO_3$ films," Phys. Rev. B **88**, 144412 (2013).

[26] A. Solignac, R. Guerrero, P. Gogol, T. Maroutian, F. Ott, L. Largeau, Ph. Lecoeur, and M. Pannetier-Lecoeur, "Dual Antiferromagnetic Coupling at $La_{0.67}Sr_{0.33}MnO_3/SrRuO_3$ Interfaces," Phys. Rev. Lett. **109**, 027201 (2012).

[27] M. Ziese, I. Vrejoiu, E. Pippel, E. Nikulina, and D. Hesse, "Magnetic properties of $Pr_{0.7}Ca_{0.3}MnO_3/SrRuO_3$ superlattices," Appl. Phys. Lett. **98**, 132504 (2011).

[28] M. Ziese, H. C. Semmelhack, K. H. Han, S. P. Sena, and H. J. Blythe, "Thickness dependent magnetic and magnetotransport properties of strain- relaxed $La_{0.7}Ca_{0.3}MnO_3$ films," J. Appl. Phys. **99**, 9930 (2002).

[29] C. Adamo, X. Ke, H. Q. Wang, H. L. Xin, T. Heeg, M. E. Hawley, W. Zander, J. Schubert, P. Schiffer, D. A. Muller, L. Maritato and D. G. Schlom, "Effect of biaxial strain on the electrical and magnetic properties of (001) $La_{0.7}Sr_{0.3}MnO_3$ thin films," Appl. Phys. Lett. **95**, 112504 (2009).

[30] X. Ke, M. S. Rzchowski, L. J. Belenky, and C. B. Eom, "Positive exchange bias in ferromagnetic $La_{0.67}Sr_{0.33}MnO_3/SrRuO_3$ bilayers," Appl. Phys. Lett. **84**, 5458 (2004).

[31] S. N. Jammalamadaka, J.Vanacken and V. V. Moshchalkov., "Exchange bias and training effects in antiferromagnetically coupled $La_{0.7}Sr_{0.3}MnO_3/SrRuO_3$ superlattices," Euro Phys. Lett., **98** , 17002 (2012).

[32] M. Ziese, F. Bern, and I. Vrejoiu, "Exchange bias in manganite/$SrRuO_3$ superlattices," J. Appl. Phys. **113**, 063911 (2013).

[33] A.Herklotz, J.D.Plumhof, A.Rastelli, O.G.Schmidt, L.Schultz, and K.Dörr, "Electrical characterization of PMN–28%PT (001) crystals used as thin-film substrates," J. Appl. Phys., **108**, 094101 (2010).

Chapter 6

Termination control of magnetic order at the interface of ferromagnetic oxides $La_{0.7}Sr_{0.3}MnO_3$ and $SrRuO_3$

The control of interfacial terminations of complex oxide films at the atomic level has potential to lead to novel interfacial functionalities. This chapter highlights some of the effects of interface termination on magnetic order at $La_{0.7}Sr_{0.3}MnO_3$-$SrRuO_3$ interfaces by precise control of atomic-scale termination of the materials at the interface. The atomic termination at the interfaces is achieved by altering the stacking sequence of the layers $La_{0.7}Sr_{0.3}MnO_3$ and $SrRuO_3$. The results demonstrate how the intefacial coupling and the switching of Mn and Ru dramatically depend on interface termination.

6.1 Introduction

The interface between two (001)-oriented perovskites ABO_3 and $A'B'O_3$ can have two different interface terminations on an atomic scale (AO-BO_2-$A'O$-$B'O_2$ or BO_2-AO-$B'O_2$-$A'O$). Different interface terminations can crucially alter the interfacial interaction between the layers and the physical properties of the heterostructures [1, 2]. They can have different nominal charge of opposite sign if the atomic planes are not charge neutral. A prominent example is the $LaAlO_3$/$SrTiO_3$ interface containing a quasi-two-dimensional electron gas for the TiO_2-LaO termination, while the interface termination is AlO_2-SrO, it shows insulating behavior. As another example, the $BiFeO_3$/$La_{0.7}Sr_{0.3}MnO_3$ interface shows different ferroelectric polarization switching for the $La_{0.7}Sr_{0.3}O$-MnO_2-BiO-FeO_2 and MnO_2-$La_{0.7}Sr_{0.3}O$-FeO_2-BiO terminations, respectively [3]. Low interdiffusion is indispensable for obtaining well-defined interface terminations. This poses an obstacle to the realization of one or both terminations for many oxide combinations. Chemistry and growth conditions are decisive and have to be explored specifically for any two oxides. For example, a set of bilayers with reversed layer sequence has been investigated for $LaMnO_3$/$LaNiO_3$ by Gibert *el* al. [4] where no termination could be identified due
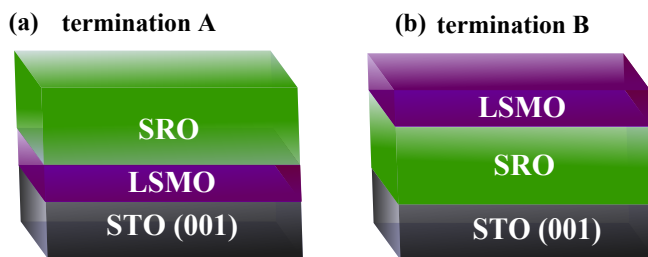
Figure 6.1: Schematic diagram of bilayers, (a) termination A type sample where LSMO is the first layer on top of TiO_2 terminated STO substrate and SRO is on top of LSMO layer, (b) termination B type sample where layer sequence is opposite to termination A type sample.

to interdiffusion at the interface. Rarely, the influence of the terminations has been explicitly studied. Some recent work has concentrated on interfaces with A′= A or B′ = B [5, 6] using the advantage of well-defined interfaces. In all other systems where A′ $\neq$ A and B′ $\neq$B, the interface termination is an open parameter of likely vital impact on electronic properties. Hence, termination control of perovskite oxide interfaces is crucial for understanding and utilizing future oxide electronics.

This chapter reports on the $La_{0.7}Sr_{0.3}MnO_3$-$SrRuO_3$ (LSMO-SRO) interface grown with both terminations by altering the stacking sequence of the layers. Based on Scanning Transmission Electron Microscopy (STEM) analysis, atomically sharp (La,Sr)O-MnO_2/SrO-RuO_2 interface is observed (called termination A hereafter) after growing LSMO and, subsequently, SRO on TiO_2-terminated $SrTiO_3$(001) (STO). The reversed layer sequence (LSMO/SRO/STO(001)) nominally leads to the SrO-$RuO_2/(La,Sr)O$-MnO_2 interface (called termination B). The different terminations have their own conspicuous effects on the magnetic properties of the coherent oxide interfaces is reported. X-ray magnetic circular dichroism (XMCD) measurements reveal an unusually tight magnetic coupling across the interface leading to joined reversal of Mn and Ru moments for the termination A interface. In contrast, the interface termination B shows a more conventional antiferromagnetic interface coupling. Magnetization and XMCD data suggest that $SrRuO_3$ has a tetragonal lattice symmetry at the termination A interface, whereas it keeps the orthorhombic (monoclinic) symmetry of bulk SRO for the other termination.

6.2   Sample preparation

Two types of bilayers (BLs) have been grown with same thickness of the layers. The BL $La_{0.7}Sr_{0.3}MnO_3$(9 u.c)/$SrRuO_3$(14 u.c) (termination A) [Fig.6.1 (a)] and $SrRuO_3$(14 u.c)/$La_{0.7}Sr_{0.3}MnO_3$(9 u.c) (called termination B) [Fig.6.1 (b)] are grown on TiO_2 terminated $SrTiO_3$ (STO) (001) using multitarget pulse laser deposition (PLD). The laser energy density of the deposition was 0.3 J/cm^2 and the frequency 3 Hz. The BLs are grown under 0.2 mbar of oxygen atmosphere at 700 °C substrate temperature. After the deposition, in-situ annealing is done under 200 mbar O_2 pressure at 700 °C for an hour.
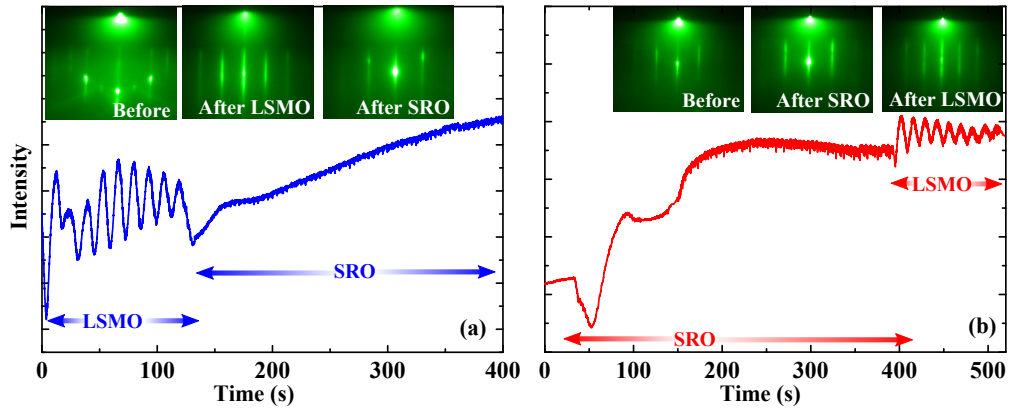
Figure 6.2: RHEED intensity during epitaxial growth for (a) termination A and (b) termination B samples. Strong oscillations during LSMO growth indicate a layer-by-layer growth mode. No oscillations during SRO growth are consistent with step-flow growth mode. Diffraction patterns before and after deposition of LSMO, SRO indicate epitaxial registry.

6.3 Structural Characterization

The BL have been structurally characterized by *in-situ* reflection high-energy electron diffraction and X-ray diffraction in a Bruker D8 Discover diffractometer. The microstructure of the BLs and their atomic termination at the interfaces has been investigated by high-angle annular dark field (HAADF) imaging in a TITAN 80-300 (FEI) scanning transmission electron microscope (STEM). STEM investigations have been done by Dr. E. Pippel at Max Planck Institute of Microstructure Physics in Halle.

6.3.1 Reflection high-energy electron diffraction

The growth mode, thickness and the crystalline quality of the BLs have been observed by *in-situ* high pressure reflection high-energy electron diffraction (RHEED) monitored during the deposition of LSMO and SRO. Fig.6.2 shows sharp RHEED pattern before deposition and after deposition of LSMO and SRO [Fig.6.2 (a) termination A and (b) termination B type sample], which indicates the epitaxial growth of the layers with same structure as substrate. The thickness of LSMO layers is controlled on an atomic scale by monitoring the RHEED intensity oscillations [Fig.6.2 (a) termination A and (b) termination B type sample] which indicates a layer-by-layer growth mode of LSMO. From the RHEED oscillations, the thickness of LSMO is 9 u.c for both bilayers. In case of SRO layer, RHEED oscillations could not be observed because of the step-flow growth mode. The thickness of the SRO of 5.5 nm (14 u.c) is calculated from *ex-situ* X-ray reflectivity.

6.3.2 X-ray diffraction

The XRD reciprocal space maps in the vicinity of (103) reflection [Fig.6.3 (b) and (c)] show the LSMO and SRO epitaxial layers on STO strained coherently to the substrate lattice
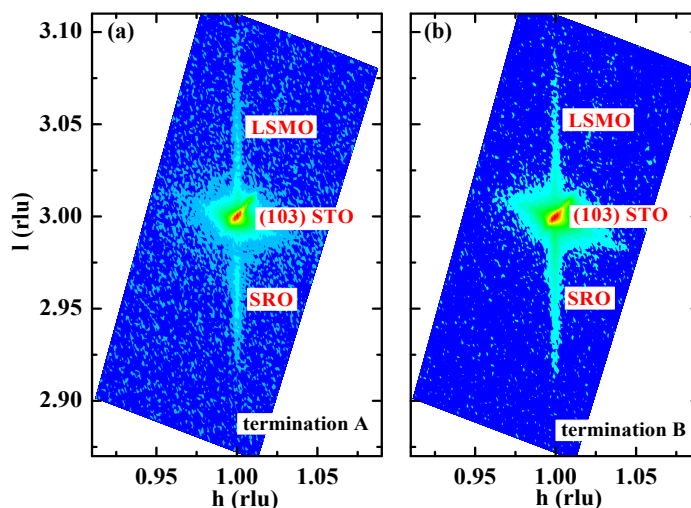
Figure 6.3: Reciprocal space map around the (103) reflection of (a) termination A, and (b) termination B sample.

with an in-plane parameter a_{STO} =3.905 Å. The out-of-plane (c) lattice parameters of LSMO and SRO are 3.828 Å and 3.983 Å for termination A sample and 3.828 Å and 3.980 Å for termination B sample, respectively. Thus, the LSMO layers in the coherently grown BLs are under tensile strain, while the SRO layers experience compressive strain, referring to the bulk lattice parameters of 3.87 and 3.93 Å for LSMO and SRO, respectively. From these in-plane and out-of-plane lattice parameters it is clear that the strain state of LSMO and SRO in termination A sample is equal to that of the termination B sample within the error range of the measurement.

6.3.3   Scanning Transmission Electron Microscopy (STEM)

The microstructure and, in particular, the kind of termination (A, B) at the interfaces have been examined by STEM using High Angle Annular Dark Field (HAADF) contrast. In the HAADF-STEM images, the intensity at an atomic column grows roughly with the value of Z^2 (Z denotes the atomic number). This also holds for the weighted average of Z values when a lattice site is occupied by different atoms. Interdiffusion occurs only within the same sublattice in the present system, i. e. La and Sr stay at the A sites and Mn and Ru at the B sites. The Z values of A site atoms are 38 (Sr) and 51 ($La_{0.7}Sr_{0.3}$), those of B site atoms are 25 (Mn) and 44 (Ru). Hence, the elemental Z contrast for the LSMO-SRO interface is very good and reliable in particular for B sites because of the heavier $4d$ element Ru. Thickness variations of STEM samples additionally change the intensity ratio for any two elements [7]. Bulk intensity values and their errors of Mn, Ru, Sr and $La_{0.7}Sr_{0.3}$ columns have been estimated by averaging intensities at atomic positions away from the interface. Fig.6.4 shows STEM images of the LSMO/SRO interface. For termination A, the intensity profile taken from the STEM image along a line (red line) crossing the interface and all types of atomic columns shows clearly the MnO_2-SrO interface [Fig.6.4 (a)]. Mn and Sr intensities at the interface are in agreement with the bulk intensity values.
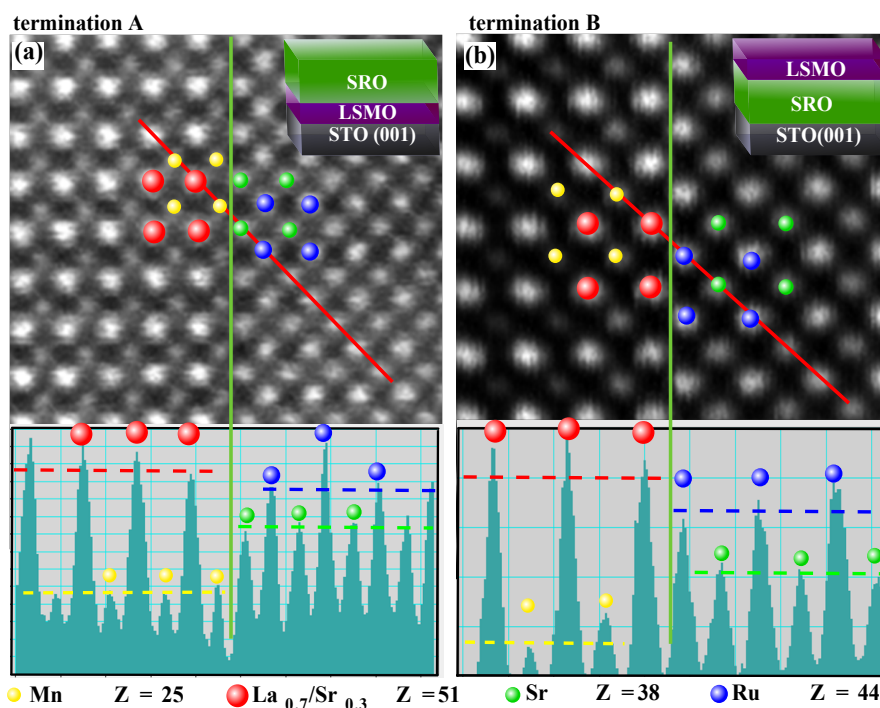
Figure 6.4: Atomic structure of the terminations of the $La_{0.7}Sr_{0.3}MnO_3$-$SrRuO_3$ interface, as obtained by HAADF-STEM (Z-contrast). The images are rotated by $90^{\underline{o}}$ with respect to the related layer systems (upper right insets). The interfaces between LSMO and SRO are marked by green lines. The lower insets show the linear intensity profiles along the red lines crossing the intefaces. (a) MnO_2-SrO termination at the interface of termination A and (b) RuO_2-(La,Sr)O termination at the interface of termination B sample. For details see text.

The result indicates that this interface termination is free of intermixing and chemically stable. For termination B, the RuO_2-(La,Sr)O interface is detectable but with modest interdiffusion [Fig.6.4 (b)]. The Mn peak next to the interface is larger than in the bulk, indicating some Ru admixture, and the Ru site at the interface seems slightly reduced in intensity, both observations indicating some B site interdiffusion. Intermixing at the A sites is not notable. Averaging over 10 parallel lines crossing the interfaces in different places confirm the result shown in Fig.6.4. It is noted that the RuO_2 atomic top layer of the SRO film for termination B is not in agreement with previous expectations, since a SrO surface termination of single SRO films has been reported in an earlier study [8]. In general, the chemical stability of an interface may differ from that of a free surface. For SRO, the volatility of RuO_2 [9] may play a role.

6.4   Magnetic properties

Having established a growth procedure leading to well defined terminations of the LSMO-SRO interface, the magnetic order in such samples has been investigated based on Superconducting quantum interference device (SQUID) magnetometry and X-ray magnetic circular dichroism (XMCD) measurements. The temperature dependence of magnetiza-
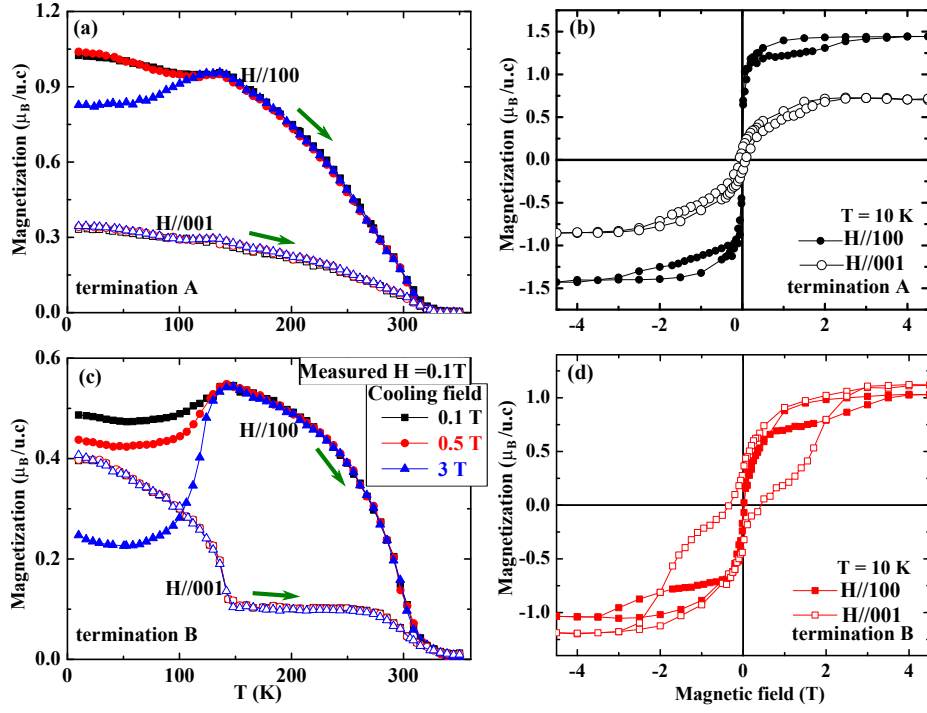
Figure 6.5: Temperature dependence of magnetization of the samples measured along H//100 and H//001 at 0.1 T after field cooling at 0.1 T, 0.5 T and 3 T of (a) termination A and (c) termination B type sample. Field dependence of magnetization of the samples measured along H//100 and H//001 at 10 K after field cooling at 0.5 T of (b) termination A and (d) termination B type sample.

tion of the samples is measured along H//100 and H//001 directions during warming from 10 K to 350 K at 0.1 T applied field after cooling at different fields [Fig.6.5 (a) and (c)]. The field dependence of magnetization of the samples is shown along H//100 and H//001 directions after cooling the samples in 0.5 T to 10 K [Fig.6.5 (b) and (d)]. The temperature dependence of magnetization data along H//100 show that in termination B-type samples the 9 uc thick LSMO layer orders at $T_C{}^{LSMO} \sim$ 310 K, while in termination A-type samples $T_C{}^{LSMO}$ is systematically larger by $5-10$ K. The reduced value of $T_C{}^{LSMO}$ measured in our films compared to that measured in bulk LSMO ($T_C{}^{LSMO} =$370 K) is due to the 0.75% biaxial tensile strain experienced by coherently grown LSMO films on STO(001) [10] and the finite-size effect experienced by films of few unit cells in thickness [11]. The Curie temperature of the SRO layer is $T_C{}^{SRO} \sim$ 140 K for both termination types. The drop of the magnetization M at $T_C{}^{SRO}$ reveals an antiferromagnetic (AFM) alignment of Ru spins to the Mn spins. In contrast to LSMO, SRO films have large magnetocrystalline anisotropy at low temperatures which prevents the Ru moments from aligning in a magnetic field of few Tesla. Magnetic order of ultrathin LSMO-SRO bilayers showing strong antiferromagnetic Mn-Ru coupling is quite complex at $T < T_C{}^{SRO}$, since four energy scales may be dominant depending on interface quality, layer thickness, temperature, magnetic field and sample history. These are the antiferromagnetic coupling at the interface, magnetic anisotropy energy, magnetostatic (stray field) energy and Zeeman energy in an external magnetic field. In the out-of-plane H//001 direction the magnetic
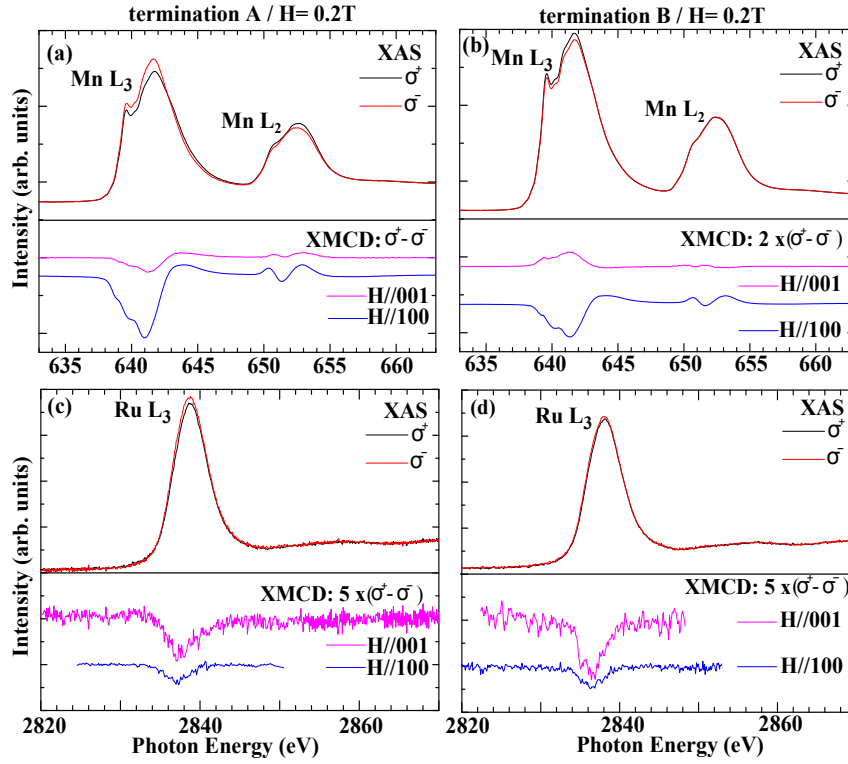
Figure 6.6: Ru L_3 and Mn $L_{2,3}$ XAS spectra (red and black curves) of termination A (a, c) and termination B (b, d) samples measured using circular polarized light at T=60 K and H=0.2 T. The difference spectrum (XMCD) is reported as blue and magenta curves for in-plane H//100 and out-of-plane H//001 magnetic field, respectively.

moment monotonically increases with decreasing temperature down to 10 K [Fig.6.5 (a) and (c)]. The magnetic hysteresis loop in in-plane H//100 for termination A type sample shows large remanent magnetization whereas the out-of-plane H//001 direction reveals some small remanent magnetization [Fig.6.5 (b)]. The out-of-plane hysteresis loop for termination B type sample is more hysteretic and shows larger remanent magnetization than the in-plane hysteresis loop, indicating out-of-plane canting of the magnetization.

In order to better understand the magnetic properties of LSMO/SRO bilayers there is need to disentangle the Mn and Ru contributions. The XMCD spectroscopy is an element-selective technique and, because the XMCD signal is proportional to the magnetization of the selected element, this technique has the great advantage to allow following the evolution of the contributions of Ru and Mn ions to the magnetization independently as a function of magnetic field. The XMCD data are recorded at 60 K after cooling the samples in 3 T. In Fig.6.6 is reported the representative Ru-L_3 XAS (c,d) and Mn-$L_{2,3}$ XAS (a,b) measured on termination A and termination B samples under an applied field of H=0.2 T at 60 K. The X-ray absorption (XAS) spectra are taken using circularly polarized light with the photon spin parallel (σ^+, red curves) and antiparallel (σ^-, black curves) to the magnetic field. The difference spectrum (σ^- - σ^+), i.e., the XMCD spectrum, is reported as blue (magenta) curve for H//100 (H//001). In the case of termination B the Mn XMCD signal has the opposite sign to that of Ru XMCD for H//001, while has the same sign for H//100. This result suggests that the termination B film is in a canted state with

Figure 6.7: Field-dependent magnetic order for termination A sample derived from XMCD spectra of Mn and Ru at 60 K. a, b) Mn-XMCD and c,d) Ru-XMCD intensity in grazing incidence in-plane orientation H//100 and perpendicular to the film plane H//001. Magnetic orientations of the layers are indicated in the layer schemes. The Ru canting angle may change gradually between lower (red) and upper (green) part of the SRO layer (c, d).

the components of the Ru and Mn magnetic moments antiferromagnetically coupled along the out-of-plane direction. In the case of termination A the Ru and Mn XMCD signals have the same sign for both H//100 and H//001. However, a simple XMCD spectra would not agree with our magnetization data and a more complex model involving the presence of the different magnetic moment orientations has to be considered.

In order to gain a deeper insight into the magnetic coupling at the interface and the switching behavior of Ru and Mn magnetic components, Mn- and Ru- L_3 edge XMCD spectra have been recorded as a function of magnetic field at 60 K along both, in-plane H//100 (at a grazing incidence angle of 20°) and out-of-plane H//001 directions yielding element-sensitive magnetic hysteresis loops (Fig. 6.7 and 6.8). Before each measurement, the sample was cooled in a field of 3 T. Blue and black curves indicate XCMD measurements versus increasing and decreasing magnetic field, respectively. The XMCD data of both Mn and Ru reveal very different magnetic behavior of termination A and B samples. For termination A, Mn moments have pronounced soft-magnetic characteristics with a saturation field of 30 mT [6.7 (a)]. The out-of-plane Mn-XMCD [6.7 (b)] reflects rotation of Mn moments by the field with very weak hysteresis. Hence, Mn spontaneous magnetization is along the 100 direction and can be switched as easily as in a single LSMO film. The in-plane Ru-XMCD loop [6.7 (c)] reveals a decrease when a positive

field of 3.5 T is reduced to zero, followed by an increase after the field turns negative. This peculiar behavior is mimicked by the hysteresis branch starting at large negative field. This can be interpreted in the following way. The maximum field of 3.5 T at 60 K is sufficient to break the antiferromagnetic coupling and align Ru and Mn moments to the field. The decreasing ordered Ru moment in reducing positive field reflects an enhanching antiparallel alignment of Ru spins to the Mn moments at the interface. The enhancement of Ru moment occurring after the field turns negative reflects the joined reversal of the antiferromagnetically coupled Ru and Mn moments at the interface. This leads to reorientation of the interface-near Ru moments along the positive direction. On the other hand, there is an upper, interface-far part of the SRO layer which is oriented to the external field, because the total Ru moment is positive at remanence. Moreover, the Ru in this upper part of the SRO layer is canted out-of-plane since the out-of-plane Ru-XMCD shows some remanence [6.7 (d)]. The Ru canting seems not to reach to the interface, because the coupled Mn does not show canting [as depicted in 6.7] (in contrast to the case of termination B where Mn canting is indeed found). This suggests that i) near the termination A interface, antiferromagnetically coupled Mn and Ru moments are aligned in-plane along 100 (and 010) directions and switch together in a magnetic field. Hence, they form an interface layer of rigidly coupled Mn and Ru moments. This is not the case for the termination B interface (details later). (ii) The SRO layer shows a depth-dependent rotation of Ru moments (very similar to an exchange-spring state [12]), in agreement with a polarized-neutron study by Kim *et* al. [13]. Possibly, the upper part of the SRO layer returns to the magnetic order of single SRO/STO(001) films [14], since the influence of the interface decays with distance.

Magnetic order and switching of the elements in termination B samples is qualitatively different. The Mn XMCD of termination B [Fig.6.8 (a) and (b)] shows, along both in-plane and out-of-plane directions, an inverted loop with negative remanence and saturation field of ~1 T. This reflects the antiferromagnetic coupling to the Ru moments aligned in field direction [Ru-XMCD, Fig.6.8 (c) and (d)] which cause the Mn moments to reverse in advance of the magnetic field. This behavior can be described by a positive exchange bias field [15]. Also, the large remanence shown by the out-of-plane Mn XMCD [6.8 (b)] indicates that the coupling with the Ru ions induces canting of the Mn moments to the out-of-plane direction. The in-plane and out-of-plane Ru XMCD signals display the typical squared hysteresis of a single-layer SRO film, which would suggest that the SRO layer behaves like a single film [Fig.6.8 (c) and (d)]. Hence, Mn and Ru switching can be understood based on antiferromagnetic coupling causing an exchange-bias effect.

More insights about the underlying physics can be gained from Fig. 6.9 showing field-cooled field-dependent and temperature-dependent magnetization measurements of bilayer films with termination A and B. Samples have been measured during cooling in constant in-plane magnetic field H // 100 to 20 K and subsequent warming in a small field (0.1 T). In Fig. 6.9, an obvious difference between the two terminations is the
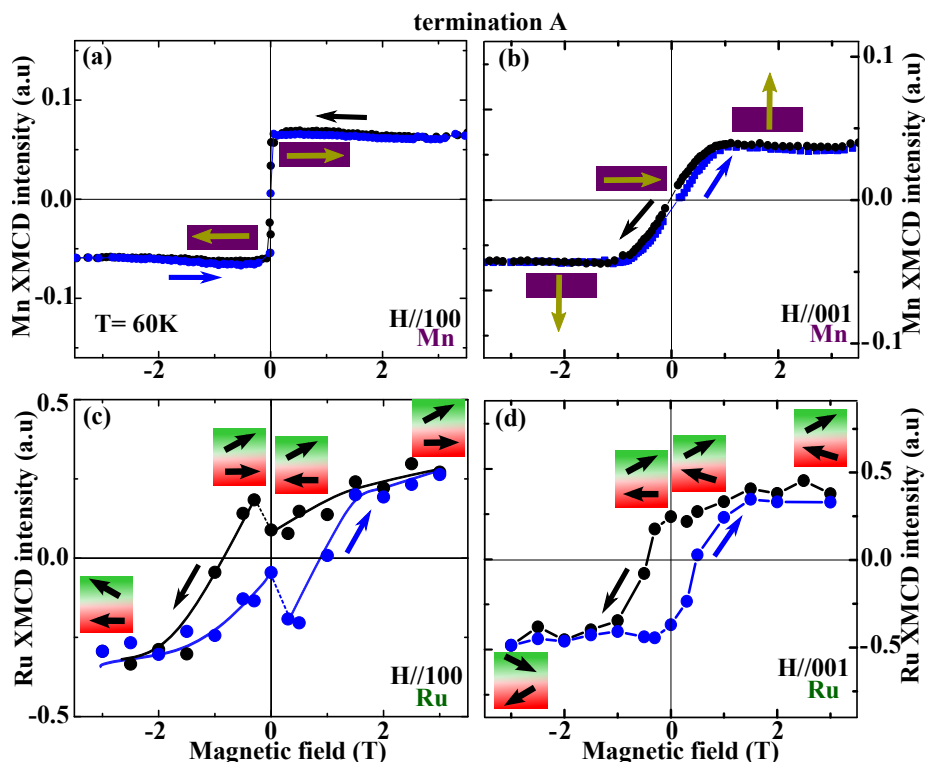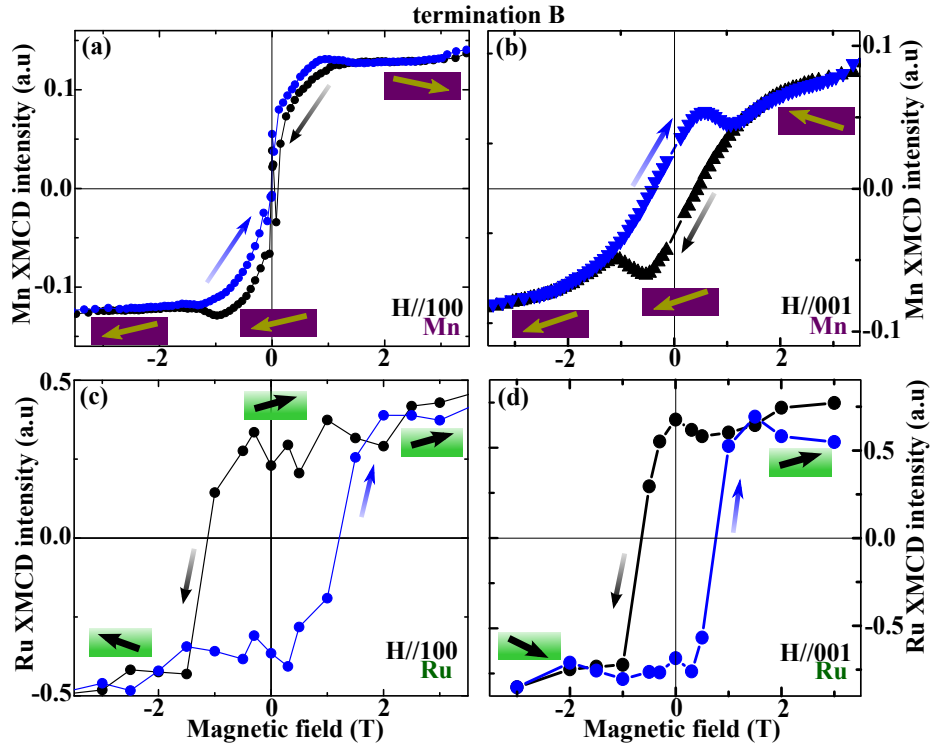
Figure 6.8: Field-dependent magnetic order for termination B sample derived from XMCD spectra of Mn and Ru at 60 K. a, b) Mn-XMCD and c,d) Ru-XMCD intensity in grazing incidence in-plane orientation H//100 and perpendicular to the film plane H//001. Magnetic orientations of the layers are indicated in the layer schemes.
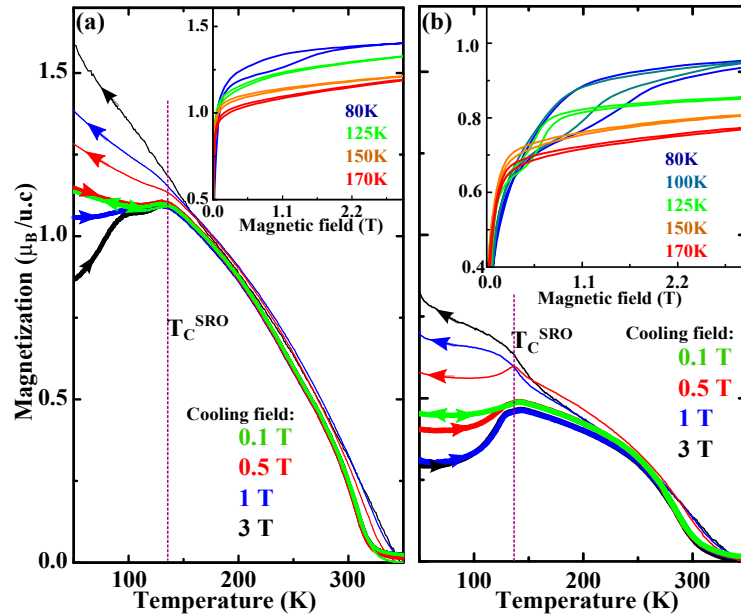
Figure 6.9: Magnetization measurements in an in-plane magnetic field H//100. Temperature dependence during field cooling (thin lines) and warming in 0.1 T (thick lines) for (a) termination A, (b) termination B sample. Inset: Field-dependent magnetization at constant temperatures.

antiferromagnetic coupling strength in the termination A-type samples compared to the B-type. Increasing the cooling field (H_{FC}) provides a measure for the antiferromagnetic (AFM) coupling strength, because at a certain field value the drop of M at T_C^{SRO} is suppressed and changes into an enhancement. A cooling field of 1 T suppresses the M drop at T_C^{SRO} in case of termination B [Fig. 6.9 (b)], whereas a field of 3 T is required in termination A [Fig. 6.9 (a)], confirming the larger coupling strength for termination A. The total magnetization grows with H_{FC}, indicating a gradually increasing alignment of both, Mn and Ru moments with the field against the antiferromagnetic interface coupling. After reducing the field at 20 K to 0.1 T, a spontaneous reduction of magnetization appears as expected, since Ru and Mn moments return to the antiferromagnetic alignment at the interface. Interestingly, the reduction of M grows with the cooling field (Fig. 6.9). At 20 K Ru moments may be fixed due to large magnetic anisotropy of SRO. Consequently, Mn would reverse in relation to the amount of positively aligned Ru moments at the interface. On the other hand, a Ru interface layer may reverse as observed in the 60 K XMCD data in Fig.6.7 (c). A qualitatively similar behavior of cooling and warming curves is observed for interface termination B [Fig. 6.9 (b)] because of the antiferromagnetic interface coupling. Here, one can conclude to have Mn reversal at 20 K upon switching off the cooling field, because this agrees with the Mn-XMCD hysteresis loop at 60 K [Fig.6.8 (a)], and the lower temperature enhances the magnetocrystalline anisotropy of SRO. On the other hand, canting of Mn and Ru moments causes additional magnetization rotation into the (001) plane for termination B.

An obvious further difference of termination A and B samples is the value of the saturated moment (M_S) of LSMO. Magnetization loops recorded at $T > T_C^{SRO}$ along a H//100 direction (Fig. 6.9, inset) have been used to estimate the saturated magnetic moment. Termination A samples show ∼1.2 μ_B/u.c. (3.1 μ_B/Mn) at 150 K and 3 T, compared to 0.9 μ_B/u.c. (2.3 μ_B/Mn) in termination B samples. (All magnetization values have an error from uncertainty of sample area of ∼10 %.) The magnetization difference of ∼0.3 μ_B/u.c. has been observed in many sample pairs which is a robust experimental feature. The often reproduced reduction of the Mn ordered moment in termination B samples probably indicates the realization of an antiferromagnetically coupled first Mn atomic layer from the top LSMO surface. The existence of antiferromagnetic first Mn layer is in line with earlier published work [16, 17].

The rigid coupling of Mn and Ru into a jointly switching Mn-Ru moment at the termination A interface is in agreement with the prediction of very strong coupling from DFT (calculation done by I. Maznichenko, MLU Halle-Wittenberg) [18]. Notably, the calculated coupling constant J between Mn and Ru across the interface is larger by about a factor of 3 for termination A which is in agreement with the experimental results. On the other hand, one cannot include all structural aspects of real interfaces into the calculations. Therefore, we consider the possible role of further relevant aspects. These include

i) elastic effects such as the coupling of rotations of oxygen octahedra at the interface [19, 20] and chemical effects (point defects from interdiffusion, oxygen vacancies), ii) different charge transfer at the interface [15, 21].

SRO as a single film on STO(001), in the same strain state as in the present samples, is tetragonal at the growth temperature of 700 °C [22]. It undergoes a phase transition to orthorhombic *Pbnm* symmetry (with the Glazer notation $a^-b^-c^+$ of octahedral rotations) at about 280 °C [22]. The magnetic anisotropy of termination B samples agrees with that of orthorhombic SRO films [14], indicating orthorhombic symmetry of the SRO layer. In contrast, termination A samples show tetragonal symmetry with 100 and 010 in-plane easy axes near the interface, in resemblance to SRO films under tensile strain [23]. The symmetries are associated with distinct rotational patterns of oxygen octahedra in SRO [20]. Thus, one expects the transfer of octahedral rotations between LSMO and SRO to be of importance for the lattice structure at the interface and, consequently, the magnetic ordering. At this point one may suspect the growth sequence to induce the altered symmetry of SRO in termination A samples. However, SRO is tetragonal at the growth temperature and assumes orthorhombic symmetry during cooling when the LSMO-SRO interface is complete and the elastic interaction between LSMO and SRO should be independent of the growth direction. Hence, the different symmetry of SRO at the termination A interface is not a result of the elastic transfer of octahedral rotations, because this rotation transfer should be present for both terminations.

Point defects at the interfaces may occur as an enrichment of oxygen vacancies [20, 24] or as interdiffused metal ions. Lu *et* al. showed that oxygen-deficient SRO films have a magnetic anisotropy with a magnetic easy axis perpendicular to the film plane and tetragonal symmetry [25]. This is not observed in our samples. The modest B site interdiffusion found by STEM at the termination B interface is unlikely to be the origin of the weaker magnetic coupling for this termination of the LSMO-SRO interface since the theoretical results support the strongly different coupling for interdiffusion-free interfaces.

If one considers the ionic model, the electronic reconstruction will be different at the interfaces. $SrRuO_3$ consists of alternating $Sr^{2+}O^{2-}$ and $Ru^{4+}(O^{2-})_2$ atomic layers. Both atomic layers are charge neutral. On the other hand, $La_{0.7}Sr_{0.3}MnO_3$ consists of positively charged $(La_{0.7}Sr_{0.3})^{2.7+}O^{2-}$ and negatively charged $Mn^{3.3+}(O^{2-})_2$ (Mn with nominal mixed valence state assumed, Mn^{3+}/Mn^{4+}) atomic layers, attaining neutrality through interlayer charge transfer. When SRO is grown on top of LSMO (termination A) negative charge exhibits at the interface between the MnO_2 and SrO atomic planes. But when LSMO is grown on top of SRO (termination B) charge transfer occurs between the RuO_2 and (La,Sr)O atomic planes, thus positive charge exhibits at the interface [15, 26]. So, $(MnO_2)^-/(SrO)^0$ interface has different charge valence state which leads to different charge transfer than the $(RuO_2)^0/((LaSr)O)^+$ interface and they may have a different local hole concentration. Depending on the hole concentration and range of the charge transfer, the interfacial coupling could be different at the different terminations [21, 27].

However, both LSMO and SRO are metals, making an electronic charge redistribution easy and, thus, any ionic reconstruction or interdiffusion can be avoided. Similar charge transfer has been suggested as the origin of unexpected magnetic configurations at other perovskite oxide interfaces [26, 27].

6.5   Conclusion

In summary, the LSMO-SRO system serves as an useful platform where one can get the different atomic termination at interface by altering the sequence layer of the materials, i.e. MnO_2/SrO atomic termination at the interface after growing LSMO and, subsequently, SRO on TiO_2-terminated $SrTiO_3(001)$ (STO). The reversed layer sequence (LSMO/SRO/STO(001)) nominally leads to the $RuO_2/(La,Sr)O$ atomic termination at the interface. The different atomic terminations at the interface have strong influence on the resulting properties of the oxide heterostructures. In particular, stronger antiferromagnetic interfacial exchange coupling has been observed in MnO_2/SrO atomic termination case. The magnetic measurements suggest a structural change of SRO layers i.e. tetragonal lattice symmetry of SRO in termination A and orthorhombic (monoclinic) symmetry of SRO in termination B. In termination A, a new interface layer is formed, where the Mn and Ru moments are rigidly antiferromagnetically coupled and switch together in a magnetic field. On the other hand in termination B, a more conventional antiferromagnetic interface coupling is observed.

Bibliography

[1] A. Ohtomo and H. Y. Hwang, "A high-mobility electron gas at the $LaAlO_3/SrTiO_3$ heterointerface," Nature , **423** (2004).

[2] M. Basletic, J.-L. Maurice, C. Carrétéro, G. Herranz, O. Copie, M. Bibes, É. Jacquet, K. Bouzehouane, S. Fusil & A. Barthélémy, "Mapping the spatial distribution of charge carriers in $LaAlO_3/SrTiO_3$ heterostructures," Nat. Mater. **7**, 621 (2008).

[3] P. Yu, W.Luo, D.Yi, J. X. Zhang, M. D. Rossell, C.-H. Yang, L.You, G. Singh-Bhalla, ,S.Y.Yang, Q.He, Q. M. Ramasse, R. Ern, L. W. Martin, Y.H.Chu, S. T. Pantelides, S. J. Pennycook, and R. Ramesh, "Interface control of bulk ferroelectric polarization," PNAS **109**, 9710 (2012).

[4] M. Gibert, M. Viret, A. Torres-Pardo, C. Piamonteze, P. Zubko, N. Jaouen, J.-M. Tonnerre, A. Mougin, J. Fowlie, S. Catalano, A. Gloter, O. Stephan, and J.-M. Triscone, "Interfacial Control of Magnetic Properties at $LaMnO_3/LaNiO_3$ Interfaces," Nano Lett. **15**, 7355 (2015).

[5] Eric J. Monkman, Carolina Adamo, Julia A. Mundy, Daniel E. Shai, John W. Harter, Dawei Shen, Bulat Burganov, David A. Muller, Darrell G. Schlom & Kyle M. Shen, "Quantum many-body interactions in digital oxide superlattices," Nat. Mater. **11**, 855 (2012).

[6] E. J. Moon, R. Colby, Q. Wang, E. Karapetrova, C. M. Schlepütz, M. R. Fitzsimmons & S. J. May, "Spatial control of functional properties via octahedral modulations in complex oxide superlattices," Nat. Comm. **5**, 5710 (2014).

[7] Reinald Hillebrand, Eckhard Pippel, Dietrich Hesse, and Ionela Vrejoiu, "A study of intermixing in perovskite superlattices by simulation-supported C_s-corrected HAADF-STEM," Phys. Status Solidi A **208**, 2144 (2011).

[8] G. Rijnders, D. H. A. Blank, J. Choi, and C. B. Eom, "Enhanced surface diffusion through termination conversion during epitaxial $SrRuO_3$ growth," Appl. Phys. Lett. **84**, 505 (2004).

[9] H.N. Lee, H. M. Christen, M. F. Chisholm, C. M. Rouleau, and D. H. Lowndes, "Thermal stability of epitaxial SrRuO$_3$ films as a function of oxygen pressure," Appl. Phys. Lett. **84**, 4107 (2004).

[10] C. Thiele, K. Dörr, O.Bilani, J.Rödel, and L. Schultz, "Influence of strain on the magnetization and magnetoelectric effect in La$_{0.7}$A$_{0.3}$MnO$_3$/PMN-PT (001) (A=Sr,Ca)," Phys. Rev. B **75**, 054408 (2007).

[11] M. Huijben, L. W. Martin, Y.-H. Chu, M. B. Holcomb, P. Yu, G. Rijnders, D. H. A. Blank, and R. Ramesh, "Critical thickness and orbital ordering in ultrathin La$_{0.7}$Sr$_{0.3}$MnO$_3$films," Phys. Rev. B **78**, 094413 (2008).

[12] S. Mangin, G. Marchal, and B. Barbara, '' Evidence of Exchange-Bias-Like Phenomenon in GdFe/TbFe/GdFe Domain Wall Junctions,'' Phys. Rev. Lett. **82**, 4336 (1999).

[13] J.-H. Kim, I. Vrejoiu, Y. Khaydukov, T. Keller, J. Stahn, A. Ruhm, D. K. Satapathy, V. Hinkov and B. Keimer, "Competing interactions at the interface between ferromagnetic oxides revealed by spin-polarized neutron reflectometry," Phys. Rev. B **86**, 180402(R) (2012).

[14] M. Ziese, I. Vrejoiu and D. Hesse, "Structural symmetry and magnetocrystalline anisotropy of SrRuO$_3$ films on SrTiO$_3$," Phys. Rev. B **81**, 184418 (2010).

[15] X. Ke, M. S. Rzchowski, L. J. Belenky, and C. B. Eom, "Positive exchange bias in ferromagnetic La$_{0.67}$Sr$_{0.33}$MnO$_3$/SrRuO$_3$ bilayers," Appl. Phys. Lett. **84**, 5458 (2004).

[16] N. M. Nemes, M. J. Calderón, J. I. Beltrán, F. Y. Bruno, J. G.-Barriocanal, Z. Sefrioui, C. León, M. G.-Hernández, M. C.n Muñoz, L. Brey, and J. Santamaría, "Signatures of a Two-Dimensional Ferromagnetic Electron Gas at the La$_{0.7}$Sr$_{0.3}$MnO$_3$/SrTiO$_3$ Interface Arising From Orbital Reconstruction,'' Adv. Mater. **26**, 7516 (2014).

[17] S Valencia, L Peña, Z Konstantinovic, Ll Balcells, R Galceran, D Schmitz, F Sandiumenge, M Casanove and B Martínez, "Intrinsic antiferromagnetic/insulating phase at manganite surfaces and interfaces'' J. Phys. Cond. Mat. **26**, 166001 (2014).

[18] M. Ziese, I. Vrejoiu, E. Pippel, P. Esquinazi, D. Hesse, C. Etz, J. Henk, A. Ernst, I.V. Maznichenko, W. Hergert, and I. Mertig, "Tailoring Magnetic Interlayer Coupling in La$_{0.7}$Sr$_{0.3}$MnO$_3$/SrRuO$_3$ Superlattices," Phys. Rev. Lett. **104**, 167203 (2010).

[19] S. J. May, J.-W. Kim, J. M. Rondinelli, E. Karapetrova, N. A. Spaldin, A. Bhattacharya, and P. J. Ryan, "Quantifying octahedral rotations in strained perovskite oxide films,'' Phys. Rev. B **82**, 014110 (2010).

[20] A. Vailionis, H. Boschker, Z. Liao, J. R. A. Smit, G. Rijnders, M. Huijben, and G. Koster, "Symmetry and lattice mismatch induced strain accommodation near and away from correlated perovskite interfaces," Appl. Phys. Lett. **105**, 131906 (2014).

[21] A. Urushibara, Y. Moritomo, T. Arima, A. Asamitsu, G. Kido, and Y. Tokura, "Insulator-metal transition and giant magnetoresistance in $La_{1-x}Sr_xMnO_3$," Phys. Rev. B **51**, 14103 (1995).

[22] K. J. Choi, S. H. Baek, H. W. Jang, L. J. Belenky, M. Lyubchenko, C.B. Eom, "Phase-Transition Temperatures of Strained Single-Crystal $SrRuO_3$ Thin Films," Adv. Mater. **22**, 759 (2010).

[23] A. Herklotz, M. Kataja, K. Nenkov, M. D. Biegalski, H.-M. Christen, C. Deneke, L. Schultz, and K. Dörr, "Magnetism of the tensile-strain-induced tetragonal state of $SrRuO_3$ films," Phys. Rev. B **88**, 144412 (2013).

[24] A. Y. Borisevich, A. R. Lupini, J. He, E. A. Eliseev, A. N. Morozovska, G. S. Svechnikov, P. Yu, Y. H. Chu, R. Ramesh, S. T. Pantelides, S. V. Kalinin, and S. J. Pennycook, "Interface dipole between two metallic oxides caused by localized oxygen vacancies," Phys. Rev. B **86**, 140102(R).

[25] W. Lu, P. Yang, W. D. Song, G. M. Chow, and J. S. Chen, "Control of oxygen octahedral rotations and physical properties in $SrRuO_3$ films," Phys. Rev. B **88**, 214115 (2013).

[26] K. S. Takahashi, M. Kawasaki, and Y. Tokura, "Interface ferromagnetism in oxide superlattices of $CaMnO_3/CaRuO_3$," Appl. Phys. Lett. **79**, 1324 (2001).

[27] M. Izumi, Y. Ogimoto, Y. Konishi, T. Manako, M. Kawaski, and Y. Tokura, "Perovskite superlattices as tailored materials of correlated electrons," Mater. Sci. Eng. B **84**, 53 (2001).

Chapter 7

Strain and interface effects on magnetic order of $La_{0.7}Ca_{0.3}MnO_3$/SrTiO$_3$ superlattices

This chapter explores the strain-induced changes of magnetic order in epitaxially grown [La$_{0.7}$Ca$_{0.3}$MnO$_3$(2.6 nm)/SrTiO$_3$(6.3 nm)]$_{15}$ superlattices (SLs). SLs are simultaneously grown by Pulsed Laser Deposition (PLD) on (001)-oriented SrTiO$_3$ (STO), LaAlO$_3$ (LAO) and piezoelectric 0.72Pb (Mg$_{1/3}$Nb$_{2/3}$)O$_3$-0.28PbTiO$_3$ (PMN-PT) substrates in order to obtain different residual strain states. The La$_{0.7}$Ca$_{0.3}$MnO$_3$ layers show tensile strain (ε=1.0%) for SL/LAO and even larger strain on STO (ε=1.7%) and PMN PT (ε=1.8%). The magnetization has been measured and is found to be quite different for the three SLs. Application of reversible biaxial compression using the PMN -PT substrate reveals the direct strain effect on magnetic order.

7.1 Introduction

The family of rare-earth manganites (R, A)MnO$_3$ (R=La, Pr or Nd, A=Ca, Ba or Sr) has drawn great research interest especially due to the colossal magnetoresistance (CMR) effect and the high electronic spin polarization [1, 2, 3, 4]. Superlattices (SLs) are widely studied for phenomena of magnetic interfacial coupling and spin-polarized electrical transport which are important from the perspectives of both, technology (magnetic sensors, magnetic memory devices and spintronic applications) and fundamental physics [5, 6, 7, 8, 9]. Phenomena such as magnetic exchange bias and strong antiferromagnetic interfacial coupling (with SrRuO$_3$ interlayers) have been observed in superlattices with manganite layers recently [10, 11, 12]. In order to improve knowledge on such oxide interfaces, the parameters of influence on magnetic order at the interfaces need to be identified. Many researchers have reported the suppression of ferromagnetic order in [La$_{1-x}$A$_x$MnO$_3$ /SrTiO$_3$]$_n$ (A = Sr or Ca, x= 0.2-0.4) SLs as the thickness of the manganite layers decreases [13, 14, 15, 16, 17, 18, 19]. Secondly, Millis et al. revealed that the Curie tem-

perature (T_C) and magnetic order are very sensitive to biaxial strain [20, 21]. Thirdly, Jo et al. attributed the loss of magnetic moment in $La_{0.7}Ca_{0.3}MnO_3/SrTiO_3$ SLs to magnetically disordered interfaces [22]. Hence, three parameters of influence on the manganite layer's magnetic order are the layer thickness, the elastic strain and the interface to the adjacent layer. The last point is rather non-specific and includes intrinsic effects from an ideal interface as well as defect-related effects. For example, atomic intermixing and dislocations have been identified as an origin of suppressed magnetic order at the interfaces of $La_{0.7}Sr_{0.3}MnO_3/SrTiO_3$ superlattices [19]. The density of such defects could be controlled by altering the laser spot size on the ceramic target, since the cation composition of the manganite layers has been found to be sensitive to this parameter [19, 23]. Intrinsic effects include the type of the chemical termination at the perovskite-lattice interfaces and proximity effects from the electronic structure of the adjacent layer.

Many recent experiments deal with SLs on STO (001) substrates due to the availability of a single TiO_2 termination at the $SrTiO_3$ surface and the rather readily achievable coherent growth of manganite/$SrTiO_3$ SLs on this substrate [7, 24, 25, 26, 27, 28]. A detailed structural, transport and magnetic characterization of $La_{0.7}Ca_{0.3}MnO_3/SrTiO_3$ heterostructure has been presented by Lu *et al.*and Liang *et al.* [24, 25]. Even though it has been recognized that elastic strain is a vital parameter governing the electronic state of complex oxide interfaces, different strain states of a particular superlattice type are rarely compared. The reason for this is found in the experimental challenges. Coherent growth on an oxide substrate implies straining all layers to match the substrate lattice. This works only for low lattice misfits between all components or for a very low total thickness [29]. Secondly, strain control may utilize the mismatch between the SL component layers relying on coherent growth inside the SL. In this case, a fully relaxed growth on the substrate would be desirable which is also not easily obtained. Hence, it is not astonishing to find that few oxide perovskite SLs have been investigated in different well-defined strain states and the impact of strain on magnetic order at the interfaces is not well known. Here the strain-induced changes of magnetic order in epitaxially grown $La_{0.7}Ca_{0.3}MnO_3/SrTiO_3$ SLs have been investigated. The SLs are simultaneously grown by Pulsed Laser Deposition (PLD) on (001)-oriented STO, LAO and piezoelectric PMN-PT substrates in order to obtain different (residual) strain states, although no coherent growth on LAO and on PMN-PT could be expected because of the large lattice misfit. The $La_{0.7}Ca_{0.3}MnO_3$ layers in the SLs are under medium tensile strain on LAO (ε=1%) and strong tensile strain on STO ($\varepsilon\sim1.7\%$) and PMNPT ($\varepsilon\sim1.8\%$), respectively. Reversible biaxial compression of the SL on the PMN-PT substrate reveals the direct strain effect on magnetic order (T_C as well as magnetization), which has been compared to the data for the different static strain states in the three samples. The contribution of elastic strain is found to be substantial, but does not completely account for the different behavior of the samples.
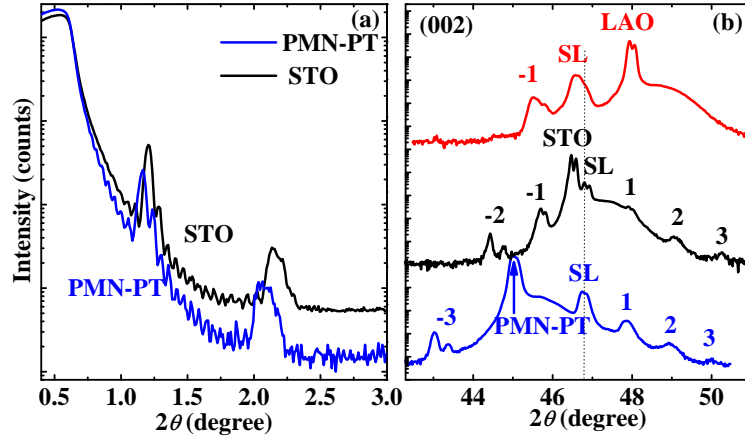
Figure 7.1: (a) X-ray reflectivity measurement of [LCMO/STO]$_{15}$ SLs on STO (black curve) and PMN-PT (blue curve). (b) X-ray θ-2θ diffraction pattern around the (002) peak of the SLs on LAO, STO and PMN-PT substrates. Double peaks arise from K$_{\alpha1}$, K$_{\alpha2}$ reflections. The curves are vertically displaced for clarity.

7.2 Sample preparation

[La$_{0.7}$Ca$_{0.3}$MnO$_3$(LCMO)/SrTiO$_3$(STO)]$_{15}$ SLs are grown simultaneously on (001)-oriented LAO, STO and piezoelectric PMN-PT substrates by off-axis Pulsed Laser Deposition from stoichiometric ceramic targets of LCMO and STO. The three substrates lay on a rotating substrate plate in a home-made tube furnace in the PLD chamber, ensuring homogeneous layer thicknesses. The deposition temperature was 650 ^{0}C, the oxygen pressure 0.1mbar and the laser energy density was approximately 2.5 J/cm^2 with frequency 3Hz. The SLs have been annealed after deposition at 650 ^{0}C for 45 min at 700 mbar pure O$_2$ pressure. The deposition starts with LCMO which is the bottom layer of the SL and finishes with STO as the top layer of the SL. In total, 15 double layers of LCMO and STO have been deposited.

7.3 Structural characterization

The structural characterization of the epitaxial nature of these SLs has been carried out by using a Phillips X'pert MRD diffractometer with Cu$K\alpha$ radiation. In Fig.7.1(a) the x-ray reflectivity curves of the SLs on STO and PMN-PT are plotted. X-ray reflectivity data of the SLs indicate well defined interfaces between the LCMO and STO layers. The total thickness of the sample is calculated from d=λ /(2$\Delta\theta$), where λ is the x-ray wavelength and $\Delta\theta = \theta_i - \theta_{i-1}$, θ_i is the angle of the i^{th}order fringe. Using a simulation of the reflectivity data, the individual film thicknesses d_1 and d_2 of the LCMO and STO layers, respectively, are calculated. The values of d, d_1 and d_2 are shown in Table I. d_1= 2.6 nm means a layer thickness of 6–7 pseudocubic unit cells.

Fig.7.1(b) represents the θ-2θ diffraction patterns near the (002) reflection for the [LCMO/STO]$_{15}$ SLs. Several distinct satellite peaks (marked as $1, 2, \ldots, -1, -2, \ldots$ etc.)

Table 7.1: Structural properties of the superlattice samples grown on LAO, STO and PMN-PT substrates: film thicknesses of LCMO (d_1) and STO (d_2), SL period (Λ), total thickness (d), average out-of-plane (c) and in-plane (a) lattice parameter.

Sample	d_1(nm)	d_2(nm)	Period Λ(nm)	Total thickness d(nm)	c (Å)	a (Å)	c/a
SL/LAO	2.6	6.3	8.9	133	3.90	3.88	1.005
SL/STO	2.5	6.3	8.8	132	3.87	3.905	0.991
SL/PMN-PT	2.6	6.3	8.9	135	3.88	3.91	0.992
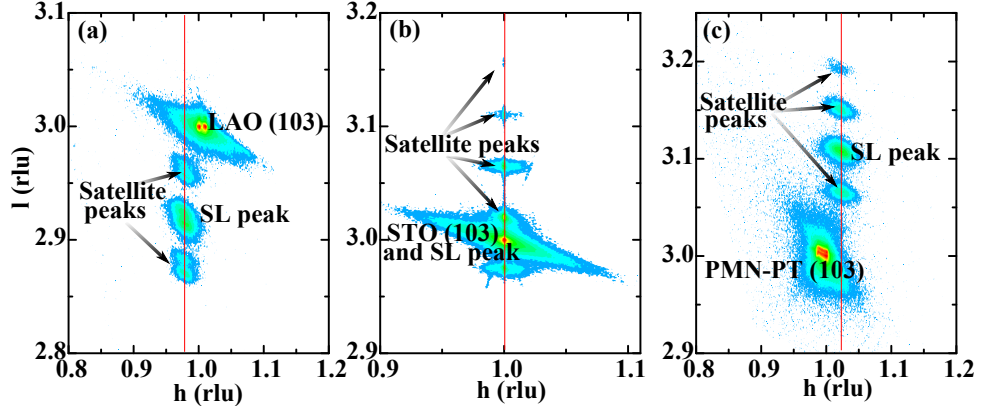
Figure 7.2: Reciprocal Space Maps around the (103) reflection of the SLs. Substrates peak, SL peak and satellites are indicated.

around the main peak (002) are observed, indicating the periodic structure of the SL as well as reasonably smooth interfaces. It should be noted that the (002) peak position is shifted for the different substrates, reflecting a strain-induced change of the average out-of-plane lattice parameter (c). The positions of the (002) film peaks are at $2\theta = 46.54^0$, 46.82^0, 46.74^0, in consistence with the values of c given in Table 7.1. The modulation period $\Lambda = d_1 + d_2$ of the SLs, calculated from direct measurements of d_1 and d_2, is in good agreement with the estimated value using $\Lambda = (n_i - n_{i-1})\lambda / [2(\sin\theta_i - \sin\theta_{i-1})]$, with n_i as the number corresponding to i^{th} order oscillation of the fringe and θ_i as the angle of that particular i^{th} order fringe. The calculated period of the SLs is shown in Table 7.1.

Coherent growth of the SL in its interior, but not of the SL on the substrates of LAO and PMN-PT, is confirmed by XRD reciprocal space maps (RSM) around the (103) reflection (Fig.7.2). The in-plane (a) and out-of-plane (c) lattice parameters are calculated from the RSM. The average lattice parameters of the SLs grown on LAO / STO / PMN-PT are a=3.88 / 3.905 / 3.91 Å, and c=3.90 / 3.87 / 3.88Å, respectively (Table 7.1). The c parameter represents an average of the c parameters of the two components, weighted with the thickness of the respective layers. The c lattice parameters measured this way agree with the ones calculated from θ-2θ diffraction patterns. The SL on LAO is tetragonally distorted with $c/a > 1$, whereas the SLs on PMN-PT and STO show a rather similar value of $c/a < 1$ (Table 7.1). Taking the pseudocubic bulk lattice constants of LCMO (3.84Å)

into account, we infer that LCMO is under in-plane tensile strain of 1.0 / 1.7 / 1.8% for SLs grown on LAO / STO / PMN-PT, respectively. This reveals that different strain states have been obtained in the SLs on different substrates, even though the growth is not coherent on the LAO and PMN-PT substrates. The origin for the different strain states is a residual strain which may partially result from thermal expansion mismatch.

7.4   Magnetization

The magnetization measurements have been carried out by using SQUID (superconducting quantum interference device) magnetometry. The magnetization is expressed in Bohr magnetons per Mn atom.

7.4.1   Temperature and field dependence of magnetization

In Fig.7.3, temperature and magnetic field dependences of the magnetization of the SLs are shown. The temperature-dependent magnetization $[M(T)]$ is measured after field cooling (FC) in a magnetic field of 0.1 T applied along an in-plane [100] direction [Fig.7.3 (a)]. For all the SLs the quadratic magnetization $M^2(T)$ is approximately linear in a temperature range below the Curie temperature (T_C); by extrapolating the linear part of $M^2(T)$ towards $M = 0$ the value of T_C is derived [Fig.7.3 (a) inset]. The paramagnetic (PM) to ferromagnetic (FM) transition is apparent at $T_C = 104.8$ / 99.7 / 89.8 K for SLs grown on LAO / STO / PMN-PT, respectively. With decreasing temperature, the magnetization increases up to 1.01 / 0.88 / 0.52 μ_B / Mn for SLs grown on LAO / STO / PMN-PT, respectively. It has been reported before that elastic strain reduces T_C of ferromagnetic manganite layers, since the ferromagnetic double exchange (DE) interaction is strongest for a cubic symmetry of the unit cell [18, 30]. In the present work, the LCMO layers of the SLs suffer from rather strong tensile strain, which is smaller for the SL on LAO. Hence, the large tensile strain of the LCMO layers on STO and PMN-PT is reflected in a lowering of T_C, in comparison to the SL on LAO. The strong reduction of T_C from the bulk value of 250 K for LCMO is essentially a result of the reduced layer thickness with $d_1 \sim$ 6 unit cells [31, 32]. We have checked that a strain-relaxed thicker film of LCMO grown under the same conditions has a Curie temperature close to the bulk value. At the low thickness of 6 unit cells, also the interfaces to the SrTiO$_3$ layers affect the magnetic order significantly.

In Fig.7.3(b), the magnetic hysteresis loops at 10 K are shown after eliminating the diamagnetic contribution of the substrates. The magnetic field (H) is applied parallel to the film plane along an [100] direction. The SL on LAO reveals the highest saturation magnetization (M_S, as measured at 2 T), whereas M_S decreases with tensile strain and is lowest in the SL grown on PMN-PT substrate. The saturated moments at 2 T are 1.97 / 1.36 / 0.98 μ_B/Mn for the SLs grown on LAO / STO / PMN-PT, respectively. Due to difficulties in accurately determining the layer thickness and the in-plane area of
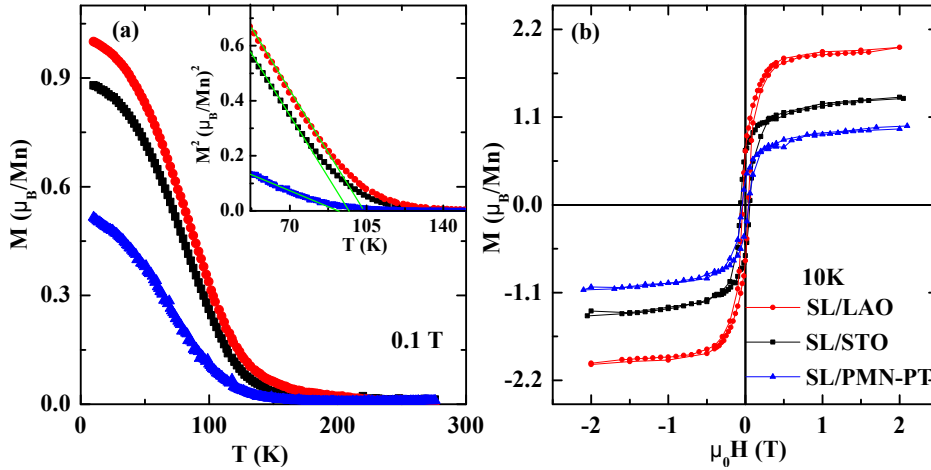
Figure 7.3: (a) Temperature dependence of magnetization (M) for the [LCMO/STO]$_{15}$ SLs on LAO, STO and PMN-PT substrates. Magnetization was measured in a magnetic field of 0.1 T applied along an in-plane [100] direction after field cooling (0.1 T). Inset: Straight line fitted to the linear range of $M^2(T)$ of SLs to determine the apparent T_C. (b) M-H curves for the SLs measured at 10K after field cooling (0.1 T).

the SLs, there is an uncertainty of about 8-10% in the above values. M_S is much lower than expected for ferromagnetically ordered Mn moments; in the latter case a value of 3.7 μ_B/Mn would be obtained for a mixed Mn valence with 30% Mn^{4+}. The decrease is not linear with increasing tensile strain; in particular, the change between the SLs on STO and PMN-PT is unexpectedly large for the small strain variation and indicates a different parameter of influence such as the interface properties.

7.4.2 Reversible strain-dependent of magnetization

To measure the direct strain dependence of magnetization, we use the SL on PMN-PT substrate for providing electrically controllable reversible biaxial strain. We use a silver paint contact on top of the SL and a NiCr/Au electrode on the bottom face of the 0.3 mm thick PMN-PT crystal for applying an electric field $E \leq 10$ kV/cm along the substrate normal [Fig.7.4 (a)]. After poling the crystal, the resulting current through the piezo-crystal is < 1 µA. The PMN-PT substrate shrinks approximately linearly with substrate voltage along both [100] and [010] in-plane directions, under-going a compression of about 0.1% in an electric field of $E =$10 kV/cm [33, 34]. Fig.7.4 (b) shows an example for the approximately linear growth of the magnetization along a [100] in-plane direction at 100 K and 0.1 T of magnetic field when the substrate voltage increases. This observation gives evidence for the direct effect of strain on magnetization. After field-cooling, the applied field of 0.1 T is sufficient to remove the domains; hence, the observed change in magnetization is not caused by domain processes [Fig.7.4 (b)].

In Fig.7.4 (c), two $M(T)$ curves are recorded in two strain state $E = 0$ and 10 kV/cm in a 0.1 T magnetic field along a [100] direction. Upon the piezoelectric compression of the sample, the total magnetization as well as T_C are enhanced. A large shift of T_C per
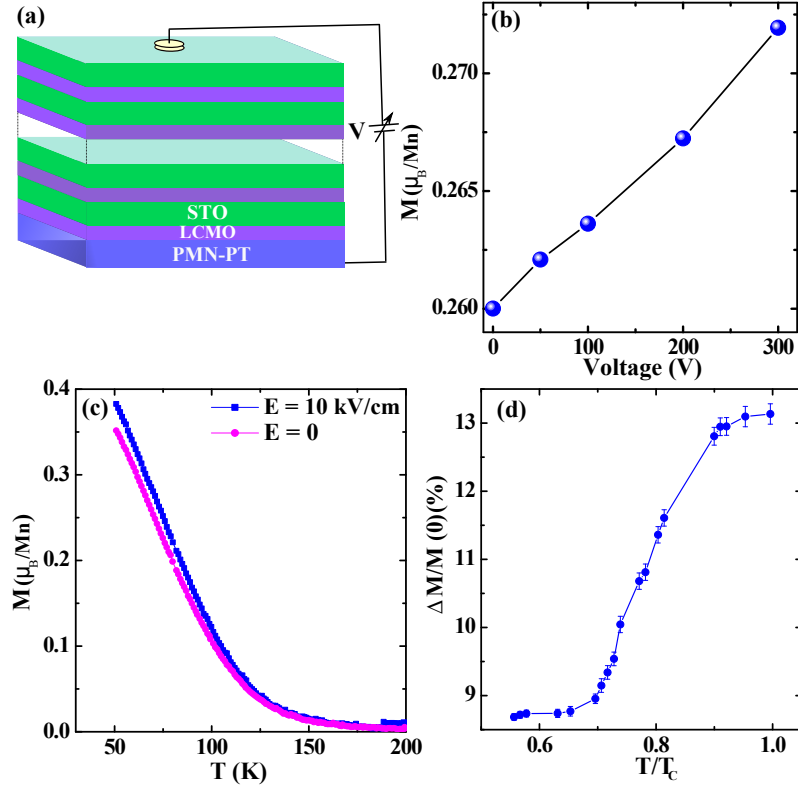
Figure 7.4: (a) Schematic diagram of reversible strain application, (b) Magnetization vs substrate voltage at 100 K. M is recorded along an [100] in-plane direction after field cooling in 0.1 T. (c) Temperature dependence of magnetization in two different strain states for H = 0.1 T, (d) $\Delta M/M(0)$ vs T at $E = 10$ kV/cm.

strain ($dT_C/d\varepsilon$) of up to 190 K/% has been observed in thin strained $La_{0.7}Sr_{0.3}MnO_3$ films earlier [35]. From our $M(T)$ data, the estimated T_C is 93.2 K for $E = 10$ kV/cm. The observed shift of T_C is 3.4 K, which sets the value of $dT_C/d\varepsilon$ approximately to be 34 K / %. The temperature dependence of the relative strain-induced change in M, $\Delta M/M(0) = (M(E)\text{-}M(E=0)) / M(0)$ is shown in Fig.7.4 (d). The magnetoelastic response $\Delta M/M(0)$ reaches a maximum of about 13.1% near T_C and drops continuously with decreasing the temperature to a value of ~8.7% which appears to be stable with further reduction of temperature. It is attributed to a strain-induced shift of T_C, which leads to the maximum response of magnetization near T_C [34]. Interestingly, the $\Delta M/M(0)$ value near T_C is within the range of values of 13%–21% found for coherent $La_{0.7}Sr_{0.3}MnO_3/SrTiO_3$ superlattices with manganite layer thicknesses of 2.2–13 nm earlier [13]. One should note that the measurement shown in Fig.7.4 (b) is taken at $T> T_C$ and gives a $\Delta M/M(0) = 4.6\%$. The non-vanishing magnetization above T_C is a consequence of the T_C estimation procedure and the fact that the field of 0.1 T induces additional magnetic order. The non-zero value of $\Delta M/M(0)$ observed at $T << T_C$ reveals that an influence of strain on magnetic ordering is still present even at low temperatures. This is consistent with the fact that the LCMO layers are not completely ferromagnetically ordered at low T, because an aligned ferromagnet cannot respond by further ordering to the strain. In the present sample, the reversible compression obviously increases the degree of magnetic order in the

ground state.

7.5   Discussion

The static and reversible strain effects on the magnetic order of the superlattices can be compared in order to find out, in what degree the strain states are responsible for the different behavior of the SL samples. We consider the three parameters of influence identified above, i. e. (i) the LCMO layer thickness, (ii) the biaxial strain of LCMO layers and (iii) the interface to adjacent STO layers. Regarding (i), the different strain levels or the reversible strain of $< 0.1\%$ have a negligible effect on layer thickness. The values of d_1 as obtained from the simulation of reflectivity data are slightly different (Table 7.1), but the observed variation of $<5\%$ is in the error range and is unlikely to have a strong impact on magnetic order. The biaxial strain (ii) is quite different for the SL on LAO with 1% tensile strain vs 1.7-1.8% for the SLs on STO and PMN-PT. The T_C values of all samples and the shift of T_C under reversible compression are shown in the Fig.7.5(a) left panel. Tensile strain is known to quadratically suppress T_C in cubic-like manganites [36]. The difference of 5 K between the T_C values for LAO and STO substrates, i. e. for a strain difference of $\sim0.7\%$, gives $\Delta T_C/\Delta\varepsilon = 7.1$ K/%. This value is very small if compared to the response to the reversible strain (of 34 K/%, see above), even though the quadratic dependence increases $dT_C/d\varepsilon$ with growing ε. This fact indicates the presence of an additional parameter affecting magnetic order, which is identified as the influence of the interface (iii). The SL on STO seems to have the smoothest interfaces as seen in the reflectivity data, showing, thus, a rather high T_C. Furthermore, the difference in T_C values between STO and PMN-PT samples is large (~10 K) and cannot be explained by 0.1% strain difference, indicating a reduced interface quality (such as roughness) in the SL on PMN-PT.

Similarly, the change of the ordered magnetic moment at low temperatures can only partially be accounted for by the elastic strain: M_S drops from the SL on LAO to the SL on PMN-PT by about a factor of two [Fig.7.5 (a) right panel]. The reversible magnetoelastic response of 8.7% at $T << T_C$ is caused by reversible compression of $\sim0.07\%$ (taking into account the reduction of the reversible strain at low temperature) [35]. This implies $\Delta M/M(0) \sim124\%$ for 1 % of strain if a linear relation $M(\varepsilon)$ would be assumed. Hence, a release of 0.7% of tensile strain can nearly double the ordered magnetic moment. In this way, the reversible strain effect can account for the observed magnetization change in the statically strained SL. However, the difference between the SLs on STO and PMN-PT is again not consistent with a pure strain effect. The smaller M_S of the SL on PMN-PT confirms the presence of an interface effect which is probably related to higher roughness.

Concerning the underlying microscopic mechanisms, tensile strain is known to suppress the ferromagnetic double exchange interaction in $La_{0.7}Ca_{0.3}MnO_3$ [35]. LCMO is orthorhombic in bulk form, but the distortions with respect to a cubic unit cell are rather
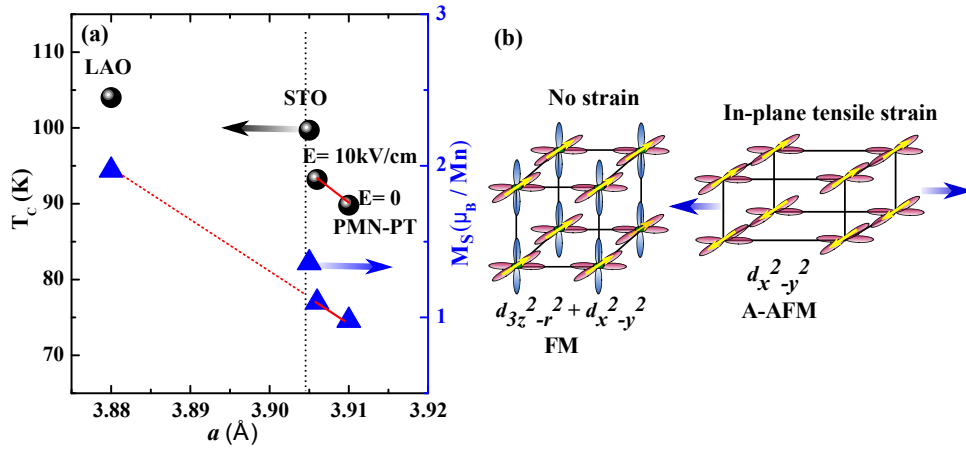
Figure 7.5: (a) T_C vs in-plane lattice parameter (spheres) and M_S vs in-plane lattice parameter (triangles) (The red line indicates the reversible strain effect) (b) Mn spin-orbital structure and strain at the LCMO/STO interfaces. Unstrain DE ferromagnetic structure and A-type AF structure under tensile strain.

small. The atomic structural response to tensile strain, i. e. the strain-dependent rotations and distortions of the MnO_6 octahedra, is not known for this material thus far. The experimentally observed decrease of T_C in thicker epitaxial LCMO films reveals that tensile strain does not bring the lattice structure closer to a cubic symmetry with 180^0 Mn-O-Mn bond angles, which would show the strongest double exchange ferromagnetism. Furthermore, strong tensile strain has been found to lift the orbital degeneracy of the Mn $3d$ e_g electrons, favoring the in-plane $d_{x^2-y^2}$ orbitals in $La_{0.7}Sr_{0.3}MnO_3$ [37, 38, 39]. This orbital occupation leads to an antiferromagnetic A type structure and may be present in the strongly strained LCMO, too [Fig.7.5 (b)]. As a consequence, a competition of ferro- and antiferromagnetic interactions may be induced in the LCMO layers under tensile strain, accounting for the reduced ordered magnetic moment.

Further, the degree of interdiffusion will affect magnetic ordering. Commonly, a suppression of magnetic order with increasing interdiffusion is expected for this type of interface. These issues need investigations of well-characterized interfaces and go beyond the scope of the present work.

Finally, a comment is needed about the possible influence of dislocations which might be present in the SLs on LAO and PMN-PT, because they are not coherently grown on the substrate. Most magnetic oxide films studied under reversible strain on PMN-PT suffered from the same problem, since the lattice parameter of PMN-PT is quite large (4.022 Å) and the films formed dislocations directly at the interface to the PMN-PT [34]. Neither the magnitude of the magnetization nor the T_C of these bulk-like films has been significantly affected by the presence of the dislocations. (This seems to be a difference to ferroelectric oxides where polarization is changed in a significant volume around a dislocation because of its strain field.) If the magnetic order at the lower-dimensional interfaces is similarly robust against the presence of dislocations, remains to be investigated. However, there is no indication for dislocations as a fourth important

parameter governing interface magnetic order.

7.6   Conclusions

The suppressed ferromagnetic order in LCMO (2.6nm)/STO (6.3nm) superlattices has been probed with respect to the influence of elastic biaxial strain. Superlattices in different residual strain states have been obtained on three different monocrystalline oxide substrates. Application of reversible biaxial strain has shown that the ground state ordered magnetic moment can change by about a factor of two upon a biaxial strain change of 1% (in the tensile strain regime near $\varepsilon = 1.7\%$). Although the influence of strain is found to be strong, it cannot account for the reduction of T_C and the ordered magnetic moment in a superlattice on PMN-PT in comparison to the one on $SrTiO_3$, pointing to an enhanced degree of structural defects or interfacial roughness.

Bibliography

[1] R. von Helmolt, J. Wecker, B. Holzapfel, L. Schultz, and K. Samwer, "Giant negative magnetoresistance in perovskitelike $La_{2/3}Ba_{1/3}MnO_x$ ferromagnetic films," Phys. Rev. Lett. **71**, 2331 (1993).

[2] A. J. Millis, "Lattice effects in magnetoresistive manganese perovskites," Nature (London) **392**, 147 (1998).

[3] K. Dörr, "Ferromagnetic manganites: spin-polarized conduction versus competing interactions," J. Phys. D **39**, R125 (2006).

[4] P. Matl, N. P. Ong, Y. F. Yan, Y. Q. Li, D. Studebaker, T. Baum, and G. Doubinina, "Hall effect of the colossal magnetoresistance manganite $La_{1-x}Ca_xMnO_3$," Phys. Rev. B **57**, 10248 (1998).

[5] Y. Ijiri, "Coupling and interface effects in magnetic oxide superlattices," J. Phys.: Condens. Matter **14**, R947 (2002).

[6] J. X. Ma, X. F. Liu, T. Lin, G. Y. Gao, J. P. Zhang, W. B. Wu,X. G. Li, and Jing Shi, "Interface ferromagnetism in (110)-oriented $La_{0.7}Sr_{0.3}MnO_3$/$SrTiO_3$ ultrathin superlattices," Phys.Rev.B **79**, 174424 (2009).

[7] C. Kwon, K.-C. Kim, M. C. Robson, J. Y. Gu, M. Rajeswari, T. Venkatesan, and R. Ramesh, "Desirable magnetotransport properties in doped Mn-oxide-based superlattices," J. Appl. Phys. **81**, 4950 (1997).

[8] H. Y. Hwang, Y. Iwasa, M. Kawasaki, B. Keimer, N. Nagaosa and Y. Tokura, "Emergent phenomena at oxide interfaces," Nature Materials **11**, 103 (2012).

[9] N. M. Nemes, M. J. Calderón, J. I. Beltrán, F. Y. Bruno , J.r G.Barriocanal, Z. Sefrioui, C. León , M.G.Hernández , M. C. Muñoz , L. Brey , and J. Santamaría, "Signatures of a Two-Dimensional Ferromagnetic Electron Gas at the $La_{0.7}Sr_{0.3}MnO_3$/$SrTiO_3$ Interface Arising From Orbital Reconstruction," Adv. Mater. **26**, 7516 (2014).

[10] M. Ziese, I. Vrejoiu, E. Pippel, P. Esquinazi, D. Hesse, C. Etz, J. Henk, A. Ernst, I.V. Maznichenko, W. Hergert, and I. Mertig, "Tailoring Magnetic Interlayer Coupling in $La_{0.7}Sr_{0.3}MnO_3$/$SrRuO_3$ Superlattices," Phys. Rev. Lett. **104**, 167203 (2010).

[11] Marta Gibert, Pavlo Zubko, Raoul Scherwitzl, Jorge Íñiguez & Jean-Marc Triscone, "Exchange bias in $LaNiO_3$–$LaMnO_3$ superlattices," Nature Materials **11**, 195 (2012).

[12] I. Panagiotopoulos, C. Christides, M. Pissas, and D. Niarchos, "Exchange-biasing mechanism in $La_{2/3}Ca_{1/3}MnO_3$/$La_{1/3}Ca_{2/3}MnO_3$ multilayers" Phys. Rev. B **60**, 485 (1999).

[13] M.C. Dekker, A. Herklotz, L. Schultz, M. Reibold, K. Vogel, M.D. Biegalski, H.M. Christen, and K. Dörr, "Magnetoelastic response of $La_{0.7}Sr_{0.3}MnO_3$/$SrTiO_3$ superlattices to reversible strain," Phys. Rev. B **84**, 054463 (2011).

[14] Y. Konishi, Z. Fang, M. Izumi, T. Manako, M. Kasai, H. Kuwahara, M. Kawasaki, K. Terakura, and Y. Tokura, "Orbital-State-Mediated Phase-Control of Manganites," J. Phys. Soc. Jpn. **68**, 3790 (1999).

[15] L. M. Wang, Jing-Kae Lin, and Jong-Pyng Shyu, "Magnetotransport properties of $La_{0.7}Sr_{0.3}MnO_3$/$SrTiO_3$ superlattices," Phys. Rev. B **74**,184412 (2006).

[16] M. Izumi, Y. Ogimoto, Y. Okimoto, T. Manako, P. Ahmet, K. Nakajima, T. Chikyow, M. Kawasaki, and Y. Tokura, "Insulator-metal transition induced by interlayer coupling in $La_{0.6}Sr_{0.4}MnO_3$/$SrTiO_3$ superlattices," Phys. Rev. B **64**, 064429 (2001).

[17] F.Y. Bruno, J. Garcia-Barriocanal, M. Varela, N.M. Nemes, P. Thakur, J. C. Cezar, N.B. Brookes,A. Rivera-Calzada,M. Garcia-Hernandez,C. Leon,S. Okamoto,S. J. Pennycook, and J. Santamaria, "Electronic and Magnetic Reconstructions in $La_{0.7}Sr_{0.3}MnO_3$/$SrTiO_3$ Heterostructures: A Case of Enhanced Interlayer Coupling Controlled by the Interfac," Phys. Rev. Lett. **106**, 147205 (2011).

[18] M. Sahana, T. Walter, K. Dörr, K.-H. Müller, D. Eckert, and K. Brand, "Magnetic properties of heteroepitaxial $La_{0.7}Sr_{0.3}MnO_3$/$SrTiO_3$ superlattices," J. Appl. Phys. **89**, 6834 (1998).

[19] L. F. Kourkoutis, J. H. Song, H. Y. Hwang, and D. A. Muller, "Microscopic origins for stabilizing room-temperature ferromagnetism in ultrathin manganite layers," PNAS **107**, 11682 (2010).

[20] A. J. Millis, T. Darling, and A. Migliori, "Quantifying strain dependence in "colossal" magnetoresistance manganites," J. Appl. Phys. **83**, 1588 (1998).

[21] A. J. Millis, P. B. Littlewood, and B. I. Shraima, "Double Exchange Alone Does Not Explain the Resistivity of $La_{1-x}Sr_xMnO_3$," Phys. Rev. Lett. **74**, 5144 (1995).

[22] M.-H. Jo, N. D. Mathur, J. E. Evetts, M. G. Blamire, M. Bibes, and J. Fontcuberta, "Inhomogeneous transport in heteroepitaxial $La_{0.7}Ca_{0.3}MnO_3$/$SrTiO_3$ multilayers," Appl. Phys. Lett. **75**, 3689 (1999).

[23] J. H. Song, T. Susaki, and H. Y. Hwang, "Enhanced Thermodynamic Stability of Epitaxial Oxide Thin Films," Adv. Mater. **20**, 2528 (2008).

[24] Y. Lu, J. Klein, F. Herbstritt, J. B. Philipp, A. Marx, L. Alff, R. Gross, and H. Zhang, "Structure and transport properties of coherently strained $La_{2/3}$ $Ca_{1/3}$ MnO_3/$SrTiO_3$ superlattices," phys. stat. sol. (b) **242** (8) 1545 (2005).

[25] S. Liang, J. R. Sun, J. Wang, and B. G. Shen, "Magnetic and conductive dead layer at the $La_{0.67}Ca_{0.33}MnO_3SrTiO_3$:Nb interface," Appl. Phys. Lett. **95**, 182509 (2009).

[26] S. A. Fedoseev, A. V. Pan, S. Rubanov, I. A. Golovchanskiy, and Olga V. Shcherbakova, "Large, Controllable Spikes of Magnetoresistance in $La_{2/3}$ $Ca_{1/3}$ MnO_3/$SrTiO_3$ Superlattices," ACS NANO **7**(1), 286 (2013).

[27] M. Bibes, Ll. Balcells, S. Valencia, J. Fontcuberta, M. Wojcik, E. Jedryka, and S. Nadolski, "Nanoscale Multiphase Separation at $La_{2/3}$ $Ca_{1/3}$ MnO_3/$SrTiO_3$ Interfaces," Phys. Rev. Lett. **87**, 067210 (2001).

[28] E Beyreuther, A Thiessen, S Grafström, K Dörrand L M Eng, "Large photoconductivity of oxygen-deficient $La_{0.7}$ $Ca_{0.3}$ MnO_3/$SrTiO_3$ heterostructures," J. Phys.: Condens. Matter. **22**, 175506 (2010).

[29] J.W. Seo, W. Prellier, P. Padhan, P. Boullay, J.-Y. Kim, Hangil Lee, C.D. Batista, I. Martin, Elbert E.M. Chia, T. Wu, B.-G. Cho, and C. Panagopoulos, "Tunable Magnetic Interaction at the Atomic Scale in Oxide Heterostructures," Phys. Rev. Lett. **105**,167206 (2010).

[30] M. Izumi, Y. Ogimoto, T. Manako, M. Kawasaki and Y. Tokura, "Interface Effect and Its Doping Dependence in $La_{1-x}Sr_xMnO_3$/$SrTiO_3$ Superlattices," J. Phys. Soc. Jap. **71**, 2621 (2002).

[31] M. Ziese, H. C. Semmelhack, K. H. Han, S. P. Sena, and H. J. Blythe, "Thickness dependent magnetic and magnetotransport properties of strain- relaxed $La_{0.7}Ca_{0.3}MnO_3$ films," J. Appl. Phys. **99**, 9930 (2002).

[32] D. Fuchs, T. Schwarz, O. Morán, P. Schweiss, and R.Schneider, "Finite-size shift of the Curie temperature of ferromagnetic lanthanum cobaltite thin films," Phys. Rev. B **71**, 092406 (2005).

[33] M.D. Biegalski, D.H. Kim, K.Dörr, H.M.Christen, "Applying uniform reversible strain to epitaxial oxide films," Appl. Phys. Lett. **96**,151905 (2010).

[34] K. Dörr , O. Bilani-Zeneli, A. Herklotz, A. D. Rata, K. Boldyreva, J.-W. Kim, M. C. Dekker, K. Nenkov, L. Schultz, M. Reibold, "A model system for strain effects: epitaxial magnetic films on a piezoelectric substrate," Eur.Phys.J.B **71**, 361 (2009).

[35] C. Thiele, K. Dörr, O.Bilani, J.Rödel, and L. Schultz, "Influence of strain on the magnetization and magnetoelectric effect in $La_{0.7}A_{0.3}MnO_3$ /PMN-PT (001) (A=Sr,Ca)," Phys. Rev. B **75**, 054408 (2007).

[36] P. Dey, T. K. Nath and A. Taraphder, "Effect of substrate-induced strain on transport and magnetic properties of epitaxial $La_{0.66}Sr_{0.33}MnO_3$ thin films,". Appl. Phys. Lett. **91**,012511(2007).

[37] Y. Tokura and N. Nagaosa, "Orbital Physics in Transition-Metal Oxides," Science **288**, 462 (2000).

[38] A. Tebano, C. Aruta, S. Sanna, P.G. Medaglia, and G. Balestrino, A.A. Sidorenko and R. De Renzi, G. Ghiringhelli and L. Braicovich, "Evidence of Orbital Reconstruction at Interfaces in Ultrathin $La_{0.67}Sr_{0.33}MnO_3$ Films" Phys. Rev. Lett. **100**, 137401 (2008).

[39] D. Pesquera, G. Herranz, A. Barla, E. Pellegrin, F. Bondino, E. Magnano, F.Sánchez and J. Fontcuberta, "Surface symmetry-breaking and strain effects on orbital occupancy in transition metal perovskite epitaxial films," Nat. Comm. **3**,1189 (2012).

Chapter 8

Summary and outlook

This thesis presents a study of novel structural and magnetic order at coherent oxide interfaces, particularly in $La_{0.7}A_{0.3}MnO_3/SrRuO_3$ (A = Sr or Ca) and $La_{0.7}Ca_{0.3}MnO_3/SrTiO_3$ heterostructures. $La_{0.7}A_{0.3}MnO_3/SrRuO_3$ has been of particular interest because of the unusually strong antiferromagnetic coupling at the interfaces between ferromagnetic manganite and ruthenate layers. The structural aspects include elastic strain and, for the $La_{0.7}Sr_{0.3}MnO_3/SrRuO_3$ interface, the atomic termination plane of the perovskite-type layers at the interface. Elastic strain has been controlled statically through growing the films on different substrates or dynamically by using a piezoelectric substrate.

Epitaxial superlattice films of $La_{0.7}A_{0.3}MnO_3/SrRuO_3$ (A = Sr or Ca) and $La_{0.7}Ca_{0.3}MnO_3/SrTiO_3$ have been deposited on (001)-oriented several different single-crystalline oxide substrates [$LaAlO_3$ (LAO), $SrTiO_3$ (STO), piezoelectric $0.72PbMg_{1/3}Nb_{2/3}O_3$-$0.28PbTiO_3$ (PMN-PT)] by a multi-target pulsed laser deposition technique. X-ray diffraction (XRD) and Scanning Transmission Electron Microscopy (STEM) have been used to investigate the lattice structure of the grown films. (STEM has been performed by Dr. E. Pippel at the Max-Planck-Institute of Microstructure Physics Halle.) Magnetization has been measured in a SQUID magnetometer at temperatures of 10-360 K and in magnetic fields of 0-4.5 T. On STO (001) substrates, all superlattice samples grew coherently, in agreement with expectations based on the moderate lattice mismatch (< 1 %) of the film components and the substrate. On LAO (001) substrates, all film components have larger lattice parameters than the substrate by more than 1 %, leading to strain relaxation by the formation of dislocations at the substrate surface. Nevertheless, a moderate residual compressive strain has been obtained in superlattice films of about 100 nm thickness using LAO(001) substrates. On PMN-PT (001) substrates with pseudocubic in-plane lattice parameter of 4.02 Å, all film components have smaller lattice parameters than the substrate by more than 2 %, leading again to relaxation of strain by dislocations, but a residual tensile strain of superlattice samples has been obtained. Superlattices are comprised of alternating layers (ABAB...)$_{15}$ forming a coherent perovskite-type crystallographic lattice with one homogeneous in-plane lattice parameter and, thus, well-defined elastic strain. Magnetization measurements of the superlattice samples showed a reduction of the fer-

romagnetic ordering temperature (T_C) of the manganite layers in all superlattices with respect to the bulk value. Besides the influence of finite layer thickness, elastic strain and interface properties (interdiffusion, interface termination and others) affect the magnetic ordering. In the first part of this thesis, an attempt has been made to identify the effects of elastic strain. Tensile strain has been found to strongly suppress T_C of La$_{0.7}$$A$$_{0.3}MnO_3$($A$ = Sr or Ca)) layers in superlattices with both, SrTiO$_3$ or SrRuO$_3$ interlayers. However, it is difficult to clarify the additional impact of the interface structure which changes in the superlattices grown on different substrates. Application of reversible elastic strain in superlattices in piezoelectric PMN-PT substrates provided insights into the direct effect of a moderate biaxial strain of the order of $\sim$0.1 %. Comparing magnetization and Curie temperatures for statically and dynamically strained samples helped to identify real strain effects and revealed the crucially important role of interface properties.

The antiferromagnetic coupling strength in La$_{0.7}$$A$$_{0.3}MnO_3$/SrRuO$_3$ has also been found to depend on biaxial in-plane strain using both, the static and the dynamic strain application (for A = Sr). Superlattice samples on substrates different from TiO$_2$-terminated STO(001), however, had an inferior interface structure with roughness of 1-4 unit cells. In order to investigate a well-defined La$_{0.7}$Sr$_{0.3}$MnO$_3$/SrRuO$_3$ interface, subsequent work has been focused on bilayer films containing one atomically flat interface. It has been observed by STEM that reversing the growth sequence of the two component layers (LSMO, SRO) on TiO$_2$-terminated STO(001) substrates leads to two different atomic interface structures: a MnO$_2$-SrO interface in SRO/LSMO/STO(001) and a RuO$_2$-La$_{0.7}$Sr$_{0.3}$O interface in LSMO/SRO/STO(001). The STEM Z contrast images reveal very low interdiffusion and allow one to conclude on the elemental distributions of Mn, Sr, Ru, and La at the respective type of interface. This is possible because interdiffusion is restricted to Mn/Ru on the B sites of the perovskite lattice and to La/Sr on the A sites, respectively, and the two metal ions have rather different mass / atomic number Z. Magnetization and X-ray magnetic circular dichroism (XMCD) measurements show that magnetic order and coupling for the bilayers with different interface termination is fundamentally different. In case of the MnO$_2$-SrO termination (called termination A), antiferromagnetic coupling of LSMO and SRO is very strong, leading to an unusual, rigidly coupled switching of an interface-near SRO layer together with the LSMO layer. The other interface termination shows exchange-bias-type behavior. Magnetic switching of Mn and Ru has been derived from XMCD spectra recorded at the Ru and Mn L-edges (at the ALBA Synchrotron Light Source in Barcelona). These observations indicate efficient control of magnetic order and coupling at a coherent oxide interface through engineering the interface termination.

Density functional theory (DFT) calculations of a collaborating group (I. Maznichenko, I. Mertig) have confirmed the strong difference of the antiferromagnetic coupling strength between the two interface terminations. At present, the details of atomic and electronic reconstructions of the two interface types are not yet fully understood. Magnetic anisotropy of termination A bilayers indicates a different lattice symmetry of the interface-near SRO

layer (tetragonal, instead of bulk-like orthorhombic) which is likely to be associated with the rotational pattern of the oxygen octahedra across the interface. Further, both interface terminations show a nominal charge and require charge transfer to the interface, since the lattice planes are not electrically neutral. However, both LSMO and SRO are metals, making an electronic charge redistribution easy (which is inherently included in the DFT results) and, thus, any ionic reconstruction or interdiffusion might be avoided.

Termination control of oxide interfaces is yet rarely successful. The proposed strategy of thin film growth and STEM characterization may help to explore coherent interfaces of other oxides and reveal the inherent electronic and magnetic properties of atomically well-defined interfaces. Very recently, some STEM facilities achieved atomic resolution for Electron Energy Loss Spectroscopy (EELS) where tracing of individual chemical elements across the interface is possible. In this way, the problem of identifying similar mass metal ions (such as Mn and Ti) could be overcome. Also a detailed understanding of the physics on the orbital occupation of these elements (Mn and Ru) in different interfaces would potentially open up new avenues of researches in the field of oxide interfaces. Probing the underlying mechanism of such a novel phenomenon would involve detailed analysis of resonant X-ray reflectivity measurements, which can provide insights on the valence state and orbital occupation of Mn and Ru at the interface. Eventually, novel electronic states at termination controlled oxide interfaces might be discovered and utilized in emerging device concepts of oxide electronics.

Curriculum vitae

Sujit Das

Personal information

Date of birth	9th January 1988
Place of birth	Gangarampur, West Bengal, India
Nationality	Indian
Civil status	Single

Education

Period	University/Institution
04/2012-present	PhD student at Martin-Luther-Universität Halle-Wittenberg, Halle, Germany Guest scientist at IFW Dresden, Germany
05/2009-06/2011	M.Sc (Master of Science) in Physics, Indian Institute of Technology, Kanpur, India
03/2006-04/2009	B.Sc (Bachelor of Science) in Physics, Calcutta University, Kolkata, India

Publications

1. Termination control of magnetic coupling at a complex oxide interface, **S. Das**, A. D. Rata, I. V. Maznichenko, S. Agrestini, E. Pippel, K. Chen, S. M. Valvidares, H. Babu Vasili, J. Herrero-Martin, E. Pellegrin, K. Nenkov, A. Herklotz, A. Ernst, I. Mertig, Z. Hu, and K. Dörr (Submitted) (Arxiv 1606.08687).

2. Strain dependence of the antiferromagnetic interface coupling in $La_{0.7}Sr_{0.3}MnO_3/SrRuO_3$ superlattice, **Sujit Das**, Andreas Herklotz, Eckhard Pippel, Er-Jia Guo, Diana Rata, and Kathrin Dörr, Phys. Rev. B **91**, 134405 (2015).

3. Strain-induced improvement of retention loss in $PbZr_{0.2}Ti_{0.8}O_3$ films, E. J. Guo, R. Roth, **S. Das**, A. Herklotz, and K. Dörr, Appl. Phys. Lett. **106**, 072904 (2015).

4. Static and reversible elastic strain effects on magnetic order of $La_{0.7}Ca_{0.3}MnO_3/SrTiO_3$ superlattices, **Sujit Das**, Andreas Herklotz, Er Jia Guo, and Kathrin Dörr, Journal of Applied Physics **115**, 143902 (2014).

5. Strain induced low mechanical switching force in ultrathin $PbZr_{0.2}Ti_{0.8}O_3$ films, E. J. Guo, R. Roth, **S. Das**, and K. Dörr Appl. Phys. Lett. **105**, 012903 (2014).

6. Enhancement of switching speed of $BiFeO_3$ capacitors by magnetic fields, E. J. Guo, **S. Das**, and A. Herklotz, APL Materials **2**, 096107 (2014).

7. Tuning the switching time of $BiFeO_3$ capacitors by electrodes conductivity, E. J. Guo, A. Herklotz, R. Roth, M. Christl, **S. Das**, W. Widdra and K. Dörr, Appl. Phys. Lett. **103**, 022905 (2013).

8. Preparation and Magnetic Studies on 10% Co- doped $BiFeO_3$ Multiferroic Nanoparticles, Samar Layek, **Sujit Das** and H. C. Verma, AIP Conf. Proc. **1349**, 351 (2011).

Acknowledgements

The thesis has become a reality due to kind support and assistance from many individuals who always extended helping hand till the work was finished. It is always pleasurable to express my hearted gratitude to all of them.

First of all I am deeply grateful to Prof. Dr. Kathrin Dörr for her guidance and constant encouragement throughout supervision of the work for the entire period of my Ph.D. work. I enjoyed every bit of discussion with her which helped me a lot to gain the insight into the subject. I also owe gratitude to the referees for their kind agreement to be referee of this thesis and offering invaluable suggestions to improve the work.

I would like to express my thanks to all my collaborators, without whom the project would not have reached to this dimension. Their input and useful discussions have increased a lot of my understanding and knowledge on this project. I would like to extend my sincere thanks to Dr. Andreas Herklotz for all his guidance to learn about the instruments. I am thankful to Dr. K. Nenkov for assistance with the SQUID measurements. During the work, I have greatly benefitted from the discussions and insight- ful comments from Dr. Diana Rata, Dr. Er Jia Guo, Dr. Andreas Herklotz. Special thanks are due to all my friends in and outside my institute whose help was imperative and the company has always been a blessing to me.

Lastly, but certainly not the least, I would like to express my love and regards to my family members for their enormous support and encouragement which inspired me in every aspect of my research not only during the time I worked on the thesis but all along the journey.

Eidesstattliche Erklärung

Hiermit erkläre ich eidesstattlich, dass ich meine Dissertation selbständig und ohne fremde Hilfe verfasst und keine anderen als die von mir angegebenen Quellen und Hilfsmittel zur Erstellung meiner Dissertation verwendet habe. Die wörtlich und inhaltlich entnommenen Stellen habe ich als solche gekennzeichnet und den entnommen Werken zugeordnet. Die Arbeit ist in vorliegender oder ähnlicher Form bei keiner anderen Prüfungsbehörde zur Erlangung eines Doktorgrades eingereicht worden.

Sujit Das

Halle (Saale), July 2016